Fine-Grained Sediment Dynamics and Morphodynamics in Tide-Dominated Channels

Robin McLachlan

A dissertation

submitted in partial fulfillment of the

requirements for the degree of

Doctor of Philosophy

University of Washington

2020

Reading Committee:

Andrea Ogston, Chair

Charles Nittrouer

John Wesley Lauer

Program Authorized to Offer Degree:

Oceanography

University of Washington

Abstract

Fine-Grained Sediment Dynamics and Morphodynamics in Tide-Dominated Channels

Robin McLachlan

Chair of the Supervisory Committee:
Professor Andrea Ogston
Oceanography

Rivers supply the bulk of sediment to the world ocean and are, therefore, crucial in building the foundation of coastal ecosystems and communities. As rivers approach the ocean, sediment dispersal can become dominated by tidal processes, and much sediment is trapped within delta distributary channels. Sediment that is discharged from a river mouth is not necessarily lost to the ocean. Instead, much of this sediment migrates along the coast before depositing back onshore. While coastal environments have been intensely studied, much remains to be learned about fine-grained sediment dispersal, specifically the impact of channel-network morphology on flux pathways and morphologic development in tidal environments, which is the focus of this work.

Within tide-influenced deltas, the partitioning of water and sediment flux between distributaries is often disproportionate to channel size, which influences the morphologic development of river deltas. While along-channel controls of sediment flux have been well studied in single-channel rivers and estuaries, the partitioning of flux remains incompletely understood in deltas with multiple distributaries subjected to bidirectional tidal flow. Research presented here shows that channel depth impacts the vertical distribution of sediment, and, as a result, complex bathymetry drives sediment-flux partitioning at a channel bifurcation.

Water velocity and suspended-sediment properties were measured at a transect upstream of a bifurcation in the Mekong River Delta over two semidiurnal tidal cycles while the region was a seasonal tidal river. Suspended particles were predominately microflocs, and the smallest particles (<40 μm) dominated the mass settling flux, rather than the less frequent large microflocs and macroflocs. Additionally, strain rates and sediment fluxes were tidally symmetric within the deep subchannel of the

bifurcating distributary but ebb dominant within the shallow subchannel. Ebb dominance promoted sediment-induced stratification, and thus sediment import upstream from the shallow distributary. Sediment-induced stratification occurred at concentrations >400 mg L^{-1}.

Comparing these results to those from previous studies at this site indicate that sediment-flux partitioning is reversed when estuarine conditions persist at the bifurcation, and that sediment delivery to downstream distributaries is reliant on both channel depth and estuarine-intrusion length. These conclusions are applicable to other tidally influenced deltas that have large supplies of fine-grained sediment, low channel sinuosity, and distributaries of similar lengths. In these deltas, the predicted global increase in sediment trapping may be disproportionately large in relatively shallow channels.

Sediment that discharges from the largest tropical rivers, like the Mekong and Amazon, is commonly transported through and deposited in mangrove forests. Sedimentary research has traditionally focused on characterizing flux patterns within mangrove forests that are associated with single rivers, nearshore environments, or terminating tidal channels. However, flows within the most extensive mangrove forests tend to be driven through channels that connect to multiple estuaries or other channels, and consequently experience tides with different temporal lags.

To characterize how connectivity impacts sediment transport in the world's largest continuous mangrove stand, *in-situ* observations of water and sediment flux were obtained in two tidal channels near the Amazon River. The low-connectivity channel connects to one estuary whereas the high-connectivity channel connects two estuaries. Results indicate that channel connectivity controls the amount of sediment stored in channels that is available to supply mangrove forests. Although tidal phase-duration asymmetry is flood dominant in both channels, velocity asymmetry becomes ebb dominant during tidal cycles when the mangrove flats are inundated. Additionally, tidal elevation and water velocity are not in quadrature for the high-connectivity channel, as they are for the low-connectivity channel. As a result, the high-connectivity channel acts as a conduit for sediment from one estuary to another rather than simply importing and retaining sediment like the low-connectivity channel. Therefore, high-connectivity channels are expected to distribute point-source sediment along coastlines and provide sediment to estuaries and channels that may not have their own direct source.

The coastline southeast of the Amazon River mouth is composed of a series of estuaries and mangrove-vegetated peninsulas, each thought to have formed by repeated sand-bar emergence and subsequent back-barrier infilling. The high-connectivity channel initially formed *ca* 2 ka as an open lagoon behind a sandy barrier island. Understanding how back-barrier environments infill and evolve is necessary to predict how they will respond to future changes in sea level and sediment supply. With this motivation, *in-situ* observations of sediment flux and sedimentary signatures from this Amazonian tidal-channel system are interpreted to create a conceptual model of morphologic evolution in a macrotidal back-barrier

environment. This model applies to other environments that are similarly rich in fine-grained sediment, vegetated by mangroves, and incised by tidal channels with multiple outlets.

Results indicate that within a high-connectivity back-barrier tidal channel, tidal processes dominate sedimentation and morphological development. Shallow cores (<60 cm) exhibited millimeter-scale tidalites composed of sand and mud. High-connectivity channels allow tidal propagation from multiple inlets, and in this case, the converging flood waves promote delivery of sediment fluxing through the system to the mangrove flats in the convergence zone. Sediment preferentially deposits in regions with adequate accommodation space and dense vegetation, and in these zones, bed sediment grain size is slightly finer than that transiting through the system. The greatest sediment-accumulation rates (3 to 4 cm yr^{-1}), calculated from steady-state ^{210}Pb profiles, were found in the convergence zone near the mangrove-channel edge.

As tidal flats aggrade vertically and prograde into the channels, accommodation space diminishes. In effect, the channel's narrowest stretch is expected to migrate along the path of net-sediment flux toward regions with more accommodation space until it reaches the tidal-convergence zone. The location of recent preferential infilling is evidenced by relatively rapid sediment-accumulation rates, finer sediment, and significant clustering of small secondary tidal channels. These findings shed light on how sediment transported through vegetated back-barrier environments is ultimately preserved and how evidence preserved in surface morphology and the geological record can be interpreted.

TABLE OF CONTENTS

LIST OF FIGURES

ACKNOWLEDGEMENTS

The completion and quality of this work was only possible with the support offered by many people. First, I thank my adviser, Andrea Ogston, who dedicated countless hours of intellectual and emotional effort to my development over the past six years. She is not only a dedicated scientist, educator, and collaborator, she is a friend. I cannot express in words how much I admire her and thank her for her support in all of my academic and scientific achievements.

I also owe a tremendous thanks to countless present and former students. I thank the members of the UW Sediment Dynamics Lab for their friendship and support: Hannah Glover, Aaron Fricke, Emily Eidam, Evan Lahr, Daniel Culling, Rip Hale, and Dan Nowacki. I give a special thanks to Aaron for his tremendous effort in the field, Emily for her never-ending mentorship in the lab, and Hannah for her encouragement both in the lab and on the trail. I am very grateful to the undergraduate students who helped with this research, particularly Julia Wallace and Jenny Renee. To my fantastic cohort, thank you for warming my heart and stoking my passion over the past six years.

I am fortunate to have been a part of several collaborative studies and count myself as lucky to have met so many fantastic scientists around the world. In Vietnam, I appreciate Rich Nguyen for his tireless work and guidance. I also thank all of the students, faculty, and staff of Vietnam National University. In Brazil, I am tremendously grateful to Nils Asp, his lovely family, and his dedicated students.

I am deeply grateful to my scientific mentors at the University of Washington. I thank all of my committee members for their time, dedication, and fresh ideas. I also thank Miles Logsdon for his wit, enthusiasm, and unwavering confidence in my educational pursuits.

Finally, and most importantly, I thank my family. To my parents, thank you for raising me to be strong willed and adventurous. To my wonderful husband, Will, thank you for joining me on this journey and for your unwavering support and constant encouragement.

This work was supported by the U.S. Office of Naval Research and the National Science Foundation. This material is based upon work supported by the National Science Foundation Graduate Research Fellowship under Grant No. DGE1256082. Any opinion, findings, and conclusions or recommendations expressed in this material are those of the authors and do not necessarily reflect the views of the National Science Foundation.

Chapter 1.
INTRODUCTION

Rivers are the primary connection between land and sea, as they supply the bulk of sediment to the world ocean (Milliman & Meade, 1983). Upon nearing and reaching the marine realm (Figure 1.1), much of this terrigenous sediment is captured by hydrodynamic processes unique to coastal zones, such as tidal-velocity modulation and estuarine circulation, and then deposited, essentially building the foundation of coastal ecosystems and communities. With ~40% of the world's population living within 100 km of a coastline (Kummu, 2016) and deltaic lowlands supporting >60% of people living in coastal communities (Tamura et al., 2012), there is a clear and urgent need to study modern sediment dynamics and historic sedimentary deposits to gain a more comprehensive understanding of how coastal morphology develops with time.

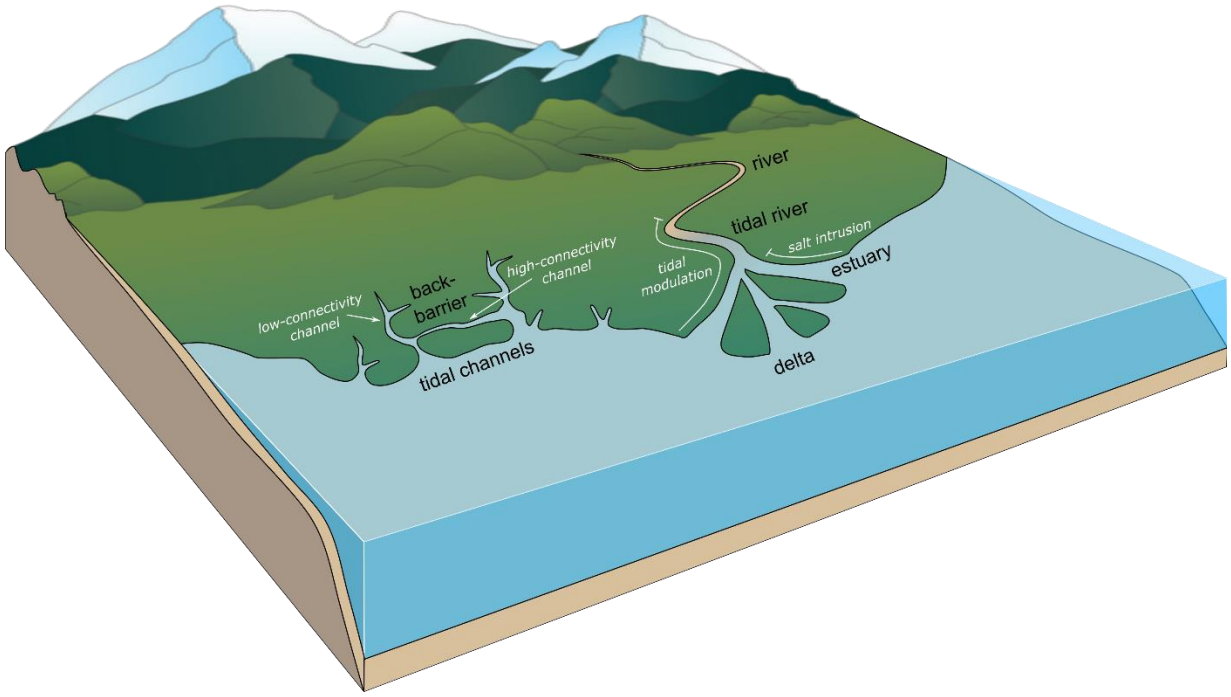

Figure 1.1. Conceptual coastline illustrating the possible environments that suspended sediment may traverse upon nearing and reaching the marine realm. This dissertation focuses on sediment transport within tidal rivers, at delta bifurcations, and through tidal channels.

While coastal environments have been the focus of intensive observational and numerical-modeling studies over the past several decades, much still remains unknown about fine-grained sediment dispersal,

including the impact of complex channel morphology on flux pathways and how modern observations of these pathways can inform our understanding of century- to decadal-scale morphologic development. This dissertation describes observational research in the Mekong tidal river and Amazonian tidal channels that interprets feedbacks between the dispersal of fine-grained sediment and channel morphology, specifically distributary depth and tidal-channel connectivity.

1.1 SEDIMENT FLUX IN TIDAL RIVERS

Exploration of sediment pathways has been traditionally split into distinct dynamical zones (i.e., fluvial, littoral, shelf), but freshwater rivers seamlessly transition into intertidal and brackish areas. Our knowledge of fluvial sediment dispersal is informed by substantial bodies of research in rivers and estuaries, though much less in known about sediment dynamics within the transition between these two environments, tidal rivers, which are modulated by tides but have no salinity. Because the tidal river lies outside traditional limits of river and estuarine research, research in this complex region is relatively lacking (Barendregt & Swarth, 2013), and the scarcity of relevant data limit our ability to accurately model the flux of water and sediment and to predict changes in geomorphology (Ensign et al., 2012, 2013; Hoitink & Jay, 2016). Therefore, fluvial and marine sedimentologists are increasingly embracing the source-to sink framework (e.g., Driscoll & Nittrouer, 2000; Warrick et al., 2015; Liu et al., 2016) to explore mechanisms that control sedimentation and morphology within terrestrial-marine interface zones.

In a recent effort to better understand tidal-river dynamics, several studies have addressed water flux, focusing on tidal-wave propagation (e.g., Bonneton et al., 2012; Eslami et al., 2019), river-velocity modulation (e.g., Jay & Flinchem, 1997), tidal impacts on hydraulic geometry (e.g., Ensign et al., 2013), and nonlinear interactions among tidal constituents (e.g., Gallo & Vinzon, 2005). As this field of research has advanced, more effort is now being devoted to studying sediment flux though tidal rivers (e.g., Sassi et al., 2013; Nowacki et al., 2015; Pritchard & Green, 2017), including many site-specific numerical models (e.g., Ralston & Geyer, 2017; Xing et al., 2017). This effort is challenging because sediment is negatively buoyant and does not passively follow water flux. Furthermore, suspended-sediment size and settling rate are altered by a host of interacting fluvial and marine processes, including tidally varying shear stress, mixing, and salinity (McLachlan et al., 2017).

In Chapter 2, an observational study in the Mekong tidal river explores the impact of distributary depth on vertical mixing, suspended-sediment aggregation and distribution, and sediment-flux partitioning at a channel bifurcation. The Mekong River was chosen for this study because it is a world leader in both water and sediment discharge (Ta et al., 2002; Milliman & Farnsworth, 2011), and concurrent studies examined the interconnecting sediment-transport pathways between the tidal river, coastal mangrove

fringe, and shallow shelf clinoform (e.g., Eidam et al., 2017; Fricke et al., 2017b; McLachlan et al., 2017). The delta is also home to >20 million people and helps support Vietnam through agriculture, aquaculture, and industry (Tamura et al., 2012). Thus, flux partitioning, and its role in the morphologic development of this highly anthropogenically modified delta, has major environmental and economic consequences for Vietnam.

1.2 SEDIMENT FLUX IN MANGROVE-VEGETATED TIDAL CHANNELS

After passing through the tidal river and estuary, much sediment travelling along its source-to-sink pathway deposits in the nearshore, building and sustaining complex coastal ecosystems. For example, sediment discharged from the world's largest tropical rivers, including the Mekong and Amazon (Milliman & Farnsworth, 2011), commonly nourishes mangrove forests. Mangrove forests are globally vital ecosystems that serve as important marine nurseries (e.g., Alongi, 2002; Glaser, 2003), significant carbon sinks (e.g., Donato et al., 2011), and buffers to coastal erosion (e.g., Souza-Filho et al., 2006). These forests are estimated to cover >170k km^2 globally (Spalding et al., 1997), but they are disappearing at alarming rates; over one-third of the world's mangrove forests have been lost since the 1950s (Alongi, 2002).

The relatively pristine Amazonian coastline is an ideal site to study natural mechanisms that act to build and sustain the foundation of mangrove forests because the Amazon River and smaller local rivers are largely unaltered by dams, levees, and dredging, and the forests themselves are left predominantly untouched by humans. An impressive body of research has explored sediment dynamics and dispersal within the Amazon river (e.g., Richey et al., 1986; Dunne et al., 1998), tidal river (e.g., Nowacki et al., 2015; Fricke et al., 2017a, 2019), near-mouth continental shelf (e.g., Gibbs, 1976; Kuehl et al., 1986; Nittrouer & DeMaster, 1996), and littoral zone northwest of the river mouth (e.g., Allison et al., 1995b, 2000). Far less is known of sediment dispersal along the southeastern coast, despite the region hosting the world's largest continuous mangrove stand, spanning almost 8,000 km^2 (Filho et al., 2004).

The coastline southeast of the Amazon River mouth is composed of a series of complex estuary and tidal-channel networks, but the dynamics controlling sediment exchange between the sandy inner shelf, estuarine basins, and muddy mangrove flats are not yet well understood. In Chapter 3, research is described that examines along-coast sediment dispersal via tidal channels, focusing on two tidal channels that bisect the Ajuruteua Peninsula ~200 km southeast of the Amazon River mouth. This research provides foundational concepts to the field of mangrove sediment dynamics by characterizing how hydrodynamics and morphology, mainly channel connectivity, interact to control sediment dispersal along coastlines and accumulation within mangrove forests.

1.3 LINKING MODERN FLUX WITH MORPHOLOGIC EVOLUTION

While studies of *in-situ* dynamics can shed light on how coastal regions are developing today, exploration must reach deeper into sedimentary deposits to understand how these environments have developed through time. Interpretations at both modern and geologic (order 10^3 years) timescales are aided by combining the two: *in-situ* observations of processes acting on sediment in transit and information preserved in the sedimentary substrate on how that sediment is ultimately preserved. However, few studies have explored sediment accumulation and depositional processes within mangrove forests over a broad range of timescales (Woodroffe et al., 2016).

In Chapter 4, conclusions from Chapter 3 are considered in conjunction with research that examines sediment-accumulation rates, shallow stratigraphy, and secondary-channel network geometry across the Ajuruteua Peninsula. Much is known of the coastline's large-scale geologic development for the past several thousand years. Stratigraphic interpretation along the peninsula suggests that the coastal plain is a large back-barrier system and that coastal evolution over the past 5 kyr has been modulated by small-scale subsidence events associated with three phases of barrier island development (Souza-Filho et al., 2006). As the rate of sea-level rise decreased in the last 2 kyr, the peninsula underwent the most significant progradation phase and mudflat progradation restricted estuarine flow into the back-barrier channels (Souza-Filho et al., 2006). In Chapter 4, a conceptual model of back-barrier infilling is presented that links modern observations of sediment flux and channel morphology with millennia-scale evolution of the back-barrier environment, again focusing on the role of tidal-channel connectivity in sediment dispersal.

Chapter 2.
Sediment-Flux Partitioning and Sediment-Induced Stratification at a Tidal River Bifurcation [1]

2.1 INTRODUCTION

Rivers not only deliver water, sediment, and nutrients that build and maintain fertile deltaic environments, which are home to over half a billion people worldwide (Ericson et al., 2006), they also counter the landward intrusion of saline water and estuarine processes. Upstream of the estuary, the section of river that is void of salinity but experiences the backwater effect, meaning that velocity is modulated by ocean tides, is referred to as the tidal river. Because tidal rivers and estuaries host unique hydrodynamics and produce differing sediment-flux pathways, sedimentation at a single location can drastically change if it is crossed by the transient boundary between the two regimes over seasonal, or longer, timescales.

Within tidal rivers, water and sediment fluxes are modulated by tidal processes, often even reversing (Hoitink & Jay, 2016), though residual downstream fluxes are most-commonly observed (e.g., McLachlan et al., 2017; Pritchard and Green, 2017; Ralston and Geyer, 2017). At the interface between tidal rivers and estuaries, much sediment is trapped due to flux convergence and reduced shear stresses associated with the estuarine turbidity maximum (Schubel, 1968; Meade, 1972; McLachlan et al., 2017). Within estuaries, the residual along-channel direction of sediment flux depends on many factors related to turbulent mixing and channel geometry. Relatively strong fluvial velocity promotes stratification and salt-wedge formation (Geyer & MacCready, 2014). In salt-wedge estuaries, which are typical of deep, confined fluvial channels, export of fluvial sediment to the coastal ocean is promoted because stratification hinders particle settling through the pycnocline toward the bed (Nowacki et al., 2015). In contrast, relatively strong tidal velocity promotes vertical mixing (Geyer & MacCready, 2014), and well-mixed estuaries favor retention of fluvial sediment within the channel through tidal pumping (e.g., Lanzoni, 2002; Scully and Friedrichs, 2007).

While along-channel controls of sediment flux have been well studied in single-channel rivers and estuaries, the partitioning of flux remains incompletely understood in deltaic channels with multiple distributaries subjected to bidirectional flow. Flow partitioning between distributaries that is disproportionate to channel size has been observed in numerical model results (Edmonds & Slingerland,

---

[1] This chapter was formatted for journal submission as: McLachlan, R.L., Ogston, A.S., Di Leonardo, D.R., Allison, M.A., and Hilmo, R.S., Sediment-flux partitioning and sediment-induced stratification at a tidal river bifurcation.

2007, 2008; Bolla Pittaluga et al., 2015) and in observational studies of many large deltas, including the Ganges-Brahmaputra (Haque et al., 2015), Mekong (Nguyen et al., 2008), Mississippi (Wright & Coleman, 1974), Fly (Harris et al., 2004), and Yangtze (Zhang et al., 2011). Because distributaries receive unequal proportions of the river discharge, the ratio of fluvial to marine influence also varies between channels, causing different mixing regimes, sediment-flux pathways, and degrees of sediment retention within the channels. Other factors also affect this ratio in asymmetric branching channel networks, including channel bathymetry (Geyer & MacCready, 2014), distributary length (Wagner & Mohrig, 2019), and configuration of the shoreline (Li et al., 2011).

Here, we will explore the impact of channel depth on sediment-flux partitioning at a tide-influenced channel bifurcation. Turbulence production and mixing in channels with no vertical density gradients, such as in tidal rivers, can be characterized by the Reynolds number, which increases with both distributary depth (h) and flow velocity (u). In stratified estuaries, which do have strong vertical density gradients, the effectiveness of tidal mixing is more appropriately quantified with the mixing number (Geyer & MacCready, 2014). Because the mixing number decreases with depth, shallower estuaries tend to be more vertically mixed while deeper estuaries promote stratified salt-wedge formation.

The above terms quantify the degree of vertical mixing of water, though they largely disregard the impact of sediment. Suspended sediment increases fluid density and can create strong vertical density gradients near the bed, i.e., sediment-induced stratification. In highly turbid estuaries and nearshore environments, sediment-induced stratification has been found to reduce the frictional bottom drag (King & Wolanski, 1996), suppress near-bed turbulent fluxes (West & Oduyemi, 1989; Friedrichs et al., 2000), and reduce dissipation of turbulent kinetic energy (Jones & Monismith, 2008). As a result, the maximum strain rate increases and is lifted away from the bed (Adams & Weatherly, 1981), and the carrying capacity of the flow is reduced (Trowbridge & Kineke, 1994) because dense, sediment-laden fluid is more difficult to mix upward into high-velocity portions of the water column.

Additionally, suspended particles are denser than water and do not mix conservatively. Processes that change particle settling rates complicate the effort to describe vertical distribution of sediment. For example, aggregate formation increases the effective size and settling velocity of suspended particles, thus altering particle sedimentation-erosion behavior. Suspended-sediment concentration, shear stress, and the presence of binding factors, such as organic polymers and salt ions, modulate aggregate formation and break up (Burban et al., 1989; Dyer & Manning, 1999; Winterwerp, 2002) and differ between tidal-river and estuarine regimes. Therefore, to properly model sediment-exchange processes at channel bifurcations with bidirectional flow, the impact of channel-network morphology and distributary depth on vertical mixing, sediment-induced stratification, and particle aggregation must first be accurately characterized.

The ability to accurately characterize and predict sediment-flux pathways in river deltas is important because anthropogenic and natural processes are increasingly altering the spatial extent of tidal-river and estuarine processes. Human alteration of drainage basins impacts what material is delivered to rivers, as well as the morphodynamics of the channel and deltaic surfaces downstream. Significant changes to delta morphology have been observed in most of the worlds' largest river deltas due to cumulative impacts of processes such as land-use change (Walling, 2006; Hayashi et al., 2019; Liu et al., 2020), dam installation (Milliman & Farnsworth, 2011; Syvitski & Kettner, 2011), and cyclone activity (Mousavi et al., 2011; Sobel et al., 2016; Walsh et al., 2016). On average worldwide, deltas have temporarily gained land surface area (Nienhuis et al., 2020) while losing elevation (Syvitski et al., 2009), in large part due to decreased river discharge (Milliman & Farnsworth, 2011; Syvitski & Kettner, 2011). Along with these changes, the boundaries between the tidal rivers and estuaries are commonly migrating upstream, altering sediment-flux pathways as they move (Rice et al., 2012; Anh et al., 2018; Akter et al., 2019).

Here, we aim to characterize the impact of distributary depth on flow and sediment-flux partitioning at a channel bifurcation that seasonally shifts between a tidal river and partially mixed estuary. Because distributary morphology governs short-term flow partitioning and transport processes, it also determines morphologic evolution and estuarine biogeomorphology over longer timescales (Schwarz et al., 2017; Nienhuis et al., 2018), timescales that are impacted by large-scale anthropogenic alterations to drainage basins and climate. As such, we use our results to predict how flow partitioning and sedimentation will shift at our study site in the Mekong Delta, as well as in deltas worldwide, due to decreasing fluvial discharge.

2.2 STUDY REGION

The Mekong River (Figure 2.1) flows >4000 km from its source in China's Tibetan Plateau to its delta in Vietnam. The Mekong River is estimated to discharge ~550 km^3 yr^{-1} of water and ~150 Mt yr^{-1} of sediment (Ta et al., 2002; Milliman & Farnsworth, 2011) into the East Sea, also known as the South China Sea. Upon reaching the delta, the river splits into eight distributaries. The largest distributary, named the Sông Hậu, carries ~40% of the total water flow (Nguyen et al., 2008) and remains a single channel until splitting around an island to form two channels: the Định An and the Trần Đề. The Định An, the larger of the two channels, is estimated to carry ~70% of the water discharge from the Sông Hậu (Nguyen et al., 2008).

This study focuses on the region of the Sông Hậu just upstream of its bifurcation, ~40 km from the river-ocean interface. This region is ideal for this research because the two distributaries are approximately equal in length, and the propagating tidal waves reach the bifurcation almost simultaneously from each

distributary channel (Eslami et al., 2019a). Therefore, channel depth, rather than tidally induced lateral circulation, is expected to be a primary control on flow partitioning around the island.

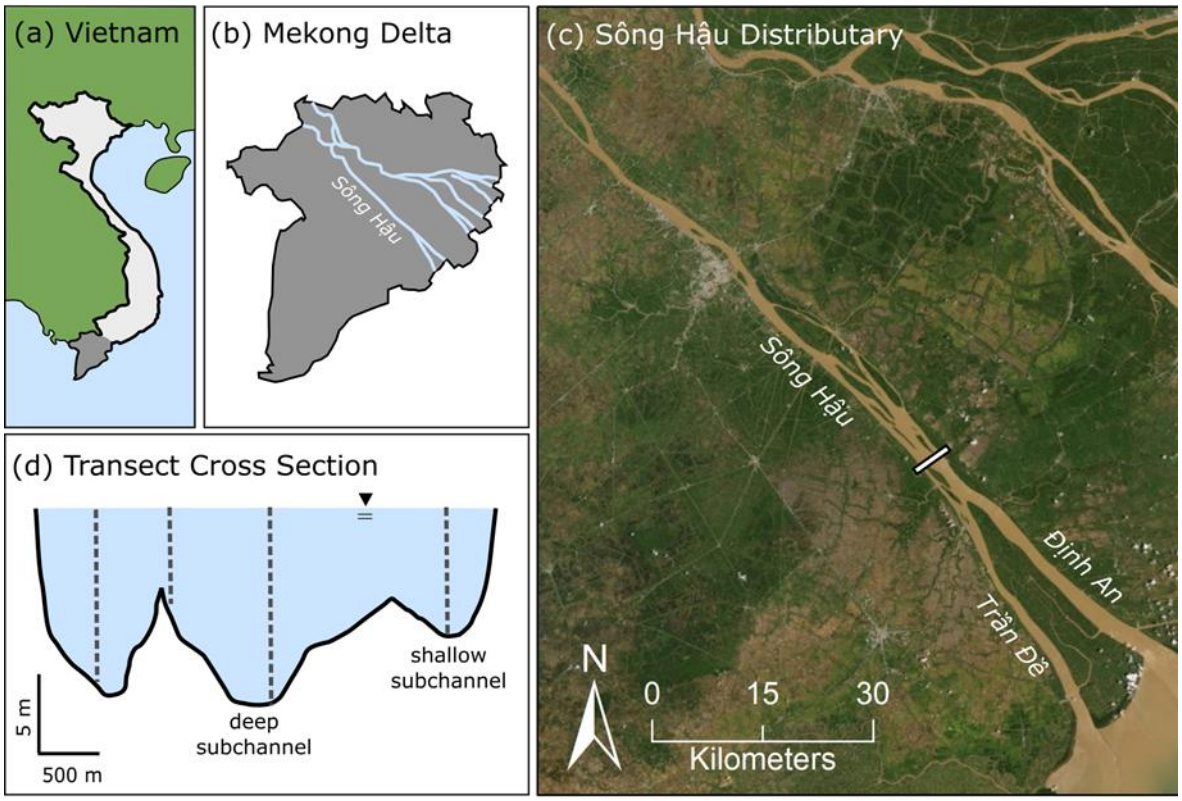

Figure 2.1. Basemaps displaying the geography of (A) Vietnam, (B) the Mekong Delta, (C) the study distributaries and transect location, and (D) cross-sectional bathymetry of the study transect with station locations indicated by dashed lines. The cross section is oriented looking downstream.

The Mekong Delta is presently dominated by mixed, semidiurnal tides. Tidal range at the river mouth is ~3 m, and tidal modulation of river flow extends >200 km upriver (Nowacki et al., 2015; McLachlan et al., 2017). River-discharge magnitude and estuarine regime are seasonally variable. During the wet season (May to October), river discharge reaches its maximum and a stratified salt wedge confined to the distributary depths propagates ~20 km upriver (Nowacki et al., 2015; McLachlan et al., 2017). Ebb tidal currents dominate tidal flows, and sediment export from the Sông Hậu is estimated to range from 1 t s^{-1} (Nowacki et al., 2015) to 1.7 t s^{-1} (McLachlan et al., 2017). Much of this sediment is deposited near the river mouth on the inner continental shelf (Eidam et al., 2017; Liu et al., 2017) and along adjacent coastlines (Fricke et al., 2017b). The river bed at this time is predominately composed of sand and silt, with bedforms consisting of exposed relict mud units and mobile sand dunes ≤2 m in height (Allison et al., 2017).

During the dry season (November to March), river discharge diminishes, the river's lower ~40 km becomes a partially mixed estuary (Nowacki et al., 2015; McLachlan et al., 2017), and flood tidal currents

become dominant (Nowacki et al., 2015). Some sediment that was deposited offshore during the previous wet season is imported into the two Sông Hậu distributaries at ~0.3 t s^{-1} (Nowacki et al., 2015; McLachlan et al., 2017), creating a mantle of soft mud ~0.25 m thick on top of the previously exposed bedforms (Allison et al., 2017).

Aggregation of suspended sediment plays an important role in sediment deposition on the channel bed (Gratiot et al., 2017; McLachlan et al., 2017). Though sand-sized particles are commonly observed in suspension during the dry season, most suspended particles with diameters >10 μm are aggregates (Gratiot et al., 2017) so the flux of discrete sand grains is near zero (Stephens et al., 2017). Fine-grained particles aggregate in the Mekong's fresh tidal river before reaching the saline estuary (McLachlan et al., 2017), an observation not uncommon in rivers with large concentrations of organic material (Zimmermann-Timm, 2002). These particles further aggregate upon reaching brackish water and are estimated to have average effective densities (ρ_e) of ~0.15 g cm^{-3} and settling velocities often >0.5 mm s^{-1} (McLachlan et al., 2017). Most aggregates observed are microflocs (<150 μm), though macroflocs (>150 μm) are also present. This aggregation due to both biologic and physio-chemical processes promotes faster settling of fine-grained particles, and aids in sediment trapping within the Mekong's lower tidal river and estuary.

Anthropogenic and natural impacts are reducing fluvial discharge and increasing estuarine intrusion in the Mekong River (Anh et al., 2018; Eslami et al., 2019b). The Mekong River basin, which is already heavily dammed, is expected to lose ~20% of its mean annual flow to reservoir storage by the year 2025 (Hecht et al., 2019), and tropical-cyclone tracks are likely shifting away from the Mekong Basin (Redmond et al., 2015). These changes reduce the amount of sediment transported downriver (Kondolf et al., 2014; Darby et al., 2016), thus contributing to observed subsidence rates of ~1.6 cm yr^{-1} in the lower delta (Erban et al., 2014).

In an effort to predict hydrodynamic and morphologic impacts of future changes in river discharge, numerous numerical models have been developed to characterize water flux (Xing et al., 2017; Eslami et al., 2019a) and sedimentation (Tu et al., 2019) in the delta and inner continental shelf. However, these models do not yet have the ability to resolve 3-dimensional flux of cohesive sediment over <100-m horizontal scales or <1-m vertical scales. To validate and refine such models, observations of sediment-flux patterns at channel bifurcations, as well as aggregate resuspension and settling data, are needed.

2.3 METHODS

This study focuses on hydrodynamics and suspended-sediment dynamics present during the dry season (November to March), when sediment is imported into the channel from offshore. During this time

of channel-bed aggradation, the channel beds are comprised of soft mud, suspended sediment is largely aggregated, and the estuary is partially mixed.

2.3.1 *Data Collection*

Vessel-based data were collected during a spring tide in March 2015. The research vessel repeatedly traversed a transect just upriver of where the Sông Hậu branches around the island called Cù Lao Dung to form the Định An and the Trần Đề distributaries (Figure 2.1). In one channel-traverse direction, water velocity (RD Instruments Acoustic Doppler Current Profiler, 600 kHz) and bathymetry (R2SONIC 2020 Multibeam, 100 kHz) were continuously recorded. Along the return traverse, in addition to collecting velocity and bathymetry data, the vessel stopped to perform casts over four stations, including one over the deepest subchannel (~12 m) and one over the shallowest subchannel (~8 m), hereafter referred to as the deep station and the shallow station. Casts recorded conductivity-temperature-depth (RBR XRX−620 CTD, 6Hz), optical backscatter (Campbell Scientific OBS 3+, 6 Hz), and grain-size distribution (Sequoia Scientific LISST-100X Type C, 2.5-500 µm size range).

The station locations were strategically chosen; the deep subchannel flows into the larger Định An distributary while the shallow subchannel flows into the smaller Trần Đề distributary. Thus, suspended-sediment characteristics observed within each subchannel are assumed to be those that are transported to the distributaries from the bifurcation during ebb flows, and from the distributaries to the bifurcation during flood flows. Data collected from the two left-most stations associated with the mid-depth subchannel are not discussed at length here due to their complex bathymetry and flow patterns; a mid-channel island is immediately upstream of these stations in addition to the bifurcating flow downstream of them.

At each station, and throughout the broader tidal river to estuarine reach (McLachlan et al., 2017), water samples were collected throughout the water column with a ~4 L Niskin sampler. Many of these samples (n=135) were immediately and gently poured into an on-board settling chamber (220×145×2 mm) and video recorded (Olympus Stylus TG-3; 1920×1080 resolution), following the design developed by Sternberg et al. (1996). All other water samples (n=174) were filtered, dried, and weighed to calibrate OBS voltage responses with suspended-sediment concentrations through linear regression (r^2=0.78).

2.3.2 *Data Processing*

To quantify instantaneous and residual fluxes of water and sediment across the entire transect, data were strategically extrapolated into regions where no data was collected. ADCP blanking regions were filled by assuming uniform velocity profiles near the surface and a no-slip condition near the bed. To assign SSC values along the transect between cast locations, SSC measurements were linearly interpolated

between casts and extrapolated to the channel banks. Then, transect-wide suspended-sediment fluxes were calculated as the product of along-channel velocity and sediment concentration. To calculate residual fluxes, these instantaneous fluxes were integrated across the transect and over the observed tidal cycle, as described and further discussed in McLachlan et al. (2017). Processing and analysis of the multibeam bathymetry data are reported in Allison et al. (2017).

For station-specific analysis, velocity data collected within 50 m of each station were averaged and paired with concurrent casts. Near-bed shear stress (τ) at each station was calculated with the Quadratic Stress Law,

$$\tau = \rho C_d \bar{u}^2 \,, \tag{2.1}$$

where ρ is the fluid density, $\bar{u}$ is the mean flow velocity at 2.5 m above the bed, and C_d is the drag coefficient. Drag coefficients were estimated using an observed correlation with bed type at this location during a previous wet-season field campaign (September-October 2014). During this previous study, drag coefficients were calculated from near-bed shear velocities found using the Law of the Wall (McLachlan et al., 2017).

Settling-chamber videos were processed to calculate both particle diameter (d) and settling velocity (W_s) of suspended particles. The best seven seconds of each video, meaning the best focused with the least turbulence, were selected for analysis and subsequently split into 21 frames (3 fps). These frames were then converted to grayscale, and successively differenced to remove stationary objects, leaving only moving sediment particles. The differenced frames were then converted to black-and-white binary images. Pixel sizes were generally <10 μm, and particles smaller than three pixels in diameter were removed from binary images due to their tendencies to blink in and out of successive frames.

Individual particles were identified and tracked through successive frames following the methods of Larsen et al. (2009). Perimeter, pixel count, equivalent diameter, minor axis length, and major axis length were found for each particle in a frame. These properties were then demeaned and equally weighted for each particle. Particles were tracked by finding the most similar particle in the next frame near the original and within a threshold for each particle property. Mean particle settling velocities and sizes were determined by averaging downward stepwise velocity and equivalent diameter from each frame. Finally, particles with stepwise velocities not within 2.5 standard deviations of the mean were deemed unsuccessfully tracked.

Particle tracking was considered successful if a particle was identified and tracked through at least 3 frames. The success rate of particle identification and tracking varied with the quality of the video. Factors such as camera focus, lighting shifts, and horizontal currents caused by boat motion each decrease the likelihood of correctly tracking particles. For the best quality videos (n=25), the tracking of individual

particles >25 μm was successful in 75% of cases on average. Only these videos were used to correlate particle diameter with settling velocity and then calculate effective density (ρ_e) using a rearranged Stoke's equation,

$$\rho_e = \rho_s - \rho_w = \frac{18 W_s \mu}{g d^2}, \tag{2.2}$$

where ρ_s is density of the settling particle, ρ_w is density of the water, μ is dynamic viscosity of the water, and g is gravitational acceleration. This method did not evaluate suspended particles finer than fine silt (<25 μm); these unobserved particles would likely have W_s < 0.01 mm s^{-1} and, thus, would not meaningfully contribute to the depositional fluxes (Soulsby et al., 2013).

To obtain grain-size distributions, LISST casts were processed using the Sequoia Scientific MATLAB® workflow with the random grain shape method. Data collected in the upper 0.25 m of the water column were excluded to remove the influence of near-surface bubbles. The LISST does not differentiate between discrete grains and aggregated particles, so to convert particle volume to particle mass, the correlation between particle diameter and effective density observed in the settling chamber was used. The mass settling flux (MSF) was then calculated, assuming spherical particles.

The mass settling flux is the product of settling velocity and mass concentration and quantifies the rate at which suspended sediment moves toward the bed, disregarding the resuspension effects of buoyancy and turbulence. Thus, *MSF* becomes the potential depositional flux near slack water. The mass settling flux is the product of settling velocity and mass concentration and quantifies the rate at which suspended sediment moves toward the bed, disregarding the resuspension effects of buoyancy and turbulence (Fennessy et al., 1994; Manning, 2002; Soulsby et al., 2013). Thus, *MSF* becomes the potential depositional flux near slack water. To provide a single instantaneous MSF for a population of particles distributed throughout the water column with varying sizes and effective densities,mean MSF was calculated as the depth-normalized vertical integration of summed fluxes for five grain-size classes (0-40 μm, 41-60 μm, 61-80 μm, 81-100 μm, and >101 μm), using each class's average settling velocity,

$$\overline{MSF} = \frac{1}{Z}\int_0^Z \sum_D W_{sD}\, SSC_D\, dz, \tag{2.3}$$

where Z is total water depth, z is height above the bed, and D is the grain-size class.

The degree of aggregation through the water column was also quantified by differencing the percent mass observed in each of 50 depth bins with the OBS from those observed with the LISST, which derives particle volume and assumes a constant particle density. Suspended-sediment concentrations near the bed of the shallow station were often so large that LISST transmission became unreliable (e.g., fell

below 15%) according to instrument specifications. At these times, grain-size distribution, $\overline{MSF}$, and the degree of aggregation could not be calculated.

The impact of sediment and velocity gradients on vertical stratification was characterized using the gradient Richardson number (Ri_g),

$$Ri_g = \frac{N^2}{S^2}. \tag{2.4}$$

A gradient Richardson number of approximately 0.25 is the empirically demonstrated threshold for stratification (West & Oduyemi, 1989; Adams et al., 1990; Winterwerp, 2001), with smaller values promoting mixing in an unstable water column and greater values promoting stable stratification. The buoyancy frequency (N) quantifies the magnitude of vertical density stratification,

$$N = \sqrt{-\frac{g}{\rho}\frac{\partial \rho}{\partial z}}, \tag{2.5}$$

and the strain rate (S) is the vertical gradient in along-channel velocity ($\partial u/\partial z$), where u is the flow velocity and z is height above the bed. For this calculation, measured water temperature, salinity, and suspended-sediment concentrations were included in fluid density (ρ) calculations, assuming a particle density of 2.65 g cm^{-3}. To smooth along-channel velocity and density profiles before calculating their vertical gradients, such that inconsequential high-frequency variations would not impact calculations of Ri_g or N, these data were interpolated into 50 fractional depth bins and then further smoothed with a moving average over three depth bins for velocity and five depth bins for density.

2.4 RESULTS

During this dry-season field campaign, the transect was predominately a tidal river; flow velocities reversed during flood tides and no salinity was present. Integrating across the transect and over the 24.8-hour tidal cycle, instantaneous water discharge ranged from -1.6x10^4 m^3 s^{-1} to 1.6x10^4 m^3 s^{-1}, with a residual discharge of 1.5x10^3 m^3 s^{-1}. Tidally averaged, instantaneous suspended-sediment discharge ranged from -5.0x10^2 kg s^{-1} to 7.2x10^2 kg s^{-1}, with a residual discharge of 75 kg s^{-1}. For a short period of time (~1-2 hrs) at the end of flood tide, salinity near the bed increased to ~1 only in the deep subchannel. Water temperature also varied little, ranging from ~28˚C to ~29˚C throughout the period of data collection.

2.4.1 *Tidal-Velocity Asymmetry and Shear Stress*

Velocity profiles indicate that hydrodynamics of the deep and shallow subchannel stations differed (Figure 2.2). For the deep station, along-channel velocity was similar during ebb and flood flows, reaching maximums of ~1 m s^{-1} in both flow directions. Maximum near-bed shear stresses, calculated at 2.5 meters above the bed, were ~2 Pa. In contrast, tidal asymmetry was observed over the shallow station. Maximum ebb flow velocity exceeded 1 m s^{-1}, while flood velocities were always <0.8 m s^{-1}. For similar maximum velocity magnitudes, near-bed shear stresses over the shallow subchannel were generally greater than those over the deep subchannel, reaching ~3 Pa in both flow directions.

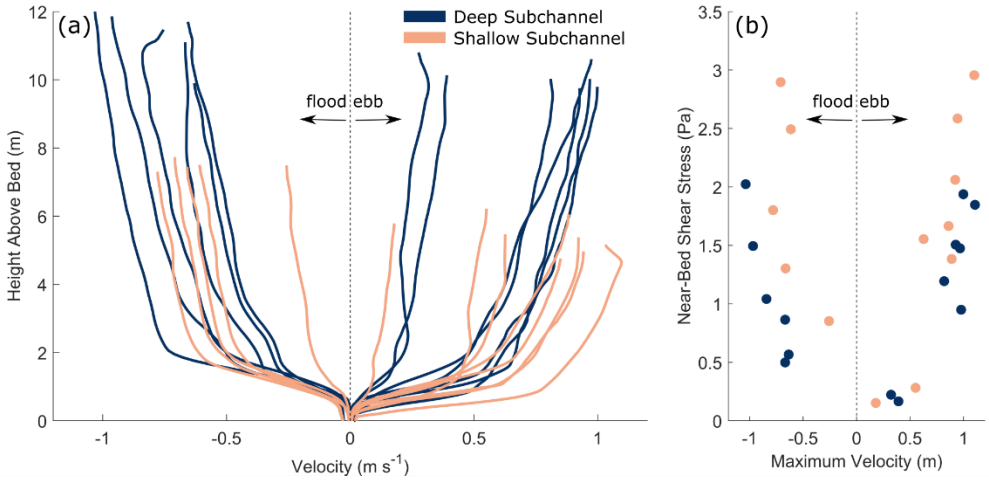

Figure 2.2. A) Along-channel velocity profiles associated with each cast. B) Maximum velocity anywhere in the water column during each cast plotted against the concurrent near-bed shear stress, calculated at 2.5 meters above the bed. Data from the deep subchannel are shown in dark blue, and data from the shallow substation are shown in light orange. Negative velocity values indicate flood flows, and positive velocity values indicate ebb flows.

2.4.2 *Suspended-Sediment Characteristics*

Vertical profiles of suspended sediment obtained from the OBS also indicate differences between the deep and shallow subchannel stations (Figure 2.3). Over the deep station, the greatest observed SSC was ~350 mg L^{-1}, and suspended sediment was well mixed vertically during both ebb and flood flows. Concentrations near the bed rarely exceeded those near the surface by more than 100 mg L^{-1}.

Sediment concentrations were more vertically stratified over the shallow station. During ebb flows, suspended-sediment concentrations near the surface were 45-85 mg L^{-1}, and gradually increased with depth. Near-bed SSC during ebb was commonly >350 mg L^{-1}, with a maximum of 800 mg L^{-1}. During flood flows,

SSC was generally well mixed at depth, with each cast averaging between 140 and 300 mg L^{-1}, but decreased in a stepwise manner to ~115 mg L^{-1} within 1 m of the water surface.

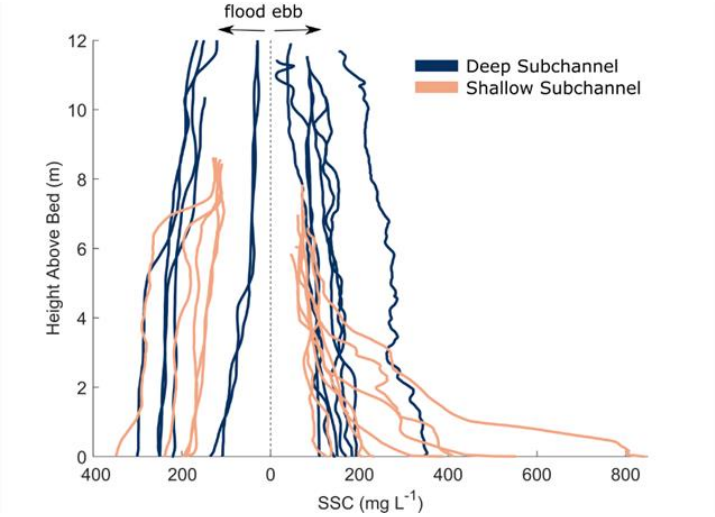

Figure 2.3. Suspended-sediment concentration profiles of each OBS cast. Data from the deep subchannel are shown in dark blue, and data from the shallow subchannel are shown in light orange.

The LISST observed clay-, silt- and fine-sand-sized particles in suspension, and the vertical distribution of particle sizes displayed similar patterns to those of SSC. Over the deep station, both typical-sized particles (25-50 μm) and the largest particles (>50 μm) were well mixed through the water column during ebb and flood flows (Figure 2.4). Over the shallow station, however, these particles were well mixed during flood flows but more concentrated in the lower half of the water column during ebb flows (Figure 2.5). Overall, the median diameter of observed particles for each cast (D_{50}) over the deep station was slightly larger than that over the shallow station, though that of the 90th percentile (D_{90}) was similar for both stations.

The effective density calculated for >25-μm particles observed in the settling chamber was less than that expected from discrete quartz grains (ρ_e=1.65 g cm^{-3}) (Figure 2.6). Instead, most particles had effective densities of 0.05-0.3 g cm^{-1}. Effective densities were negatively correlated with particle size, such that the largest particles had the smallest effective densities, as is expected for aggregated particles

The degree of aggregation represented in each depth bin also showed differences between the two stations (Figure 2.7). Over the deep station, the degree of aggregation was not well correlated with either tidal phase or depth. In contrast, over the shallow station, aggregation degree was most prominent at depth and was positively correlated with near-bed shear stress. This measure of aggregation produced the largest values near the bed during ebb flows over the shallow station, the same tidal phase and location with the largest suspended-sediment concentrations.

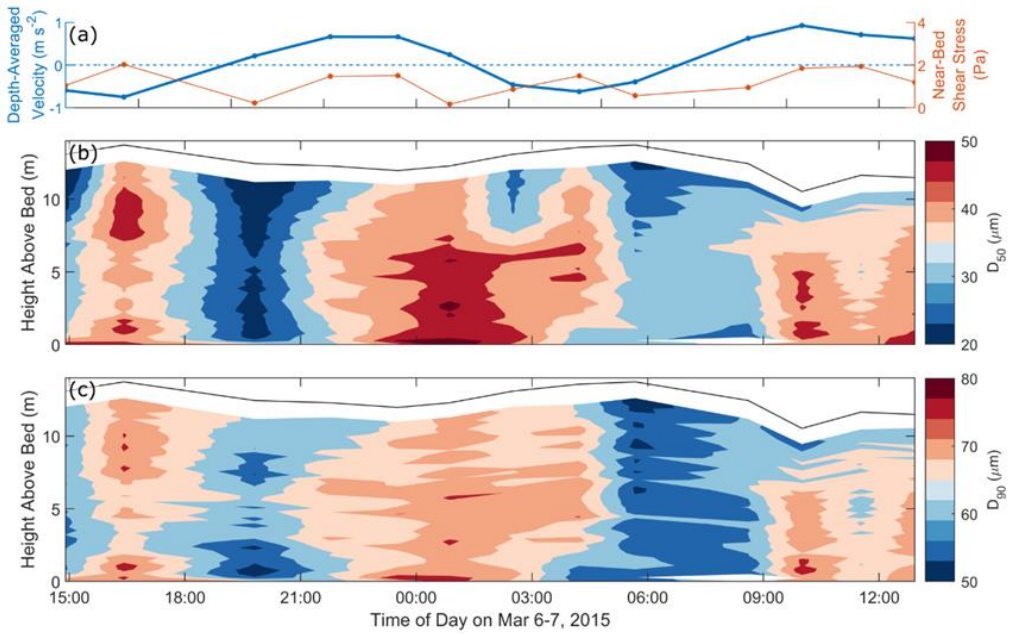

Figure 2.4. Time series from the deep subchannel of A) depth-averaged velocity (bold blue line) and near-bed shear stress (thin orange line), B) median suspended grain-size diameter, and C) the 90th percentile of suspended grain-size diameter. For panels B and C, data were collected with the LISST, and black lines represent the water surface.

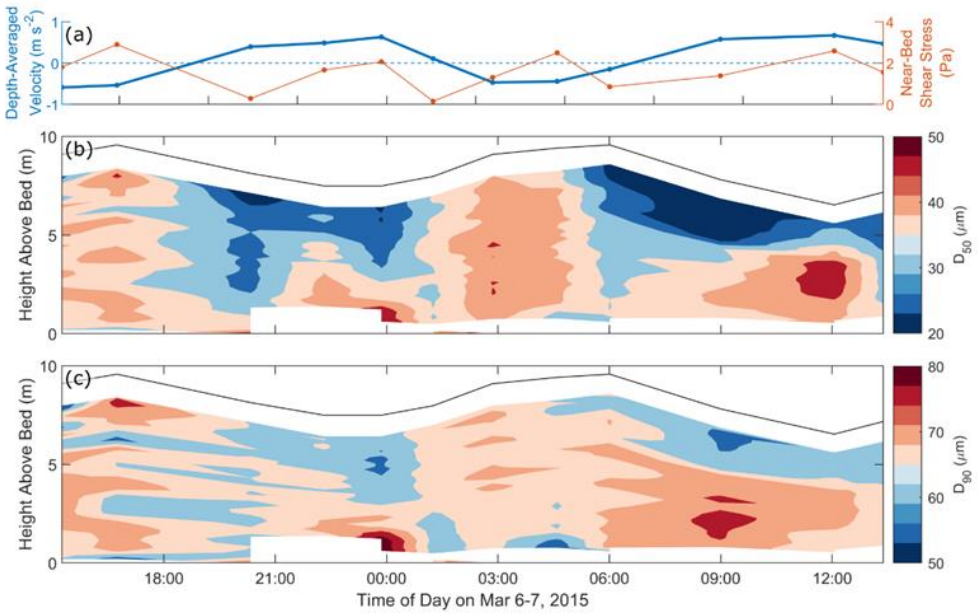

Figure 2.5. Time series from the shallow subchannel of A) depth-averaged velocity (bold blue line) and near-bed shear stress (thin orange line), B) median suspended grain-size diameter, and C) the 90th percentile of suspended grain-size diameter. For panels B and C, data were collected with the LISST, and black lines represent the water surface.

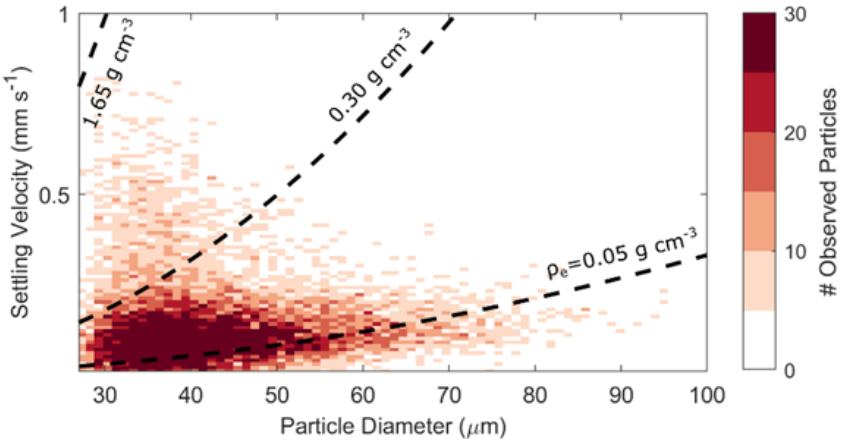

Figure 2.6. Observed relationships between particle diameter and settling velocity from settling-chamber videos. Dashed black lines represent relationships expected from particles with indicated effective densities (ρ_e), using Stoke's settling equation for discrete spherical particles.

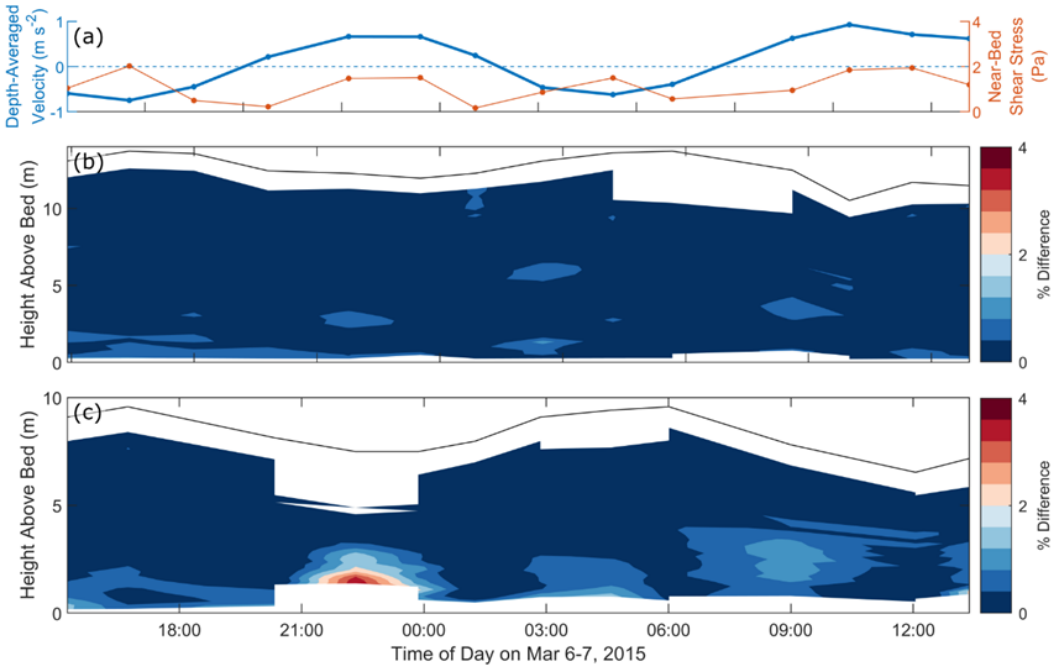

Figure 2.7. Time series of A) depth-averaged velocity (bold blue line) and near-bed shear stress (thin orange line) from the deep subchannel, B) degree of aggregation within the deep subchannel, and C) degree of aggregation within the shallow subchannel. For panels B and C, black lines represent the water surface. The degree of aggregation is quantified by differencing the percent mass observed in each of 50 depth bins with the OBS from those observed with the LISST.

2.4.3 *Suspended-Sediment Flux*

Integrating the along-channel flux of suspended sediment over two consecutive semidiurnal tidal cycles (Figure 2.8) reveals that residual sediment flux during this study was near zero over the deep station, with a slight tendency to export in the upper water column and import in the lower water column. Over the shallow station, residual flux magnitudes were larger (order 10 g m^{-2} s^{-1}) and this vertical pattern was reversed; sediment was imported in the upper water column and exported near the channel bed. For comparison, these data from the 2015 dry season are plotted with those collected during the 2013 dry season when the bifurcation was an estuary (Nowacki et al., 2015) (Figure 2.8), as discussed further in later sections.

Integrating these residual sediment fluxes through the water column produces a relatively small seaward export over the deep station (11 g m^{-1} s^{-1}) and a larger import over the shallow station (-30 g m^{-1} s^{-1}). However, these residual fluxes are two orders of magnitude smaller than maximum instantaneous fluxes, so confidence in exact values is low.

Patterns in mass settling flux, which becomes the depositional flux near slack water, are similar between the two stations (Figure 2.9). Over both stations, maximum $\overline{MSF}$ is ~0.3 kg m^{-2} hr^{-1}. Furthermore, $\overline{MSF}$ is dominated by fine particles throughout the entire tidal cycle. Particles <40 μm persistently compose >90% of the $\overline{MSF}$, while particles >80 μm never compose >2%.

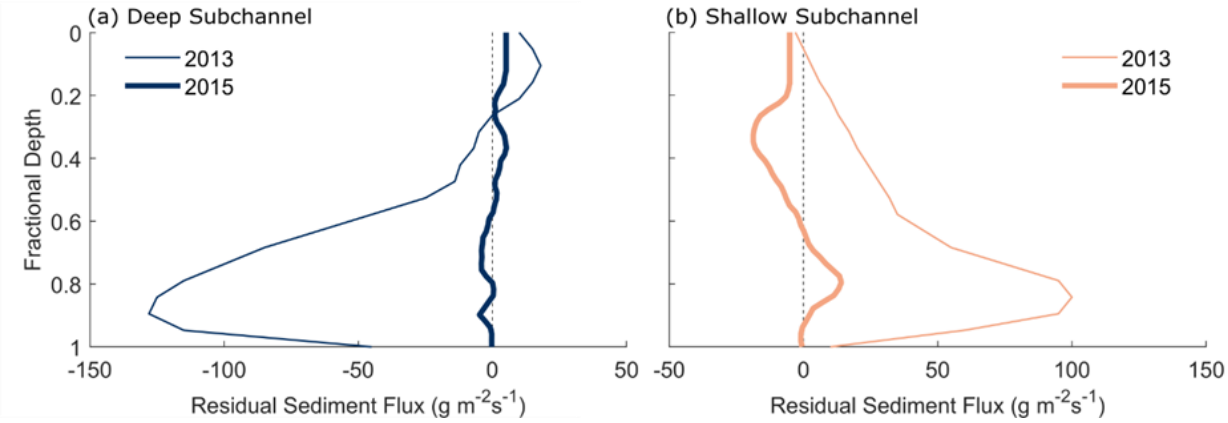

Figure 2.8. Residual along-channel sediment fluxes for the A) deep subchannel and B) shallow subchannel during a previous study conducted in the 2013 dry season, when the transect was an estuary, and the 2015 dry season when the present study was conducted, and when the transect was a tidal river. Data from 2013 are from Nowacki et al. (2015).

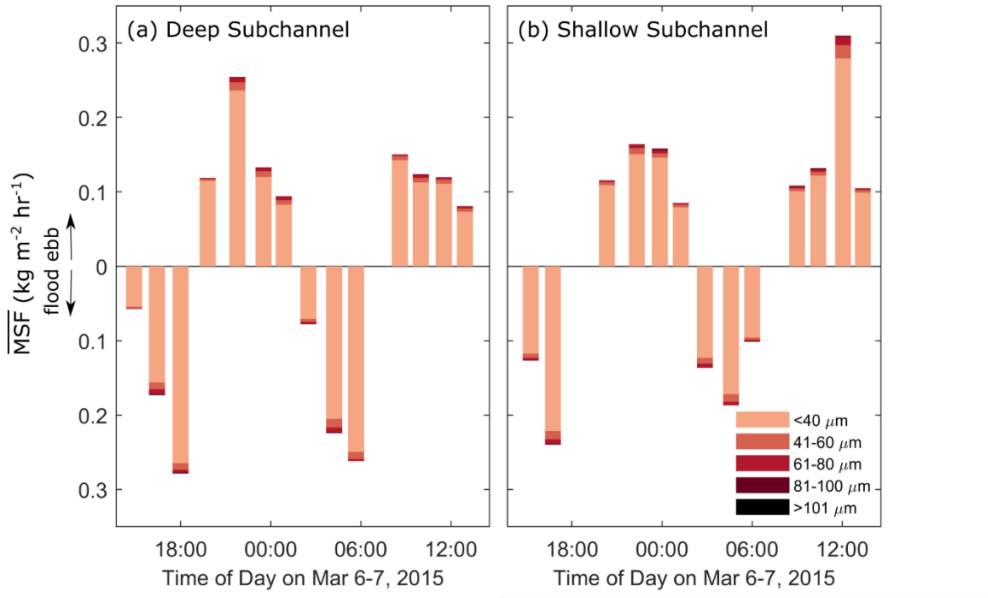

Figure 2.9. Time series of instantaneous mean mass settling fluxes for the A) deep subchannel and B) shallow subchannel. Bars are sectioned by color to indicate the component fluxes of each grain-size range. Mass settling fluxes were calculated from particle settling velocities and effective densities measured in the settling-chamber videos and particle sizes measured with the LISST.

2.4.4 *Vertical Stratification*

Stratification was assessed with three parameters: 1) buoyancy frequency (N), which quantifies density stratification, 2) strain rate (S), which quantifies shear in along-channel velocity, and 3) the gradient Richardson Number (Ri_g), which quantifies the ratio of the previous two terms. Again, the two stations show different patterns. Over the deep station (Figure 2.10), density stratification is relatively minor with N<0.03 throughout the water column over the tidal cycle. Strain rate is greatest near the bed and has a maximum of 1.1 s^{-1} during the fastest tidal velocities. As a result of this strong near-bed strain rate, gradient Richardson numbers are relatively low, rarely exceeding 0.01 within the lower 10% of the water column or 0.25, the critical value, within the lower 30%.

In contrast, the shallow subchannel (Figure 2.11) shows larger magnitudes of density stratification in the lower water column; N=0.06 s^{-1} during ebb flows when near-bed SSC is >350 mg L^{-1}. Strain rates near the bed tend to be slightly larger in magnitude over the shallow station than over the deep station, exceeding 1.2 s^{-1} during the fastest ebb velocities. During ebb flows, when density stratification is relatively strong, the greatest strain rate appears to be raised in the water column away from the channel bed. During these time periods, Ri_g closest to the bed reaches 0.1, and just before these time periods, Ri_g within the lower 30% of the water column exceeds 0.25.

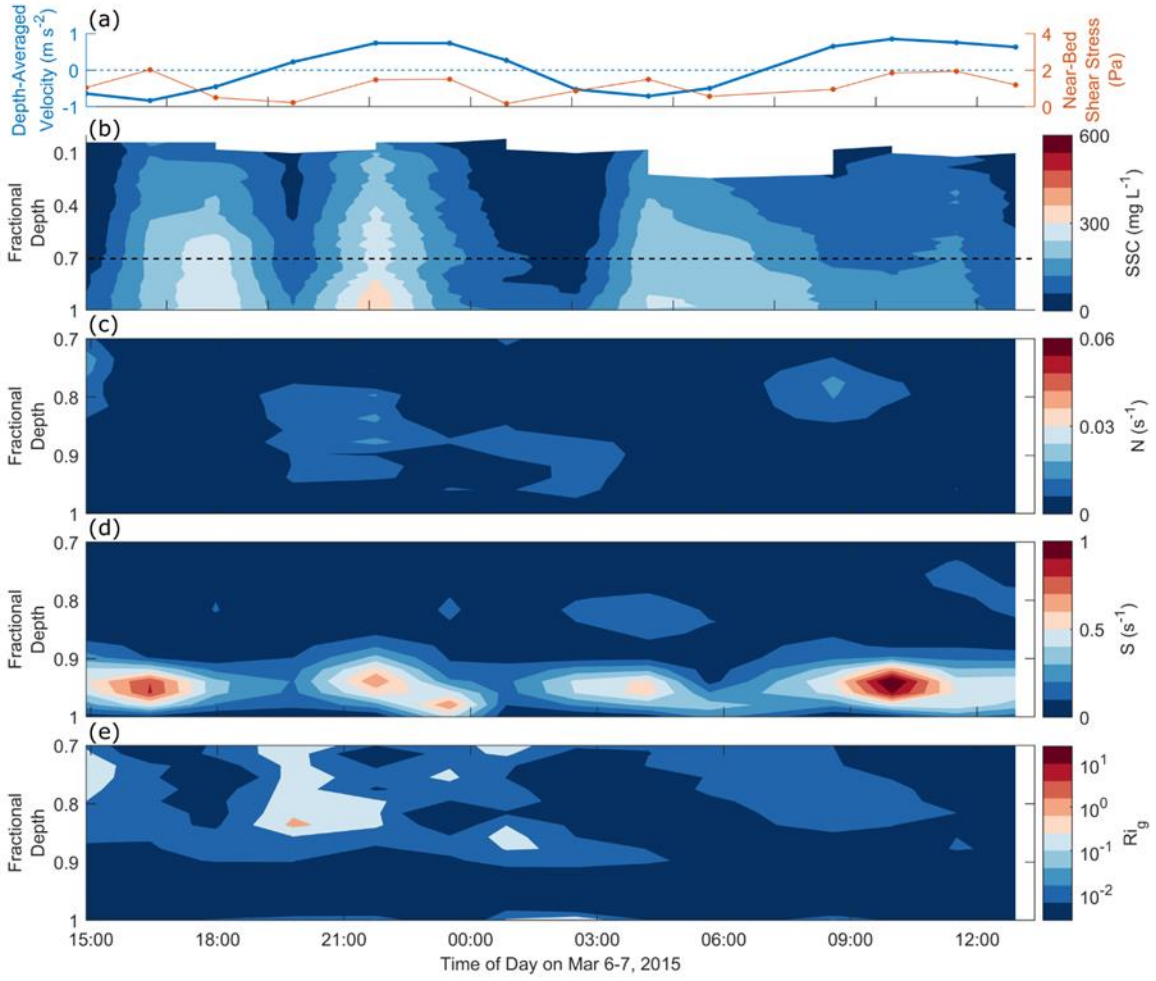

Figure 2.10. Time series from the deep subchannel of A) depth-averaged velocity (bold blue line) and near-bed shear stress (thin orange line), B) SSC through the entire water column, C) buoyancy frequency (N) in the lower water column, D) strain rate (S) in the lower water column, and E) gradient Richardson numbers (Ri_g) in the lower water column. The dashed line in panel B indicates the upper y-axis limit for panels C, D, and E.

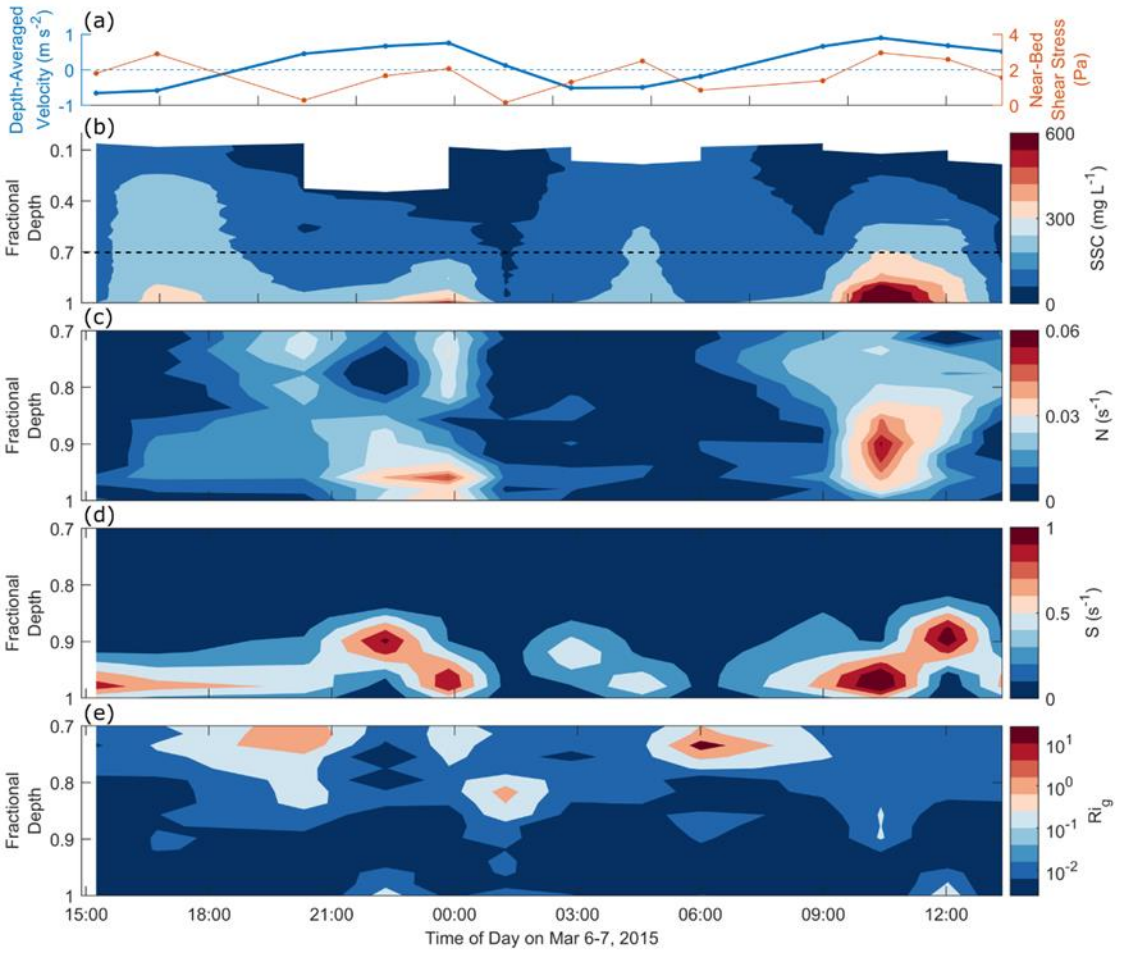

Figure 2.11. Time series from the shallow subchannel of A) depth-averaged velocity (bold blue line) and near-bed shear stress (thin orange line), B) SSC through the entire water column, C) buoyancy frequency (N) in the lower water column, D) strain rate (S) in the lower water column, and E) gradient Richardson numbers (Ri_g) in the lower water column. The dashed line in panel B indicates the upper y-axis limit for panels C, D, and E.

2.5 DISCUSSION

2.5.1 *Depth Impacts on Suspended-Sediment Distribution in the Tidal River*

To better understand and accurately predict sediment-exchange processes at channel bifurcations with bidirectional flow, the impact of channel depth on sediment distribution in the water column must first be accurately characterized. Here, we discuss the impact of subchannel depth on aggregation, vertical mixing, and flux partitioning at the distributary bifurcation when it is a tidal river. We then contrast these

processes to those present when the bifurcation is an estuary and apply our conclusions to other deltas with similar environmental conditions.

2.5.1.1 Sediment Aggregation and Settling

Suspended-sediment aggregation increases particle size and promotes sediment settling toward the bed, though the direct impact of subchannel depth on local suspended-sediment particle size appears to be minimal. Similar ranges of suspended-sediment particle size were observed over both stations (Figure 2.4 and Figure 2.5). This result is not unexpected in a channel with complex bathymetry such as the Sông Hậu (Allison et al., 2017) because particles are advected over terrains with varying depths, bedforms, and bed-sediment characteristics before reaching the transect. Particle characteristics are often a product of their recent advective pathways more than their instantaneous circumstances (Sassi et al., 2013; Schwarz et al., 2017).

Furthermore, the suspended load coarser than 25 μm is assumed to be dominated by aggregates, specifically microflocs, because the effective densities of almost all observed settling particles (ρ_e = 0.05-0.30 g cm^3) were less than those expected from discrete quartz grains (ρ_e = 1.65 g cm^3) (Figure 2.6). For aggregates, maximum particle sizes are dependent on many factors along their flux pathways, including bed-sediment availability, particle size, and composition, and the presence of biological and physiochemical binding agents. Aggregate formation and break up are additionally moderated by turbulent shear stress and sediment concentration in the water column (Soulsby et al., 2013).

Sediment aggregation was largely modulated by suspended-sediment concentration. This relationship is illustrated in Figure 2.7, where the degree of aggregation remains constant with depth over the deep station, which had vertically well-mixed SSC, but increases with depth over the shallow station, which had relatively large SSC confined near the bed. While the degree of particle aggregation was correlated with SSC, which is impacted by channel depth as discussed later, most observed settling velocities were in a narrow range (<0.25 mm s^{-1}) (Figure 2.6). Furthermore, >90% of the mean mass settling flux over each station was attributed to particles <40 μm (Figure 2.9), giving the less frequent formation of larger microflocs and macroflocs minimal influence on potential sediment deposition. As a result, total suspended load, rather than aggregate size, can be assumed as the dominant control on mass settling flux in tidal rivers that are dominated by microflocs, like the Sông Hậu.

2.5.1.2 Flow Velocity and Sediment Mixing

Although channel depth did not directly influence aggregate size, it did meaningfully impact along-channel flow velocity, with important implications for sediment-transport potential of each subchannel. As

rivers approach base level, their cross sections widen, decreasing the flow velocity necessary to accommodate the fluvial water discharge (Langbein, 1963; Wright et al., 1973). This widening is visible in the lower Sông Hậu upstream of its bifurcation (Figure 2.1). Fluxes around these bifurcations are often mutually evasive, meaning that minimal water exchange occurs between subchannels due to counter-rotating secondary flow cells (Sassi et al., 2013). Therefore, increases in subchannel cross-sectional area moving downstream must be partially accommodated by reductions in flow velocity. Because flow through the transect is sectioned into three subchannels, the large cross section of the deepest subchannel allows for a larger magnitude decrease in ebb flow velocity. In contrast, the shallowest subchannel has a relatively confined cross section and creates faster ebb velocities.

Flow velocity was an important factor for suspended-sediment distribution. Suspended sediment within the deep subchannel was well-mixed vertically during both ebb and flood flows, suggesting that the large depths produced large inertial forces relative to viscous forces. Because sediment resuspension was similar during ebb and flood flows, the residual sediment flux was near zero with a relatively minor export (Figure 2.8a). The reduced depth of the shallow subchannel did not always create conditions for a well-mixed water column. During flood flows, suspended sediment was well mixed through the lower 85% of the water column. In contrast, large suspended-sediment concentrations were confined near the bed during ebb flows, suggesting that sediment-induced stratification suppressed turbulence, overcoming the relatively large ebb flow velocities and resulting in residual sediment import (Figure 2.8b) due to tidal pumping and particle settling lag.

2.5.1.3 Sediment Transport in the Deep Subchannel

The deep subchannel exhibited little tidal asymmetry in profiles of velocity (Figure 2.2) and suspended sediment (Figure 2.3). In effect, little difference is observed in buoyancy frequency, strain rate, or gradient Richardson Numbers between flood and ebb flows (Figure 2.10). The consistently well-mixed SSC profiles produce $N<0.02\ s^{-1}$, and strain rates near the bed always exceed $0.5\ s^{-1}$ during maximum flood and ebb velocities, with maxima at 95% water depth. This combination of small buoyancy frequencies and strong strain rates produces gradient Richardson Numbers almost always less than 0.25, which indicates an unstable water column and promotes vertical mixing. The tidal symmetry results in minimal residual sediment flux. The slight import of sediment at depth and export near the surface (Figure 2.8a) resembles estuarine exchange flow (Geyer & MacCready, 2014) and is likely a result of the estuary briefly intruding up to the transect near the end of flood tide (McLachlan et al., 2017).

2.5.1.4 Sediment Transport in the Shallow Subchannel

The shallow subchannel is likewise conducive to vertically mixing sediment during flood-tide flows, and sediment is well mixed through much of the water column. Sediment is not well resuspended into the upper water column (Figure 2.3), perhaps because shallower depths and lesser flood velocities (Figure 2.2) produce weaker inertial forces. During flood, strain rate near the bed exceeds 0.8 s^{-1}, strengthening resuspension potential near the bed, while the buoyancy term N stays below 0.2 s^{-1} due to little suspended-sediment stratification (Figure 2.11). In effect, the gradient Richardson number in the lower water column rarely exceeds 0.25 during the beginning of flood flows. During this time, sediment is resuspended from the bed and vertically mixed up through the water column.

When flow velocities increase during ebb flows, enough sediment is resuspended from the bed to produce large vertical gradients in SSC (Figure 2.3). During ebb flows, strain rate near the bed often exceeds 0.9 s^{-1}. Around these times, buoyancy frequency due to sediment stratification is large, exceeding 0.3 s^{-1}. The maximum strain rates occur farther from the bed, and strain rates approach zero at the bed (Figure 2.11). In effect, sediment-induced stratification inhibits the mixing of momentum and sediment from near the bed to the surface of the water column, and the carrying capacity of the upper layer is reduced (West & Oduyemi, 1989; Adams et al., 1990; Winterwerp, 2001). The suspended-sediment concentration present prior to the collapse of the vertical turbulence field, i.e. Ri_g>0.25, is referred to as the saturation concentration. Here, the saturation concentration is ~400 mg L^{-1}, which is comparable to other observed instances of sediment-induced stratification at just a few hundred milligrams per liter (West & Oduyemi, 1989; Adams et al., 1990; Winterwerp, 2001).

Because suspended sediment in the shallow subchannel was well mixed during flood flows and confined near the bed during ebb flows, and sediment in the upper water column is advected at faster velocities than that in the lower water column, a net landward sediment flux was observed over the shallow subchannel station. Asymmetry in settling lag times likely also contributed to the landward tidal pumping of sediment, as has commonly been observed in many tidal environments (e.g., Postma, 1961; Pritchard, 2005; Chernetsky et al., 2010). As flood velocities wane and strain rate decreases beyond its ability to maintain sediment in suspension, sediment settles toward the bed. Sediment high in the water column has a greater distance to settle, thus having more time to be advected landward at the end of flood tide. In contrast, more suspended sediment is confined near the bed during ebb flows, resulting in a shorter distance to settle through the water column and less time to be advected seaward as ebb velocities wane.

2.5.1.5 Sediment-Flux Partitioning in the Tidal River

In summary, when river discharge is great enough to confine saline water and estuarine processes downstream of the Sông Hậu bifurcation, the region is a tidal river. The residual sediment flux is seaward in the deep subchannel where the water column is well mixed and landward in the shallow subchannel where sediment-induced stratification dampens turbulent mixing during ebb flows. In effect, sediment flux is directed upstream from the shallower Trần Đề distributary and downstream to the deeper Định An distributary, and a clockwise residual sediment flux toward the deeper distributary prevails (Figure 2.12).

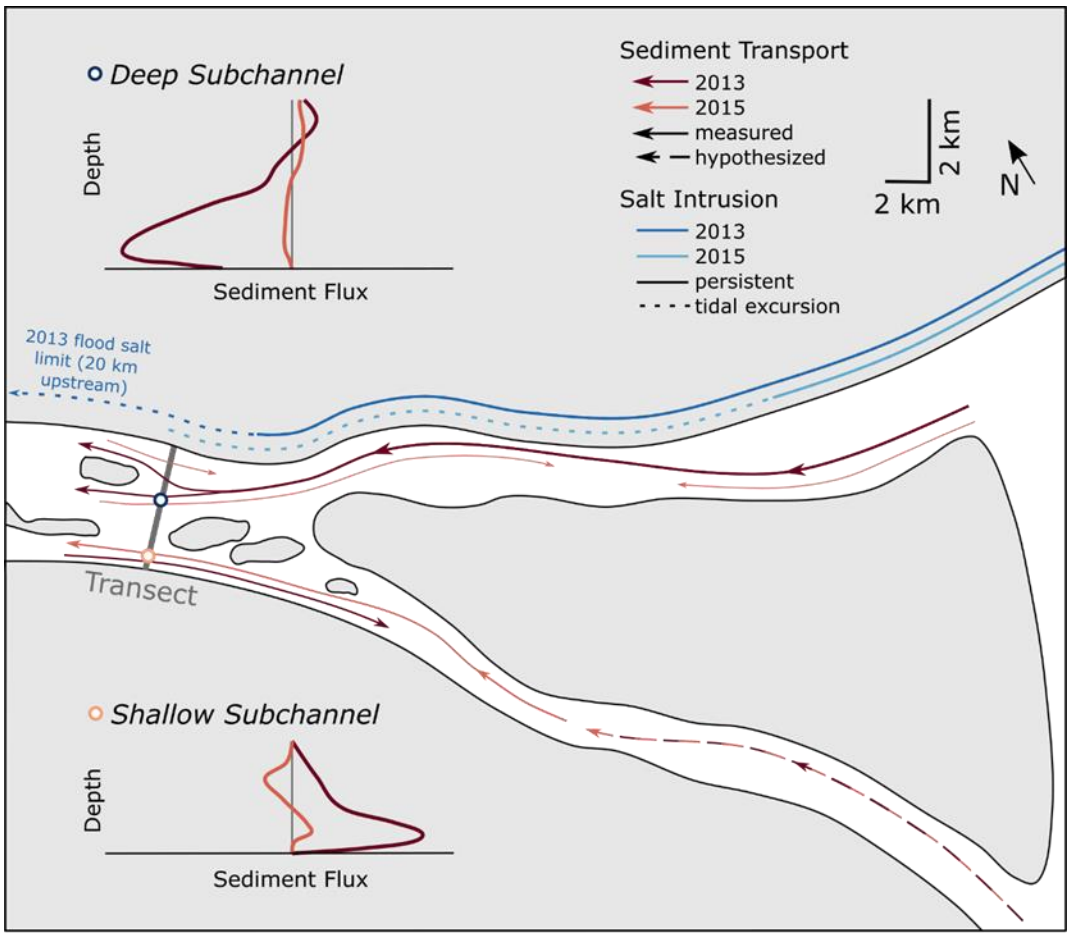

Figure 2.12. Schematic map of residual sediment transport pathways and salt intrusion during the dry seasons of 2013, when the transect was predominately an estuary, and 2015, when the transect was predominantly a tidal river. Flux magnitude is qualitatively illustrated with arrow thickness. Inset plots show vertical profiles of residual sediment flux for the deep and shallow stations; vertical grey lines divide landward flows to the left from seaward flows to the right. Data from 2013 are from Nowacki et al. (2015). Data from 2015 are from this study and McLachlan et al. (2017).

2.5.2 *Regime Impacts on Sediment-Flux Partitioning*

The boundary between the tidal river and estuarine regime is not static in tide-influenced distributaries such as the Sông Hậu, so it is important to understand how its migration may impact sediment dynamics through time and space. We accomplish this by comparing our results to those of others who evaluated sediment flux along this distributary at different times and locations when and where regimes were different.

Similar to subchannel depth, salinity regime has not been found to meaningfully influence the impact of sediment aggregation on deposition in this environment. While differences were observed in the size and settling velocity of suspended particles in the tidal river and downstream estuaries, these differences were slight. Particles are already aggregated into microflocs in the fresh tidal river, so further aggregation into larger microflocs and macroflocs once particles reach the saline estuary does not substantially increase their settling velocity; the vast majority of particles had settling velocities <0.5 mm s^{-1} regardless of particle diameter (Figure 2.6) (McLachlan et al., 2017). Because the mass settling flux is dominated by the smallest particles, which are most plentiful, the degree of aggregation can be excluded as a major factor in controlling the vertical sediment distribution and, thus, the longitudinal sediment flux in the lower Sông Hậu as it transitions from a tidal river to estuary. Instead, channel depth and its impact on mixing in both the tidal river and estuary largely controls the vertical distribution of along-channel sediment flux and, therefore, the sediment-flux partitioning around the mid-channel island.

Results here show that when the region upstream of the channel bifurcation is a tidal river, the tidally averaged suspended-sediment flux within the deeper subchannel is seaward and toward the deeper distributary. This flux pathway was not observed during a previous study conducted at the same transect in 2013 (Nowacki et al., 2015). Fluvial discharge was less in 2013, which allowed the estuary to propagate upriver past the bifurcation. Salinity at the transect averaged 2.5 PSU. A counterclockwise residual sediment flux was measured upstream of the channel bifurcation; sediment was imported from the deeper Định An distributary (-490 g m^{-1} s^{-1}) and exported to the shallower Trần Đề distributary (252 g m^{-1} s^{-1}) (Figure 2.12). We interpret that channel depth has a primary effect on this reversal in flux partitioning around the mid-channel island due to the inverse impact that channel depth has on vertical mixing in tidal rivers and estuaries.

When the lower Sông Hậu was an estuary during the dry season of 2013, baroclinic effects generally drove a residual landward flux of sediment in the lower water column and a seaward flux in the upper water column. These sediment-transport pathways are analogous to those of other coastal-plain estuaries (Meade, 1969) and are primarily a result of estuarine circulation. As such, the largest landward fluxes were in the deepest subchannels where the salt-wedge estuary was most stratified (Nowacki et al.,

2015). Specifically at the study transect, the landward residual sediment flux over the deep station (Figure 2.8a) was attributed to tidal pumping, whereas the seaward residual sediment flux over the shallow station (Figure 2.8b) was generally attributed to geographic complexity of the branching channel (Nowacki et al., 2015). Here, we associate that complexity with differing channel depths.

In many tide-influenced systems, disproportionate flux at channel bifurcations has been attributed to differing downstream channel lengths and sinuosities (Buschman et al., 2013) and sediment sorting by upstream meanders (Frings & Kleinhans, 2008; Sassi et al., 2013). Conclusions from this study, where the channels are relatively straight and downstream distributaries are similar in length, indicate that sediment-flux partitioning at channel bifurcations can also be a result of channel-depth impacts on flow velocity and vertical mixing and that these impacts differ in tidal-river and estuary regimes.

2.5.3 *Implications for Future Morphodynamics*

Here we have shown an instance where the direction of sediment circulation around the apex of a mid-channel island is reversed when the regime shifts from a tidal river to an estuary. This reversal is predicated to occur on differing subchannel depths and plentiful, erodible fine bed sediment, two requirements that are fulfilled at many other large, tropical deltas, including the Yangtze (Yang et al., 2015), Mahakam (Gastaldo et al., 1995), and Ganges-Brahmaputra (Haque et al., 2015). These deltas also share a present or predicted reduction in the fluvial discharge due to increasing dam installations and water-diversion projects (Milliman & Farnsworth, 2011; Syvitski & Kettner, 2011). Land subsidence (Syvitski et al., 2009) and reduced sand supply (Milliman & Farnsworth, 2011; Syvitski & Kettner, 2011) are also prevalent in the world's major tropical deltas, causing tidal rivers to deepen, tidal motion to amplify, and salinity intrusion to increase (Hoitink & Jay, 2016).

As the geographic locations of freshwater zones shift inland, channel bifurcations that are now predominately tidal rivers are expected to more commonly become estuaries. Figure 2.13 illustrates four large tide-influenced river deltas, including the Mekong River Delta, where many channel bifurcations lie near the modern limit of typical salt intrusion. For example, salinity in the Mekong Delta is presently increasing by 0.2-0.5 yr^{-1} (Eslami et al., 2019b), and within the next 45 years, salinity intrusion length in the largest distributary of the Mekong Delta could increase by 3.3-4.7 km (Anh et al., 2018). Similarly in the Ganges-Brahmaputra-Meghna delta, freshwater zones below the Meghna confluence are expected to disappear if upstream discharge reduces below one standard deviation of that measured in 2011 (Akter et al., 2019).

The reduction in river discharge and associated impacts on mixing and salt intrusion are not always equally partitioned between individual distributaries, as has been observed in many large deltas including

the Mekong (Eslami et al., 2019b) and the Yangtze (Qiu & Zhu, 2013). Thus, the future shifts in sediment partitioning between distributaries is expected to be spatially complex, though potentially similar overall, among these deltas. Results from this study indicate that these regime shifts could cause sediment to be rerouted toward shallower distributaries, perhaps promoting sediment retention and channel infilling. If so, these shallowing depths will have many biogeomorphological impacts that alter biologic habitat, including increased maximum velocity, increased salinity, and increased near-bed turbidity.

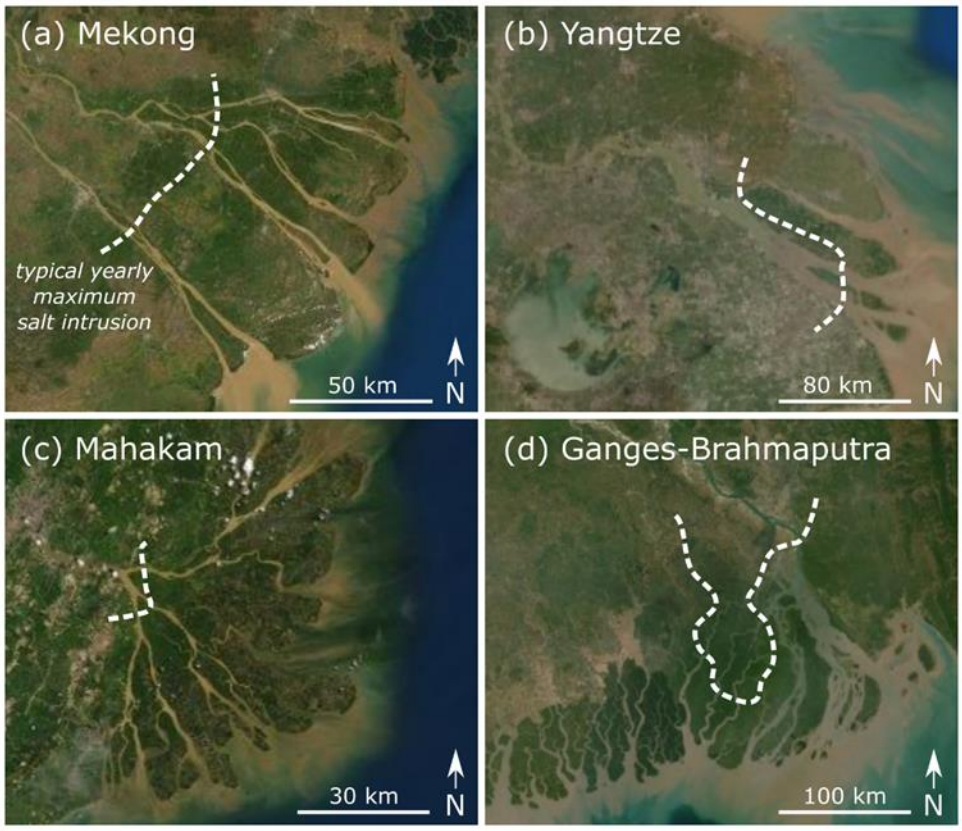

Figure 2.13. Maps of four tide-influenced deltas illustrating their typical yearly limit of maximum salt intrusion and channel-bifurcation geography. Salt-intrusion data from: Mekong (Wassmann et al., 2019), Yangtze (Zhang et al., 2011), Mahakam (Salahuddin, 2011; Budiyanto & Lestari, 2013) and Ganges-Brahmaputra (Akter et al., 2019).

However, the long-term sustainability of these feedbacks is unclear. A shallower channel depth and the potential associated increase in flow velocity may strengthen bed stress, increase bed erosion, and deter sediment deposition on the channel bed (Wolanski et al., 1996; Chernetsky et al., 2010), resulting in a negative feedback loop. Likewise, tidal propagation up the shallower channel will slow, leading to a larger hydrostatic pressure gradient along the shallow distributary than the deeper distributary and driving more fluvial discharge down the shallow distributary (Wagner & Mohrig, 2019), further increasing flow velocity

and erosion potential. A positive feedback loop is also possible; the reduced tidal prism that must be accommodated within the shallower channel may reduce bed erosion and promote sediment retention (Canestrelli et al., 2010; Li et al., 2017).

Both positive and negative feedbacks have been observed in tidal deltas. In the Kapuas River Delta (Kästner et al., 2017) and Berau River Delta (Buschman et al., 2013), where sediment supply to smaller distributaries is often limited, distributary depths downstream of channel bifurcations have become more similar over time (Buschman et al., 2013). In contrast, distributary depths have become more dissimilar in deltas with large sediment supplies. In the Yangtze Estuary, the relatively small North Branch has become narrower and shallower as the South Branch has deepened (Jiyu et al., 1985; Yang et al., 2015). Likewise, the Ba Lai distributary, a minor distributary in the Mekong Delta, was abandoned due to sediment infilling within the past several centuries (Tamura et al., 2012). Additionally, historical aerial imagery suggests that the Trần Đề distributary is shrinking due to sediment infilling (Nowacki et al., 2015). While the net result of these possible feedbacks is still unknown for most deltas, many studies agree that seasonal trapping of fine-grained sediment within tide-influenced deltas is likely to increase (McLachlan et al., 2017; Nienhuis et al., 2018), and we conclude that this increased trapping may be disproportionately large in relatively shallow channels.

2.6 CONCLUSIONS

Channel bifurcations control the division of water and sediment across downstream distributaries. In tidally influenced deltas, these bifurcations add complexity to vertical mixing and longitudinal sediment flux, and, thus, control sediment distribution and morphologic development of tidal rivers and estuaries. Understanding what factors control sediment-flux partitioning in both tidal rivers and estuaries is important to predict future morphologic changes, particularly considering that estuarine regimes are intruding farther into many of the world's largest and most populated deltas.

In this study, sediment-flux partitioning was measured at a channel bifurcation in the Mekong River Delta that seasonally transitions from a tidal-river to estuarine regime. We make the following conclusions about the impacts of channel depth:

1. Suspended particles in the tidal river were predominately microflocs with effective densities of 0.05-0.3 g cm^{-1} and settling velocities <0.5 mm s^{-1}. Mass settling fluxes were dominated by the finest particles, giving the less frequent formation of larger microflocs and macroflocs minimal influence on potential sediment deposition. Subchannel depth did not have a significant or meaningful direct impact on suspended-sediment particle size or settling velocity.

2. In the deep subchannel, where seaward flows ebb into a larger cross-sectional area, tidal velocity is symmetric, and the residual suspended-sediment flux is near zero.
3. In the shallow subchannel, where seaward flows ebb into a smaller cross-sectional area, flow velocity and shear are ebb dominant. Sediment-induced stratification during ebb flows inhibits the mixing of sediment away from the bed, resulting in a landward flux of suspended sediment. Here, the saturation concentration required for sediment-induced stratification is ~400 mg L^{-1}.
4. Due to these processes, residual sediment flux is directed upstream from the shallow distributary and downstream to the deep distributary when the bifurcation is a tidal river. The flux direction is reversed when fluvial discharge is lesser and estuarine processes control sediment flux.

These results are likely applicable to other tidally influenced deltas that have large supplies of fine-grained sediment, low channel sinuosity, and distributaries of similar lengths. In these deltas, the predicted global increase in seasonal sediment trapping may be disproportionately large in relatively shallow channels.

Chapter 3.

Impacts of Tidal-Channel Connectivity on Transport Asymmetry and Sediment Exchange with Mangrove Forest [1]

3.1 INTRODUCTION

The foundations of coastal ecosystems and communities are built with sediment that is captured by hydrodynamic processes within coastal zones and then deposited. Sediment-transport dynamics in coastal environments such as tidal mudflats (e.g., Boldt et al., 2013; Fagherazzi and Mariotti, 2012; Nowacki and Ogston, 2013; Uncles et al., 2003) and vegetated marshlands (e.g., Bayliss-Smith et al., 1979; Christiansen et al., 2000; Larsen and Harvey, 2010) have been the focus of numerous research projects over the past several decades. Recently, more focus has been directed towards mangrove forests. In tropical and subtropical settings, these forests serve as buffers to coastal erosion and storm damage (e.g., Dahdouh-Guebas et al., 2005; Danielsen et al., 2005; Furukawa et al., 1997; Granek and Ruttenberg, 2007; Thampanya et al., 2006) and are considered important juvenile habitats, refuges, and feeding grounds for many fish species (e.g., Alongi, 2002; Glaser, 2003; Ikejima et al., 2003; Rehage and Loftus, 2007; Robertson and Duke, 1987; Sheridan and Hays, 2003). Mangroves also sustain traditional human communities worldwide, especially in developing regions such as the Brazilian Amazon coast (Fernandes et al., 2018).

Mangroves are estimated to cover >170,000 km^2 globally (Spalding et al., 1997), but they are disappearing at alarming rates; over one-third of the world's mangrove forests have been lost since the 1950s (Duke et al., 2007; Thorne et al., 2011). To predict future change and effectively manage these forests, knowledge of the mechanisms that control sediment transport and morphologic evolution is needed. Previous studies have found that tidal channels deliver sediment to mangrove forests, where sediment is retained due to velocity stagnation, particle flocculation, and settling within the forest (e.g., Furukawa et al., 1997; Horstman et al., 2015). These studies focused on channels with low connectivity, meaning they connect to only one marine body such as an ocean, estuary, or another tidal channel. While some major mangrove forests are incised predominately by low-connectivity channels, such as those studied in Australia (e.g., Larcombe and Ridd, 1996; Wolanski et al., 1992), many of the most expansive mangrove

---

[1] This chapter was submitted to *Estuarine, Coastal and Shelf Research* as: McLachlan, R.L., Ogston, A.S., Asp, N.E., Fricke, A.T., Nittrouer, C.A., and Gomes, V.J.C., Impacts of tidal-channel connectivity on transport asymmetry and sediment exchange with mangrove forests, and was accepted for publication on 2 December, 2019.

forests, such as the Sundarbans (e.g., Hale et al., 2019; Rogers et al., 2014) and those associated with the Fly River (e.g., Walsh and Nittrouer, 2004), are incised by high-connectivity channels with complex morphologies and connections to multiple marine bodies.

Complex channel-bank morphologies and dense vegetation can influence water and sediment flux in estuaries and tidal channels. For example, ephemeral shoals alter sediment-flux pathways and deposition (Ali et al., 2007), and interacting tidal currents complicate flux and produce spatially heterogenous deposition in channels with high connectivity (Warner et al., 2003). Furthermore, secondary circulation of water and sediment is enhanced in mangrove-fringed channels, where hydrodynamics and sediment dynamics differ between the forests and channels (e.g., Adame et al., 2010; Furukawa et al., 1997; Mazda et al., 2005) and interweaving channels create residual flow circulation (Haque et al., 2015). The following questions arise:

1. In what ways do tidal-scale hydrodynamics, specifically water velocity and sediment-transport potential, differ between high- and low-connectivity channels?
2. How do these differences affect sediment delivery from channels to their adjacent mangrove forests?

To answer these questions, suspended sediment was tracked as it transited between estuaries, tidal channels, and mangrove flats within an Amazonian mangrove forest. The interactions between tidal forcing and sediment flux were considered in this study as manifested in (1) tidal-velocity asymmetry and (2) sediment-flux asymmetry.

Within these intertidal environments, bidirectional tidal flows control sediment redistribution between estuaries, tidal channels, and flats. Asymmetry in tidal velocity affects transport in most embayments by causing differences in peak shear stresses during ebb and flood tides (Nidzieko & Ralston, 2012). Asymmetry in phase duration generates asymmetry in velocity when tidal elevation is in quadrature with tidal velocity, meaning that velocity is 90˚ out of phase with tidal elevation (Boon & Byrne, 1981). Confounding factors such as fluvial discharge and complex bathymetry can disrupt this relationship (Dronkers, 1986). Because sediment transport generally scales with water velocity to a high power (e.g., cubed; Bagnold, 1966), contributions to the sediment flux during short durations of maximum water velocity control the net flux by means of tidal pumping (Postma, 1961). In effect, sediment flux scales with asymmetry in both phase duration and velocity under the most simplified circumstances (Figure 3.1).

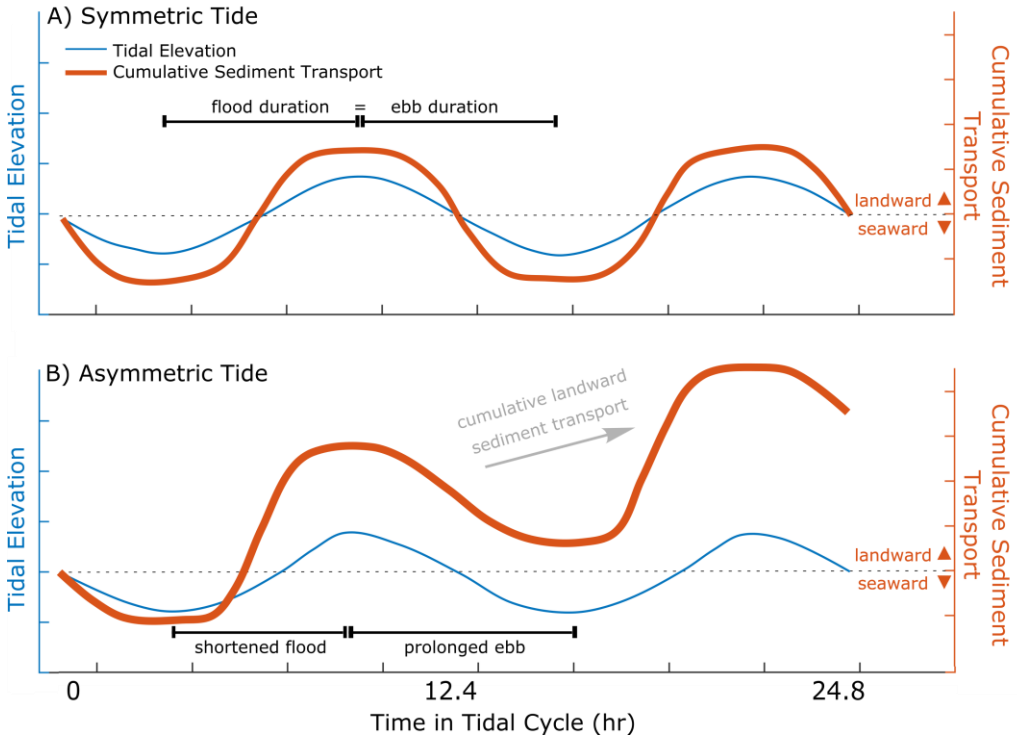

Figure 3.1. A conceptual timeseries demonstrating (A) a symmetric tide that generates no cumulative sediment transport over a tidal cycle and (B) an asymmetric tide that generates a cumulative flux in the direction associated with the shortest tidal-phase duration. In the example scenario presented here, a flood-dominant phase duration produces a landward-dominant sediment flux. Velocity is assumed to be in quadrature with tidal elevation, so sediment transport (S) is scaled as $S \propto (u \propto dh/dt)^3$, where u is along-channel water velocity and dh/dt is the rate of change in tidal elevation.

Asymmetry is further influenced by vegetation. A mangrove forest's dense understory generates turbulence on the forest edge (e.g., Norris et al., 2017) and inhibits sediment-transport potential within the forest relative to the channel (Mazda et al., 1997). As a result, where small channels flood extensive vegetated intertidal regions, falling tide at the channel mouth occurs before that on the flat, shortening the amount of time that water can leave the vegetated flat and truncating ebb tide (Nidzieko & Ralston, 2012). Even if tidal-phase duration is flood dominant in the channel, an ebb-tidal pulse of water entering the channel is created and tidal velocity becomes ebb dominant (e.g., Lincoln and Fitzgerald, 1988; Nidzieko and Ralston, 2012; Speer et al., 1991).

This study compares velocity asymmetry and sediment flux within two channels with differing degrees of connectivity. Conclusions provide foundational concepts to the field of mangrove sediment dynamics by characterizing how morphodynamics, specifically those related to channel connectivity, control sediment flux and accumulation within mangrove forests.

3.2 STUDY REGION

Tidal channels within a mangrove forest on the northern coast of Brazil were studied (Figure 3.2). Channels here display a wide range of connectivity, with many connections between adjacent estuaries. The relatively pristine Amazonian coastline is an ideal study site because the region is largely unaltered by aquaculture, levees, and dredging, and the forests themselves are left predominantly untouched by humans. Approximately 8,000 km^2 of continuous mangrove forests thrive along the tide-dominated coastline to the southeast of the Amazon River mouth (Souza-Filho et al., 2006). The coastline is composed of a series of complex estuary and tidal-channel networks. Sediment exchange between the sandy inner shelf, estuarine basins, and muddy mangrove flats is assumed to exist (Asp et al., 2018), although the exact transport pathways are not yet well defined.

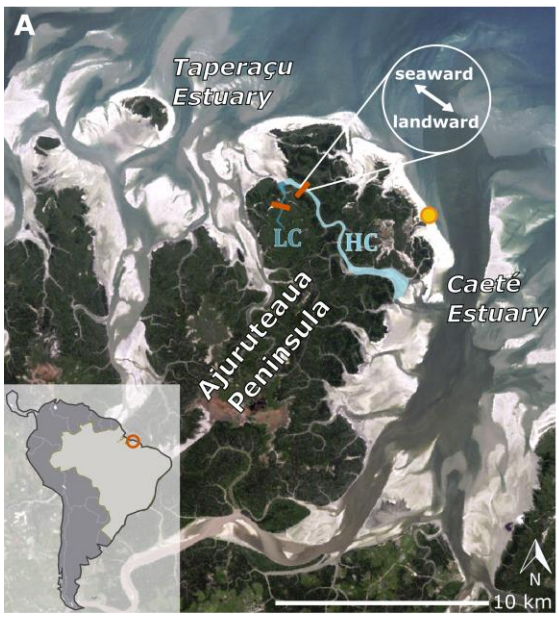

C

	Instrument	Measurement	Sampling Frequency	Sampling Interval	Burst Period
Mangrove Forest	InfinitySD Turbidimeter	turbidity	1 Hz	60 s	60 s
	InfinitySD Electro-magnetic Current Meter	water velocity, pressure	1 Hz	60 s	60 s
Fringe	RBR Duo	turbidity, pressure	6 Hz	continuous	-
Channel Thalweg	Aquadopp Current Profiler, 20 cm bin size	water velocity profile	2 MHz	60 s	30 s
	Campbell Scientific OBS 3+	turbidity, pressure	2 MHz	60 s	30 s

Figure 3.2. A) Map of the Ajuruteua Peninsula on the northern coast of Brazil showing the locations of the studied low-connectivity (LC) and high-connectivity (HC) channels, adjacent estuaries, and study transects (orange lines). Yellow dot indicates position of meteorological station deployed on the outer coast. Satellite image: LandSat TM, 2001, Laboratório de Análise de Imagens do Trópico Úmido. B) Idealized transect cross-section showing the location of fixed instruments (orange squares) deployed in the mangrove forest, fringe, and channel thalweg of each channel. C) Table displaying the location, model, and sampling method of fixed instruments deployed along the study transects.

Two tidal channels with differing degrees of connectivity were explored. They are in close proximity and both traverse the Ajuruteua Peninsula, located ~150 km southeast of the Amazon River mouth (Figure 3.2). This peninsula is flanked by the Caeté estuary to the southeast, which is fed by the

Caeté River, and the Taperaçu estuary to the northwest, which has no direct fluvial input (Asp et al., 2012). The channel with high connectivity, Furo Grande, crosses the entire peninsula and connects both estuaries. The channel with low connectivity opens only into the Taperaçu estuary.

Both channels are flanked by mangroves. The mangrove flats only receive sediment during spring tides; their elevation is ~0.5 m higher than typical neap high-water level and ~0.6 m lower than average spring high-water level (Asp et al., 2016). Tides here are dominated by semidiurnal components, with a spring tidal range of ~5-6 m and a neap tidal range of ~3 m at the coast (Asp et al., 2012, 2013).

The forest is also impacted by seasonally variable processes. Almost three-quarters of the annual precipitation falls between January and April. From September to November, precipitation levels are near zero (Souza-Filho et al., 2009). Local rivers have mean suspended-sediment concentrations of just a few milligrams per liter; the Caeté River only reaches ~20 mg L^{-1} during heavy precipitation events (Asp et al., 2016). The Amazon River is another possible sediment source; the periodic southeastward expansion of the Amazon River plume and resuspension on the inner shelf may deliver sediment to the study region (Geyer et al., 1996; Asp et al., 2018).

Much is known of the coastline's geologic development. Stratigraphic interpretation suggests that coastal evolution over the past 5 kyr has been modulated by small-scale subsidence events associated with three phases of barrier-island development via sandbar emergence (Souza-Filho et al., 2006, 2009). As the rate of sea-level rise decreased in the last 2 kyr, the peninsula underwent the most significant phase of mudflat progradation and lateral accretion, which restricted estuarine flow into the back-barrier channels (Souza-Filho et al., 2006). Research presented here addresses the modern processes associated with sediment transport in the back-barrier system that control the lateral accretion phase of geomorphic development.

3.3 METHODS

3.3.1 *Data Collection*

In-situ hydrodynamic and turbidity measurements were collected (Figure 3.2) during both the dry (4-12 Oct 2015) and wet (4-16 Mar 2016; 24 Mar – 2 Apr 2017) seasons. During each field effort, fixed instruments were deployed for ~10 consecutive days to capture spring and neap tidal endmembers. Timeseries measurements were concentrated on a transect across each channel. To avoid local vorticity in the tidal channels (Fortunato et al., 1997), transects were placed ~2 km from the Taperaçu estuary at relatively straight extents of each channel and away from large drainage channels (Figure 3.2). Each transect may not represent the entire channel, but the patterns observed can be compared because of their similar

distances from channel outlets. To analyze sediment-flux patterns in the thalweg of each channel, we collected water-velocity profiles and measured near-bed turbidity at 0.25 and 0.55 m above the bed (cf. Fricke et al., 2017), to avoid burial and boat snag. Turbidity and water-level data were also collected on the channels' aggrading flanks, which were colonized by salt-marsh grass and juvenile mangroves. Farther into the mangrove forest, ~25 m from the channel, water pressure, turbidity, and velocity were measured.

In addition to the fixed instruments in the channels and forest, a meteorological station (HOBO Onset U30) was deployed on the peninsula's seaward coast (Figure 3.2) to record local wind velocity and precipitation beginning in October 2015. Additionally, boat-mounted cross-channel ADCP (acoustic Doppler current profiler) transects in the high-connectivity channel were performed at accessible portions of the tidal cycle in 2016 to record cross-channel variability and along-channel fluxes of water and suspended sediment.

During both wet seasons, strong tidal currents destabilized instruments deployed in the channel thalwegs and often covered them in organic debris. During the dry season, tidal ranges were inadequate to submerge the upper mangrove flats. As a result, interpretation of channel dynamics is predominately based on data collected during the dry season, and interpretation of mangrove-flat dynamics is solely based on data collected during the wet seasons. In the channel, we expect that wet-season dynamics would enhance results discussed below because input from the Caeté River would increase seaward flux through the high-connectivity channel. In the mangroves, we expect dry-season dynamics to also enhance results discussed below as less sediment would be exported to the channel through runoff associated with precipitation. However, this data set is not sufficient to provide a seasonal comparison.

3.3.2 *Data Processing*

To map sediment-transport pathways and fluxes, suspended-sediment concentration (SSC) was estimated from optical-sensor response. Voltage responses from the profiling and fixed instruments were converted to SSC by calibration with concurrently collected water samples assuming a linear response ($n_{\text{profiling}} = 63$, $n_{\text{fixed}} = 20$, $r^2 > 0.8$).

Along-channel fluxes were estimated by integrating measured SSC and water velocity through space and time. Sediment flux (F_S) over the channel thalweg within the lower 0.5 m of the water column was calculated as

$$F_s = \int_0^T \int_0^{0.5} u\, SSC\, dh\, dt, \tag{3.6}$$

where u is along-channel water velocity, h is elevation above channel bed, and T is total time in a tidal cycle. Sediment fluxes calculated in regions with direct turbidity measurements, i.e. the lower water column

above the thalwegs, were then scaled up to the entire channel cross section using geometry based on measured channel bathymetry;

$$F_{s(cross\ section)} = \int_0^T \bar{u}\ SSC\ A\ dt, \tag{3.7}$$

where $\bar{u}$ is the depth-averaged velocity over the thalwegs and *A* is the cross-sectional area of the channel at time *t*. On the mangrove flats, water velocity was recorded at a single point, rather than profiled through the water column as in the channel; therefore, sediment flux into the forests was calculated as

$$F_s = \int_0^T u\ SSC\ H\ dt, \tag{3.8}$$

where *H* is water depth. Sediment-transport pathways were visualized by effectively converting from eulerian to lagrangian reference frames;

$$X_{t=n} = X_{t=n-1} + u_{t=n}\ SSC\ \Delta t, \tag{3.9}$$

where *X* represents the progression of a parcel along a net flux pathway and *n* is the sample number.

To examine how the incident asymmetry in phase duration translated to velocity skew and net sediment flux, tidal asymmetry (γ) was calculated as the normalized sample skewness:

$$\gamma \equiv \frac{\mu_3}{\sigma^3} = \left[\frac{1}{N-1}\sum_{n=1}^{N}(\mathrm{V'}_t - \bar{\mathrm{V}}')^3\right] \Big/ \left[\frac{1}{N-1}\sum_{n=1}^{N}(\mathrm{V'}_t - \bar{\mathrm{V}}')^2\right]^{3/2}, \tag{3.10}$$

where μ_3 is the third sample moment about the mean, σ is the standard deviation, N is the total number of observations from time $t = 1$ to $t = T$, and V is the relevant variable (cf. Nidzieko, 2010; Nidzieko and Ralston, 2012; Thomson and Emery, 2014). Phase-duration asymmetry (γ_d) quantifies the difference in duration of rising and falling tide ($V = \partial h/\partial t = h'$, where h is tidal elevation); velocity asymmetry (γ_u) quantifies the skewness in the distribution of ebb and flood tidal currents over a tidal cycle ($V = u$, where u is depth-averaged water velocity); and sediment-flux asymmetry (γ_s) quantifies the skewness in distribution of ebb and flood sediment flux at a single point over a tidal cycle ($V = u\ SSC$).

3.4 RESULTS

3.4.1 *Tidal Channels*

Flux patterns over the channel thalwegs differed between the two channels during the dry season. Flux calculations, as described in the methods, reveal that sediment transported through the low-connectivity channel is tidally modulated, with a relatively short landward translation averaged over many tidal cycles (F_s = ~63 kg per meter of channel width per tidal cycle), whereas sediment transported through the high-connectivity channel shows a more consistent seaward transport, regardless of tidal phase or range (F_s = ~1300 kg per meter of channel width per tidal cycle). Positive fluxes represent seaward flow, defined as transport towards the northern Taperaçu estuary for both channels studied (Figure 3.2A). These fluxes were integrated over the channel cross section to estimate sediment budgets. Per tidal cycle, the low-connectivity channel imports ~31 t of suspended sediment landward. In contrast, per tidal cycle, the high-connectivity channel exports ~1140 t from the Caeté estuary towards the Taperaçu estuary.

Within the low-connectivity channel, water flowed landward with rising tide and seaward with falling tide, resulting in two periods of slack water over a 12.4-h tidal cycle (Figure 3.3A). However, currents in the high-connectivity channel reversed directions four times within a semidiurnal tidal cycle, resulting in four periods of slack water at the transect (Figure 3.3B). This pattern creates an inequality between the descriptors “flooding”, “rising”, and “landward” as well as “ebbing”, “falling”, and “seaward” to describe flow direction. To clarify terminology used hereon in this manuscript, rising/falling will refer to changes in water level, whereas landward/seaward will refer to along-channel flux directions. The terms flood and ebb will only be used regarding flow within the mangrove forests: rising tide floods into the forest and falling tide ebbs into the channel.

Timing and magnitude of sediment flux were not in phase with those of water flux. For example, maximum water velocity occurred during seaward flows in both channels, but the timing of maximum SSC varied. In the low-connectivity channel, SSC reached ~0.4 g L^{-1} as water flowed landward but was typically <0.2 g L^{-1} during maximum seaward velocity (Figure 3.3C,E). This pattern contrasts with that observed in the high-connectivity channel, where SSC was minimal during landward flows (<0.2 g L^{-1}) and greatest during seaward flows (>0.3 g L^{-1}) (Figure 3.3D,F).

Dynamics also varied over fortnightly timescales. In both channels, tides became more asymmetric as tidal ranges increased and water overtopped the channel banks; larger tidal ranges are associated with both shorter rising-tide duration as well as seaward-dominant velocities and sediment fluxes (Figure 3.4G-J). Depth-averaged landward velocities rarely reached 0.5 m s^{-1} in the low-connectivity channel or 0.8 m s^{-1} in the high-connectivity channel, whereas seaward velocities exceeded 0.9 and 1.1 m s^{-1}, respectively

(Figure 3.4D). Although the fortnightly patterns of asymmetry were similar between the two channels (Figure 3.4I,J), net sediment fluxes were landward in the low-connectivity channel (Figure 3.4G) and seaward in the high-connectivity channel (Figure 3.4H).

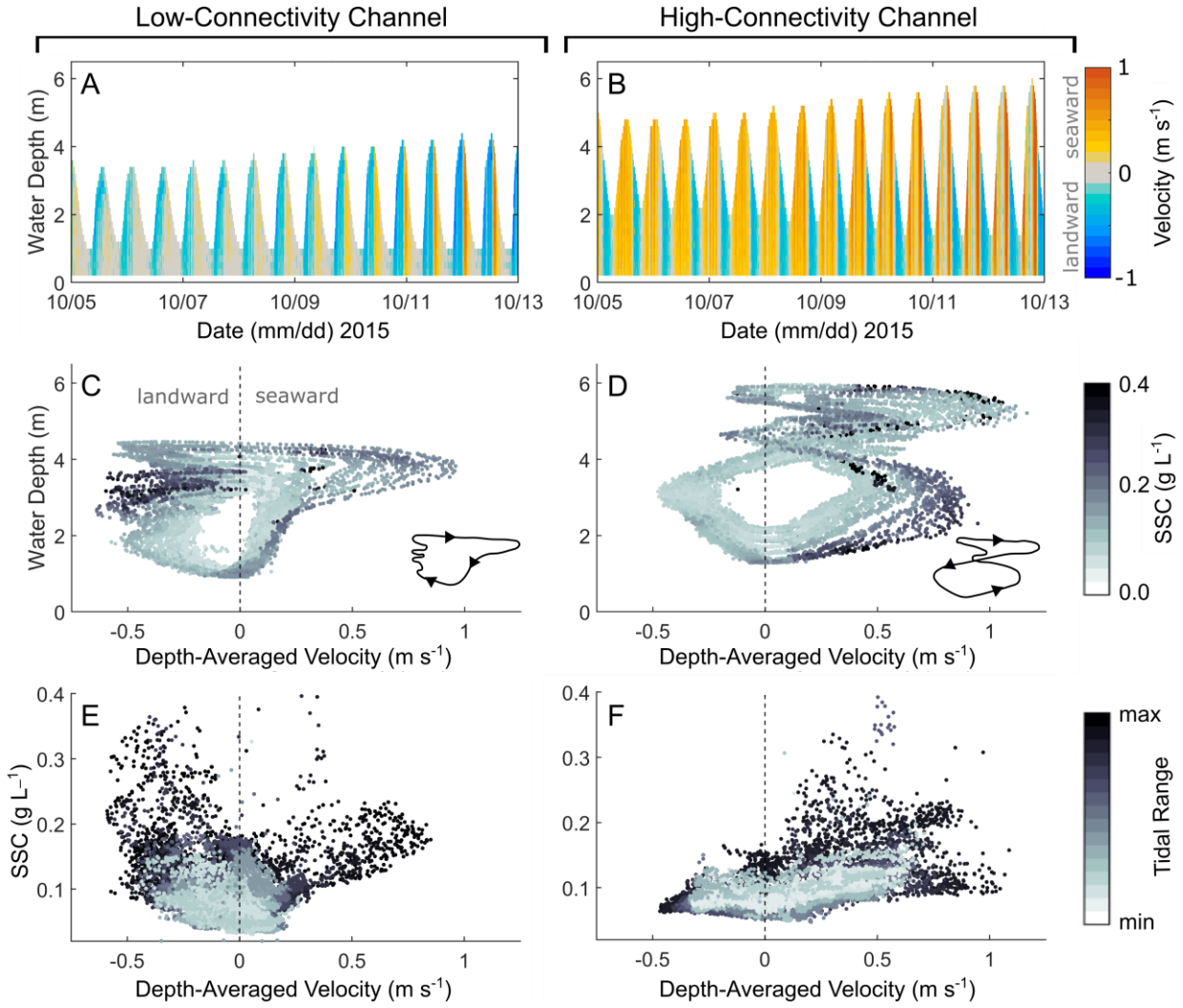

Figure 3.3. Data collected in the 2015 dry season illustrating the relationships between water depth, velocity, and SSC over the channel thalwegs. A,B) Timeseries of water depth and velocity in each channel. C,D) Velocity-stage diagrams shaded by SSC. Inset diagrams illustrate shape and directionality of velocity-stage diagram over a single spring tide. E,F) Scatterplot of depth-averaged water velocity and SSC shaded by relative tidal range. Only data collected during a fully captured tidal period are plotted. Suspended-sediment concentrations were measured 0.25 m above channel beds.

To assess homogeneity of velocity and SSC over the transect cross sections, cross-channel water-velocity profiles (Figure 3.5A,B) and vertical turbidity profiles were measured (Figure 3.5C). The water-column properties were found to be well-mixed, at least during accessible portions of the tidal cycles when

these measurements were obtained. Moreover, turbidity measurements from the channel fringes were equivalent in magnitude to those measured in the channel thalwegs during rising tide (Figure 3.5D), demonstrating that the channel waters are horizontally homogenous when water from the channel flows into the forest during rising tide.

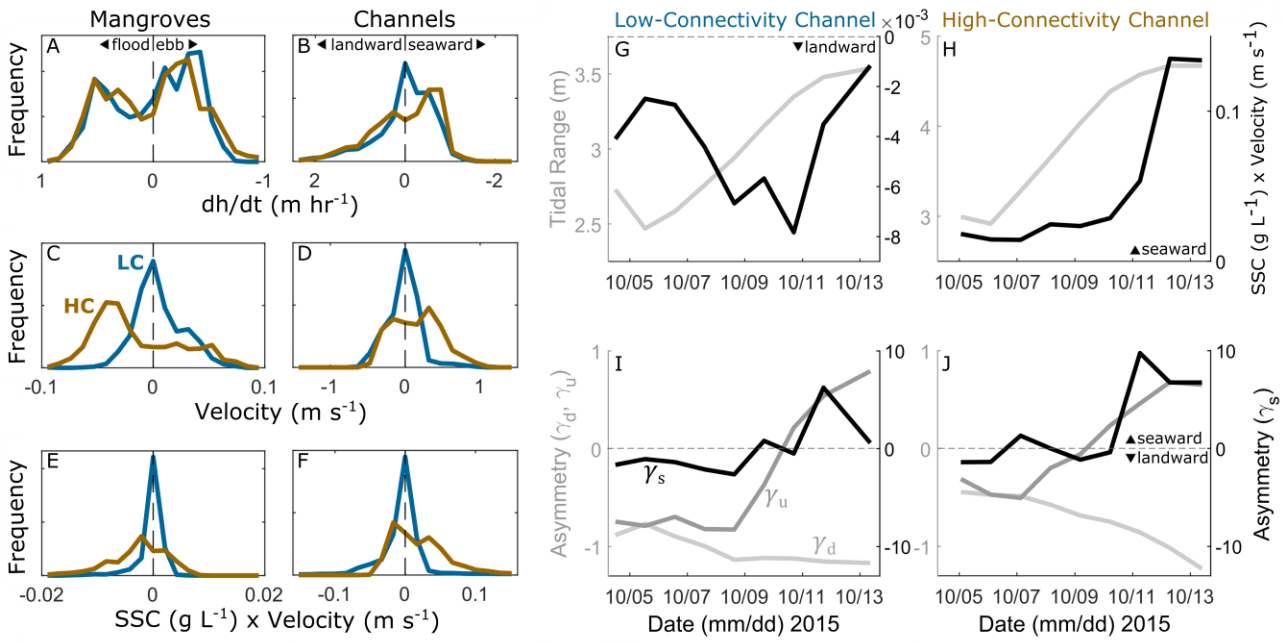

Figure 3.4. A-F) Frequency distributions for water-elevation change over time (*dh/dt*), water velocity, and rate of sediment transport measured in the low-connectivity (LC) and high-connectivity (HC) channels and mangrove forests. Velocities in the channels are depth averaged. G-J) Timeseries showing trends in tidal range, net sediment flux, and asymmetry of tidal duration, velocity, and sediment-transport rate in each channel. All variables in timeseries are averaged over 12.4-h windows.

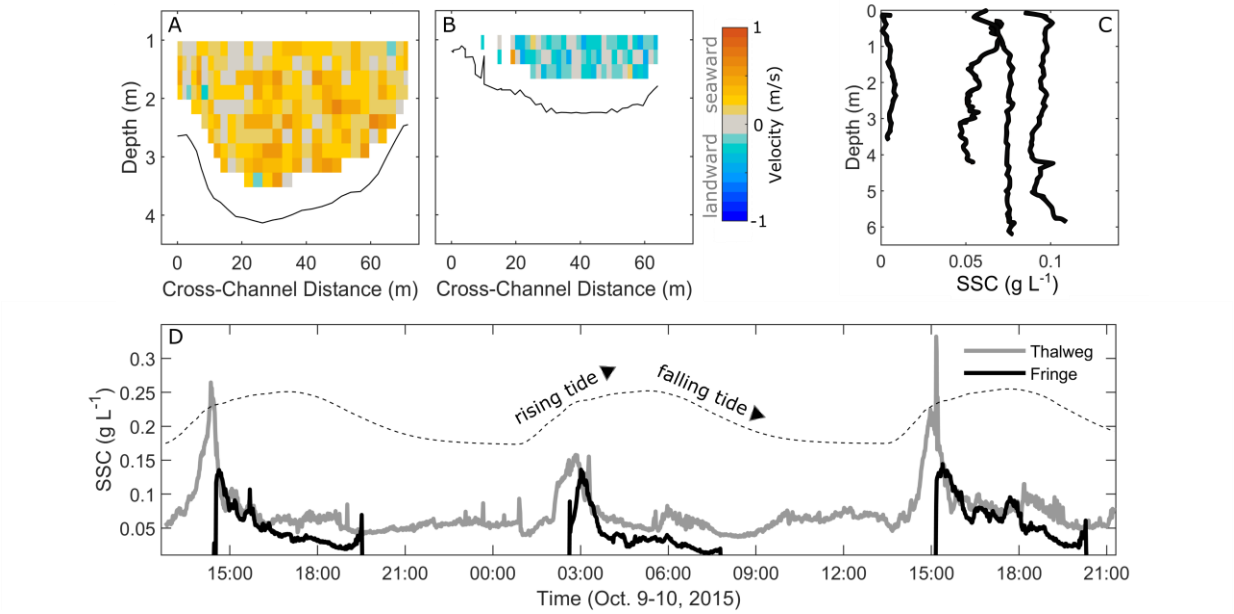

Figure 3.5. A,B) Characteristic cross sections of along-channel water velocity during landward and seaward flows in the high-connectivity channel illustrating cross-channel homogeneity. Black line denotes channel bed. Measurements collected with an ADCP in 2016. C) A selection of SSC profiles collected from both channels at various tidal phases demonstrating that the channels are vertically well mixed. Measurements collected with a CTD+OBS in 2017. D) Suspended-sediment concentration measured concurrently in the low-connectivity channel thalweg and fringe. Concentration measured in the thalweg is equivalent to that on the fringe immediately after fringe instruments are submerged during rising tide. Dotted line represents water depth and illustrates periods of rising and falling tide. Measurements collected in 2015.

3.4.2 *Mangrove Flats*

Flux patterns in the mangrove forests were similar between the two channel systems during the wet seasons, though calculations of sediment flux, as described in the methods, reveal that the mangroves surrounding the high-connectivity channel imported a larger amount of sediment. Per tidal cycle, the low-connectivity channel imported 1.2 kg of sediment into the mangroves per meter of channel length, whereas the high-connectivity channel imported 37 kg of sediment into the mangroves per meter of channel length. Horizontal velocities were correlated with the rate of change of tidal elevation, and maximum flood and ebb water velocities over the flats were similar in each channel. Maximum velocities reached 0.07 m s^{-1} on the flats surrounding the low-connectivity channel (Figure 3.6A, C) and 0.09 m s^{-1} on those surrounding the high-connectivity channel (Figure 3.6B,D).

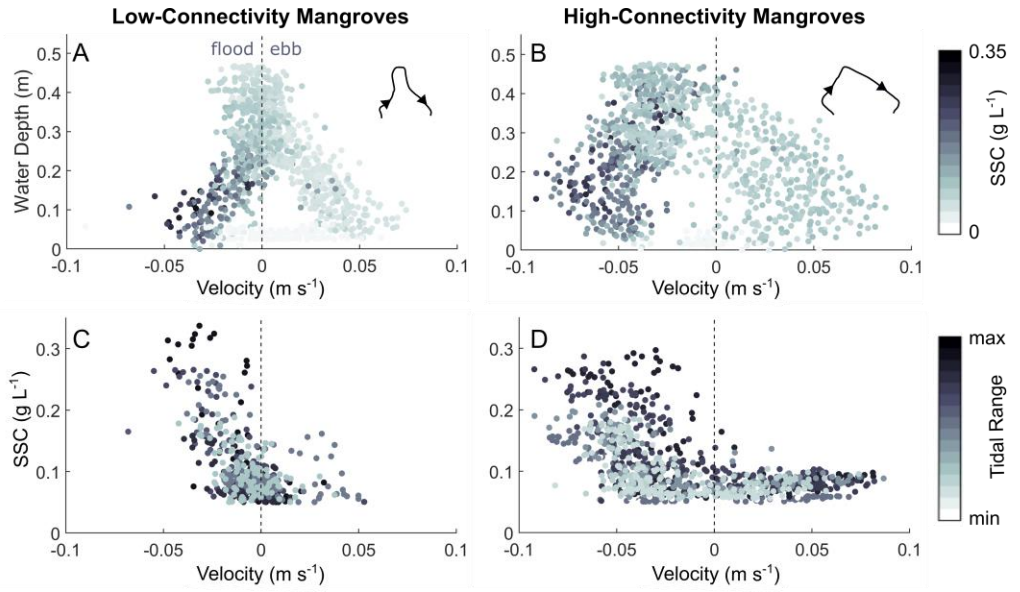

Figure 3.6. Data collected in the 2017 wet season illustrating the relationships between water depth, velocity, and SSC within the mangrove forests. A,B) Velocity-stage diagrams colored by SSC. Inset diagrams illustrate shape and directionality of velocity-stage diagram over a single spring tide. C,D) Scatterplot of water velocity and SSC colored by relative tidal range. Only data collected during a fully captured tidal period are plotted. Velocity and turbidity measured ~0.15 m above forest floor.

3.5 DISCUSSION

Because the channels were found to be well mixed both vertically and horizontally during the dry season (Figure 3.5A-C), measurements recorded with fixed instruments in the channel thalwegs can be considered characteristic of the entire channel cross section. Vertical mixing is strong in mangrove-fringed tidal channels because sinuous morphology induces secondary transverse-circulation cells (Wolanski et al., 1992), particularly where muddy beds create strong bottom friction (Wolanski et al., 1980). Additionally, the relatively large tidal amplitude compared to channel depth (Wolanski et al., 1992) and the minimal along-channel density gradient both promote vertical mixing (Bowden, 1981). This homogeneity of channel waters suggests that representative water properties, such as turbidity measured in a channel, are transported into the mangrove forests. We observed turbidity measurements from the channel fringes that were equivalent to those measured in the channel thalwegs during rising tide but less than those during falling tide (Figure 3.5D), suggesting that sediment is transported into the forest during rising tide, and some of that sediment is deposited.

The relative importance of mechanisms that control sediment flux, including resuspension, settling, and deposition, apparently do differ between these two channel systems, as described in more detail in the following sections. Whereas flux patterns in the mangroves were similar for both channel systems, those

patterns within the channels differed. These differences influence the amount of sediment available to the mangrove forests and can be explained by the effects of channel connectivity on tidal asymmetries.

3.5.1 *Asymmetry: Sources and Impacts*

3.5.1.1 Phase-Duration Asymmetry

As a tidal wave propagates into shallower water, the growth and interactions of harmonic frequencies distort its initially sinusoidal shape. Estuaries that are shallow compared to tidal amplitude and/or those that have a much larger intertidal storage volume on the flats than in the channel tend to be flood dominant in tidal duration (Friedrichs & Aubrey, 1988). This is the case for both channels studied here during the dry season. The phase-duration asymmetry is negative (Figure 3.4I,J), i.e. rising-tide duration is shorter, and is correlated with tidal range (Figure 3.4G-J), which supports the importance of large tidal amplitude and intertidal storage volume.

3.5.1.2 Tidal-Velocity Asymmetry

In the absence of confounding factors such as complex bathymetry and fluvial discharge, phase-duration asymmetry generates tidal-velocity asymmetry. These conditions are met in the low-connectivity channel when tidal ranges are <3 m and insufficient to inundate the mangrove forest (Figure 3.4G,I); shorter rising tides generate faster landward velocities because velocity is most strongly dependent on the along-channel pressure gradient.

When tidal ranges become sufficient to inundate the mangrove flats (>3 m), ebb-tidal pulses shift velocity asymmetry within the low-connectivity channel to become seaward dominant (Figure 3.4G,I). During the largest tidal ranges, peak seaward velocities are ~50% faster than peak landward velocities (Figure 3.3E). This ratio of seaward to landward peak velocity is on the higher end of the observed range in other mangrove-channel systems (e.g., Wolanski et al., 1980; Woodroffe, 1985), and much greater than (e.g., Nowacki and Ogston, 2013) or even opposite of (e.g., Aubrey, 1986; Friedrichs et al., 1990) those in estuaries without mangroves. The large ratio here could be due to a large friction factor caused by mangrove density (Wolanski et al., 1980; Mazda et al., 1995) and/or a large ratio of mangrove-flat area to channel area (Wolanski et al., 1992).

The shape of the velocity-stage diagram for the low-connectivity channel (Figure 3.3C) resembles those of other similar well studied channels (e.g., Larcombe and Ridd, 1996). When water is confined within the channel, velocity is relatively slow, reducing shear stress and sediment-transport capacity. When water inundates the mangrove forest, an ebb-tide pulse develops, increasing shear stress and sediment-transport

capacity. In effect, the largest tidal ranges create the fastest ebb-tidal pulses (Figure 3.3C.E) and the most seaward-dominant velocity asymmetries (Figure 3.4G,I).

In contrast to the low-connectivity channel, the residual water flux from the Caeté estuary towards the Taperaçu estuary positively shifts velocity asymmetry in the high-connectivity channel to be more seaward dominant (Figure 3.4J). Tidal elevation and water velocity are not in quadrature as they are in the low-connectivity channel (Figure 3.3D), so common patterns of hydrodynamics and sediment transport previously discussed do not apply.

The shape of the velocity-stage diagram for the high-connectivity channel (Figure 3.3D) differs substantially from that of the low-connectivity channel (Figure 3.3C). In the high-connectivity channel, water-velocity direction is not forced by a single standing tidal wave. Instead, there is a difference in tidal phase and/or amplitude between the two channel outlets, likely a result of the northwestward propagation of the principal lunar semi-diurnal tide offshore (Lyard et al., 2006). This imbalance creates an along-channel pressure gradient that skews the velocity asymmetry (Figure 3.4F).

Additionally, water velocity is strongly influenced by the bathymetry of the estuaries. Sandy shoal deposits in both estuaries become subaerial at low tide, creating barriers at each outlet and blocking flow. The initiation of flow during rising tide occurs when tidal elevation supersedes the shoals. This occurs first on the southwestern Caeté side, steepening the along-channel pressure gradient and quickening seaward velocity (Figure 3.3B,D). Because of these processes in the high-connectivity channel, water flows seaward during the onset of rising tide and during the ebb tidal pulse, further pushing tidal-velocity asymmetry seaward (Figure 3.4J).

3.5.1.3 Sediment-Flux Asymmetry

Cumulative sediment flux was seaward in the high-connectivity channel and landward in the low-connectivity channel during the dry season (Figure 3.7), demonstrating the influence of channel connectivity. Sediment flux depends on both sediment-transport capacity, i.e. shear stress, and sediment availability. Therefore, if sufficient sediment is available to be resuspended, velocity asymmetry will generate sediment-flux asymmetry. In the low-connectivity channel, SSC and velocity show a strong positive correlation (Figure 3.3E), so sediment-flux asymmetry tends to be directed in the same direction as tidal-velocity asymmetry (Figure 3.4I).

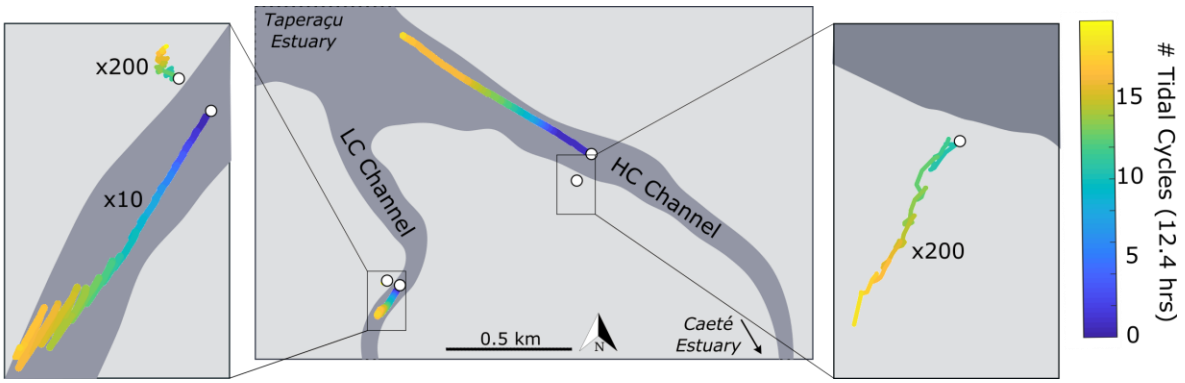

Figure 3.7. Sediment path lines along the low-connectivity (LC) and high-connectivity (HC) channels (2015) and in the forests (2017) calculated as $X_{t=n} = X_{t=n-1} + u_{t=n}\ SSC\ \Delta t$, where X is the progression of the tracked parcel along a net flux pathway. White circles represent locations of fixed instruments. Scaling of path lines is arbitrary, but all path lines are shown at the same scale in the center panel. Side panels illustrate path lines magnified relative to the center panel.

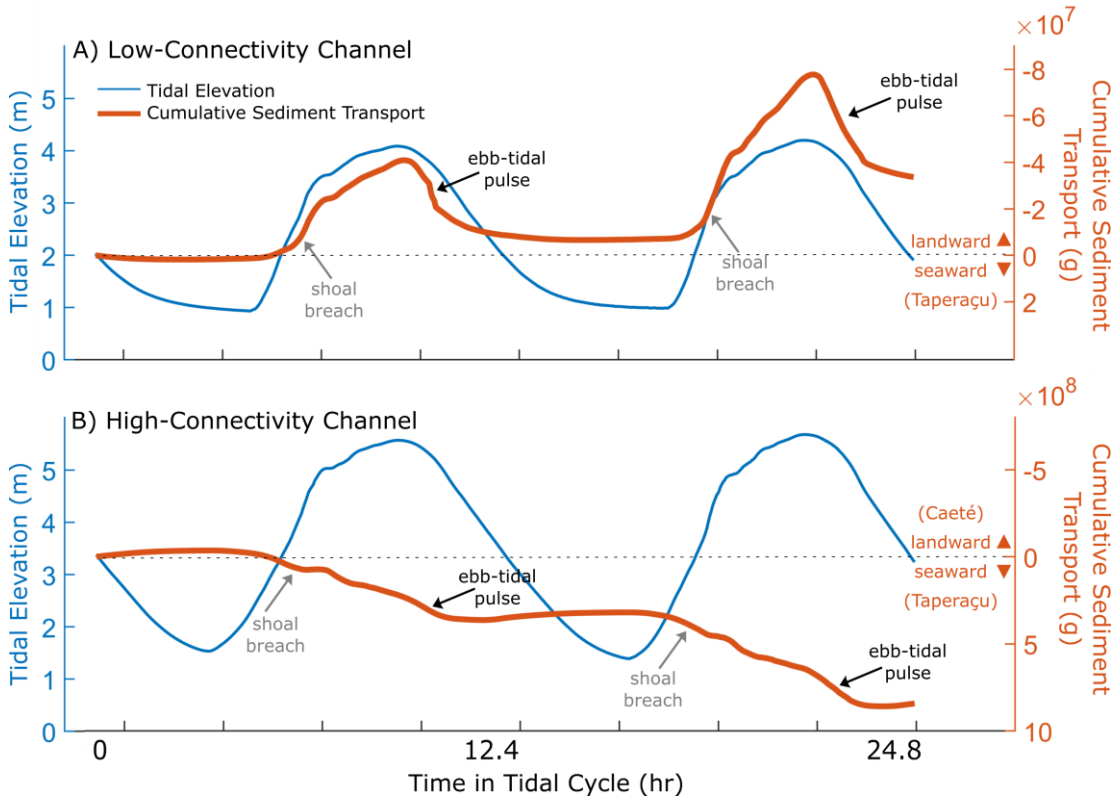

Figure 3.8. Timeseries demonstrating tidal elevation and cumulative sediment transport over two complete tidal cycles (24.8 hours) in the (A) low-connectivity channel and (B) high-connectivity channel. Cumulative sediment transport was calculated as the cumulative flux of sediment to pass over each channel transect, as described in the methods section. The timing of ebb-tidal pulses and shoal breaches have been identified. Note that the scale of sediment transport is an order of magnitude greater in the high-connectivity channel than that in the low-connectivity channel.

Comparing cumulative sediment transport through time in the low-connectivity channel (Figure 3.8A) to that in an ideal flood-dominant, non-vegetated tidal channel (Figure 3.1B) demonstrates that the development of an ebb-tidal pulse can reduce cumulative sediment flux but does not necessarily reverse the residual along-channel flux direction. This pattern of suspended-sediment import during all tidal ranges is not unique. Persistent import of suspended sediment has been recorded in other low-connectivity tidal channels that incise mangrove forests, including those in Australia (e.g., Furukawa et al., 1997; Larcombe and Ridd, 1996), India (e.g., Kathiresan, 2003), and Thailand (e.g., Horstman et al., 2015).

Differences in sediment-transport potential between channels and mangroves also impact sediment flux. When velocities increase to >0.2 m s^{-1}, SSC also increases, suggesting that resuspension plays a dominant role in transport within the channels (Figure 3.3E). However, this relationship is not consistent between tidal phases. SSC values are larger during rising tides than falling tides with equivalent velocities (Figure 3.3E), further implicating the channel-mangrove interaction as a control of residual sediment flux.

Although velocities are fastest during the ebb-tidal pulse (Figure 3.3C), resuspension from the channel bed appears to be minimal; less sediment is suspended compared to rising tide (Figure 3.3E). This explanation agrees with a fundamental theory of mangrove-channel dynamics proposed by Wolanski et al. (1992); ebb-tidal pulses scour channel beds, limiting the sediment available for resuspension, and maintain an equilibrium ratio between the volume of the inundated mangrove flat and depth of the channel. If geometry of the mangrove/creek system is stable, bed sediment below the equilibrium channel depth will not be resuspended during ebb-tidal pulses and will consolidate over time. Additionally, if sediment accumulates on the mangrove flats, as is suggested here, the channel will shallow in response, further diminishing sediment export.

Whereas net sediment flux in the low-connectivity channel is largely determined by phase-duration and tidal-velocity asymmetry, flux in the high-connectivity channel is more influenced by tidal-velocity magnitude and sediment availability. The fastest water velocities in the high-connectivity channel, associated with the onset of rising tide and the ebb tidal pulse, occur during portions of the tidal cycle when water flows seaward. Therefore, the strongest shear stresses are directed seaward (Figure 3.3D), and sediment transport is overwhelmingly seaward (Figure 3.4H and Figure 3.8B).

Conclusions discussed here can be applied to other high-connectivity channels, although the net sediment-flux direction may not necessarily be the same and/or may vary seasonally. These channels effectively distribute sediment along a coastline. In this study region, the high-connectivity channel transports sediment towards the Taperaçu estuary, an estuary with no direct fluvial input that serves as the source of sediment to the low-connectivity channel and numerous others (Figure 3.7).

3.5.2 *Transport into the Mangrove Forests*

Though tidally modulated, sediment was persistently imported into the forests for both channel systems during the wet seasons (Figure 3.7). The transport rate depends on velocity and SSC. Channel connectivity has been shown here to impact SSC in the channels, but not mechanisms that control channel-mangrove sediment exchange such as cross-channel pressure gradients.

Flux into and out of mangroves is controlled by the pressure gradient between the channel and forest, which is in part determined by the rate of tidal-elevation change in the channel and the frictionally generated phase lag produced by dense vegetation, neither of which are directly controlled by channel connectivity. As a result, hydrodynamics within the mangroves that surround channels with varying degrees of connectivity should be similar, assuming vegetation density and topography are comparable. Indeed, relationships between water velocity, turbidity, and tidal range within the mangrove forests are comparable for both systems studied (Figure 3.6). The larger fluxes of sediment into the mangroves bordering the high-connectivity channel are likely a result of this channel servicing a larger mangrove area, which provides a larger intertidal volume and tidal prism (e.g., Wattayakorn et al., 1990; Woodroffe, 1985).

When the mangrove forests are inundated, the shape of the tidal-elevation profiles through time (Figure 3.3A,B) and the velocity-stage diagrams (Figure 3.6A,B) are comparable between the two studied channels; slight dissimilarities can be explained by differences in local topography and vegetation density that alter flux direction and speed. In the high-connectivity channel, interacting tidal waves do not appear to meaningfully affect the rate of water-elevation change. This may not apply to systems with larger phase lags.

More sediment is in suspension as water flows into the forests during rising tide than is still in suspension as the water flows back into the channel during falling tide, regardless of tidal range or water velocity (Figure 3.6C,D), resulting in net sediment import (Figure 3.7). The fastest velocities within the mangrove forests do not exceed 0.1 m s^{-1} (Figure 3.6), much slower than the observed minimum velocity required to resuspend bed sediment in the channels (~0.2 m s^{-1}) (Figure 3.3E,F). These slow velocities are comparable to observations in other similar mangrove forests (e.g., Aucan and Ridd, 2000; Wolanski et al., 1992, 1980). As a result of these diminished velocities and consequent weak shear stresses, water exported back into the channel typically had SSC <0.1 g L^{-1} (Figure 3.6C,D). This suggests that the sediment left in suspension is the finest and slowest settling material; all faster-settling material deposits.

Channel connectivity was found to only indirectly affect sediment transport into forests by influencing the provenance and volume of available sediment. In high-connectivity channels, the imposition of a net flux creates faster velocities in the direction of that flux and slower velocities in the opposing direction. These faster tidal velocities can resuspend more sediment that may enter the adjacent mangrove

forests compared to their low-connectivity counterparts, if these faster velocities immediately precede mangrove inundation.

3.5.3 *Implications for Coastal Development*

This study found that within channel networks that distribute sediment along a coastline, channels with low connectivity serve a different purpose than those with high connectivity, and, as a result, back-barrier infilling and channel closure can dramatically affect the along-shore distribution and sediment supply to tidal channels and mangrove forests. The estuaries and channels discussed here are assumed to receive sediment from local rivers as well as sediment imported from offshore. While both estuaries likely import sediment from the continental shelf, only the Caeté estuary receives direct fluvial input. Observations suggest that sediment trapped within the Caeté estuary turbidity maximum (Asp et al., 2018) is flushed through the high-connectivity channel to the Taperaçu estuary. The amount of sediment imported by the low-connectivity channel (~31 tons per tidal cycle) is <3% of what the high-connectivity channel delivers to the Taperaçu estuary (~1140 tons per tidal cycle), making the amount of sediment imported directly from offshore inconsequential on tidal timescales. Because high-connectivity channels bisect many of the estuaries along this 480-km coastline (Souza-Filho et al., 2009), sediment is assumed to migrate along the entire coastline through these channels, supplying estuaries and channels that do not have as large of a direct fluvial source.

This conclusion adds onto the hypothesis of sandy bar emergence and subsequent back-barrier infilling that has constructed this coastline (Souza-Filho et al., 2006). A bar that does not completely weld onto the mainland will create a back-barrier channel with high connectivity, and sediment will be distributed along the coastline beyond just proximate mangrove forests. The back-barrier environment may then infill until the bar connects to the mainland, creating low-connectivity back-barrier channels. Sediment distribution along the coastline will be diminished and the mangrove forests surrounding the channels will depend on immediately adjacent sediment sources.

3.6 CONCLUSIONS

The morphodynamics of mangrove forests, including the impact of channel connectivity on sediment transport, must be understood to effectively protect and manage these highly productive environments in the face of sea-level rise and changes to sediment supply. Hydrodynamics and sediment dynamics were observed and analyzed for two tide-dominated channels within a Brazilian mangrove forest, allowing for the impact of channel connectivity on sediment distribution to be evaluated.

Dynamics within high-connectivity and low-connectivity channels differ. Within low-connectivity channels, tidal duration and tidal velocity are in quadrature and are both landward dominant when tidal ranges remain below the elevation of the mangrove flats. When water overtops the flats, ebb-tidal pulses develop and skew the tidal-velocity asymmetry temporarily seaward. Still, sediment is consistently imported inland.

In contrast, tidal duration and tidal velocity are not in quadrature within high connectivity channels, and a residual flow skews water and sediment fluxes. The greatest sediment flux occurs during strong ebb-tidal pulses. The direction of along-channel flow concurrent with the ebb-tidal pulse determines the net direction of sediment flux. These channels act as conduits for water and sediment along the coastline and provide sediment to estuaries and channels that may not have their own direct fluvial source. Additionally, channel connectivity influences both the source and volume of sediment available to the surrounding mangrove forest but does not affect the processes that distribute sediment once it leaves the channels and enters the mangrove forests.

This study of *in-situ* morphodynamics has shed light on how sediment transits through tidal channels and along mangrove-vegetated coastlines. Future studies will benefit from combining modern observations of processes acting on sediment in suspension, such as those presented here, with signatures preserved in the sedimentary record that can help elucidate how that sediment is ultimately preserved.

Chapter 4.

Morphologic Evolution of a Macrotidal Back-Barrier Environment: The Amazon Coast [1]

4.1 INTRODUCTION

The emergence of an offshore bar can create a barrier island and back-barrier lagoon. Sediment can then infill the lagoon, creating distinct tidal-channel networks and ultimately welding the barrier onto the mainland. The theory of barrier formation via sandy bar emergence was first proposed by de Beaumont (1845), but the step-by-step processes that drive subsequent infilling landward of the barrier are still not completely understood. It is critical to develop a conceptual understanding of how coastal-system morphology responds to dynamic processes that are increasingly threatening coastal-zone stability worldwide, such as sea-level rise (e.g., Nicholls et al., 1999; Schuerch et al., 2018; Vafeidis et al., 2008), increasing storm intensity (e.g., Mousavi et al., 2011; Sobel et al., 2016; Walsh et al., 2016), land-use change (e.g., Walling, 2006; Hayashi et al., 2019; Liu et al., 2020), and sediment starvation (e.g., Milliman and Farnsworth, 2011; Syvitski and Kettner, 2011). Thus, comprehension of morphologic evolution in back-barrier lagoons and tidal channels is important for future efforts in coastal management and restoration.

Offshore bars are usually elongate features oriented parallel with the shoreline. These bars are often formed from offshore sand that is resuspended by waves, transported landward by asymmetric wave action, and then deposited as oncoming wave energy dissipates in shallow water (de Beaumont, 1845; Johnson, 1919; King and Williams, 1949). Extensive geologic investigations have shown that this type of bar emergence commonly creates long-lived islets and associated back-barrier environments along many gently sloping sandy coastlines worldwide, including the northern Gulf of Mexico (Otvos, 1981), the US Mid-Atlantic Bight (Oertel and Overman, 2004), and northern Brazil (Souza-Filho et al., 2006). After the bars form, wave energy can continue to move them farther inland, welding them onto the beach as the mobile sand spreads laterally along the shoreline (Oertel and Overman, 2004).

Another way these bars can join with the mainland is through sediment deposition and infilling in the back-barrier environment. Sediment infilling behind barriers has been studied in lagoon settings with

---

[1] This chapter was submitted to *Sedimentology* as: McLachlan, R.L., Ogston, A.S., Asp, N.E., Fricke, A.T., Nittrouer, C.A., and Schettini, C.A.F., Morphologic evolution of a macrotidal back-barrier environment: the Amazon coast, and was accepted for publication on 24 April, 2020.

one (e.g., Sloss et al., 2005, 2007, 2011; Benallack et al., 2016) or more marine outlets (e.g., Thorbjarnarson et al., 1985; Zeff, 1988). These studies reveal the importance of the barriers to provide sheltered, low-energy environments for sediment deposition and retention. For example, open lagoons behind protective barriers can progressively lose accommodation space as flood-tide shoals deposit, grow laterally and vertically, and restrict flow through the system, creating stable tidal channels within back-barrier environments (Zeff, 1988). Circulation of marine water through the back-barrier environment can also be restricted by sea-level regression (Sloss et al., 2005, 2007; Souza-Filho et al., 2009) and/or increased rates of sediment supply (Sloss et al., 2005). Sediment in confined lagoons is generally dominated by mud (Roy et al., 1980; Thorbjarnarson et al., 1985; Dalrymple and Choi, 2007) because quiescent lagoons can trap fine sediment delivered by rivers and that from offshore transported landward in bottom flows (Postma, 1967; Burchard et al., 2018). Back-barrier environments can continue to infill as sediment supply and accommodation space allow, while the barrier remains stable (Benallack et al., 2016).

The presence of stabilizing vegetation, such as marsh grass and mangrove trees, is another factor known to influence sediment dynamics in these intertidal environments. The dense understories of mangrove forests are hydraulically rough (Wolanski et al., 1980; Mazda et al., 1995; Furukawa et al., 1997), slowing water speed while enhancing vegetation-scale turbulence (Furukawa et al., 1997; Norris et al., 2017). In effect, some of the sediment that flows into a mangrove forest remains in suspension during flood tide, settles to the bed during high slack water, and is not resuspended during the following ebb tide (e.g., Adame et al., 2010; Furukawa et al., 1997; McLachlan et al., 2020), promoting tidal-flat aggradation.

As coastal zones accumulate sediment, they can preserve signals of morphologic evolution over a wide range of temporal and spatial scales, from minutes to millennia and from millimeters to kilometers. Therefore, to understand the step-by-step progression of geomorphic change and feedback interactions between morphology and hydrodynamics, signals should be interpreted with a variety of analytical tools that are each targeted toward a specific temporal and spatial scale. *In-situ* dynamics, including water velocity and turbidity, control sediment flux and deposition on tidal timescales. Over longer timescales, from tidal cycles to seasons to millennia, evidence of accumulation can be preserved in the sedimentary record as laminae on the order of millimeters, beds on the order of centimeters, and packages on the order of meters. With individual cores, accumulation rates can be calculated from analytical methods such as radioisotope geochronology.

Evidence of morphologic evolution is also preserved in channel-network geometries as they evolve toward a state of equilibrium. Sediment deposition causes tidal-flat aggradation, resulting in a decrease in the tidal prism that the tidal channels must service (Woodroffe, 1985; Wattayakorn et al., 1990). As the morphology approaches equilibrium with sediment- and hydrodynamic-forcing conditions, the rate of

change of channel geometry, including depth, width, and network density, slows dramatically (e.g., van Maanen et al., 2015; Xu et al., 2017).

The presence of stabilizing vegetation influences this temporal evolution. For example, a morphodynamic model developed by van Maanen et al. (2015) demonstrates that the presence of mangrove vegetation influences channel-network geometry in tidal embayments. This morphodynamic model was coupled to a mangrove-population model in order to study how mangroves in sandy tidal embayments influence long-term channel-network evolution. Thus, the coupled models were capable of simulating the interactions between hydrodynamics, sediment transport, and evolving morphology, e.g., flow resistance and erosion thresholds. Qualitative results from numerical simulations that produced channel evolution from an initially unchanneled bathymetry reveal that mangroves first enhance channel branching by concentrating tidal flows and reducing bed erodibility (<160 years), but ultimately produce a seaward retreat of the channel network by promoting accretion and reducing the tidal prism (~1000 years). In general, tidal-flat morphology evolves from clustered networks of small channels to more dispersed and stable networks of large channels, particularly in regions with dense vegetation such as mangroves (van Maanen et al., 2015) and marsh grass (Xu et al., 2017).

Additionally, the relative sinuosity of vegetation-fringed tidal channels may indicate their origin of formation. Channels which completely traverse a landmass, thus having multiple outlets, often form in intertidal zones by the emergence of mobile sand bars (e.g., Souza-Filho et al., 2006; Van Santen et al., 2007). For example, Zeff (1999, 1988) found that these channels, which they identify as “through-flowing” channels, can originate in tidal marshes as flood-tide-delta channels. These through-flowing channels were found to be less sinuous than nearby channels with single outlets, “dead-end” channels, which originated as highly sinuous tidal channels on the marsh islands. Both types of channels can be fixed in place if transient shoals are stabilized by vegetation and cohesive sediment (Zeff, 1988, 1999).

For this study, we use observations of active processes, surface morphology, and bed strata to inform our understanding of past morphologic evolution and predict future changes in surface morphology of a back-barrier tidal-channel network. This approach is followed to create a conceptual model of sediment accumulation and infilling in a macrotidal back-barrier environment that is sediment rich, vegetated by mangroves, incised by tidal channels with multiple outlets, and initially formed landward of an emergent barrier island. The following questions are addressed:

1. What are the morphodynamic feedbacks between channel connectivity, accommodation space, vegetation, hydrodynamics, and sediment deposition in a back-barrier environment?
2. Can the sequential history of geomorphic evolution for a back-barrier tidal-channel system be interpreted using all the following in tandem?
    - *in-situ* observations of water and sediment flux

- measurements of modern sediment accumulation recorded in bed strata
- evidence of equilibrium stability preserved in tidal-channel network geometry

4.1.1 *Study Region*

The Ajuruteua Peninsula, located ~150 km southeast of the Amazon River mouth (Figure 4.1), is in a relatively pristine state. Most prior research along the southeastern Amazonian coastline has been focused on this peninsula, which is bordered by two estuaries, the Taperaçu Estuary to the northwest and the Caeté Estuary to the southeast (Asp et al., 2012, 2016, 2018; Gomes et al., 2013b). The region is macrotidal with spring tidal ranges of ~5-6 m (Asp et al., 2012). Trade winds blow predominantly from the northeast and cause waves to approach the coastline from slightly northward of shore-normal. Consequently, net shore drift is oriented landward along the northern sector and southeastward along the southern sector of the peninsula (Souza-Filho et al., 2003). This wave activity transports sand landward, creating subtidal sand bars that have continually transgressed over an estuarine environment as sea level rose over the past 5100 years (Souza-Filho et al., 2006). As the bed aggraded, the subtidal sand bars gradually transitioned into intertidal shoals, a process described for many other sandy intertidal environments (e.g., Oertel and Overman, 2004; Souza-Filho et al., 2006; Pereira et al., 2016). The intertidal shoals then developed into stable barrier islands as they were colonized by mangroves (Souza-Filho et al., 2006).

Following the end of the postglacial marine transgression 7000 years ago, a sand surplus along this coast allowed for multiple events of coastal progradation via bar emergence and barrier-island formation (Souza-Filho et al., 2009). Data derived from surface sediment samples, deep sediment cores, radiocarbon dating, and pollen analysis allowed for reconstruction of paleo-environmental changes along a 25-km-long shore-normal transect of the Ajuruteua Peninsula (Souza-Filho et al., 2006). This study found stratigraphic evidence for three phases of barrier-island development via sandbar emergence over the past 5100 years, each modulated by small-scale subsidence events and followed by periods of back-barrier infilling (Souza-Filho et al., 2006, 2009). In the past 2100 years, the most significant progradation phase occurred due to a more stable sea level, creating the most recent barrier island. Since the formation of this recent barrier island, intertidal mangrove flats have infilled and prograded >20 km in the back-barrier environment (Souza-Filho et al., 2009).

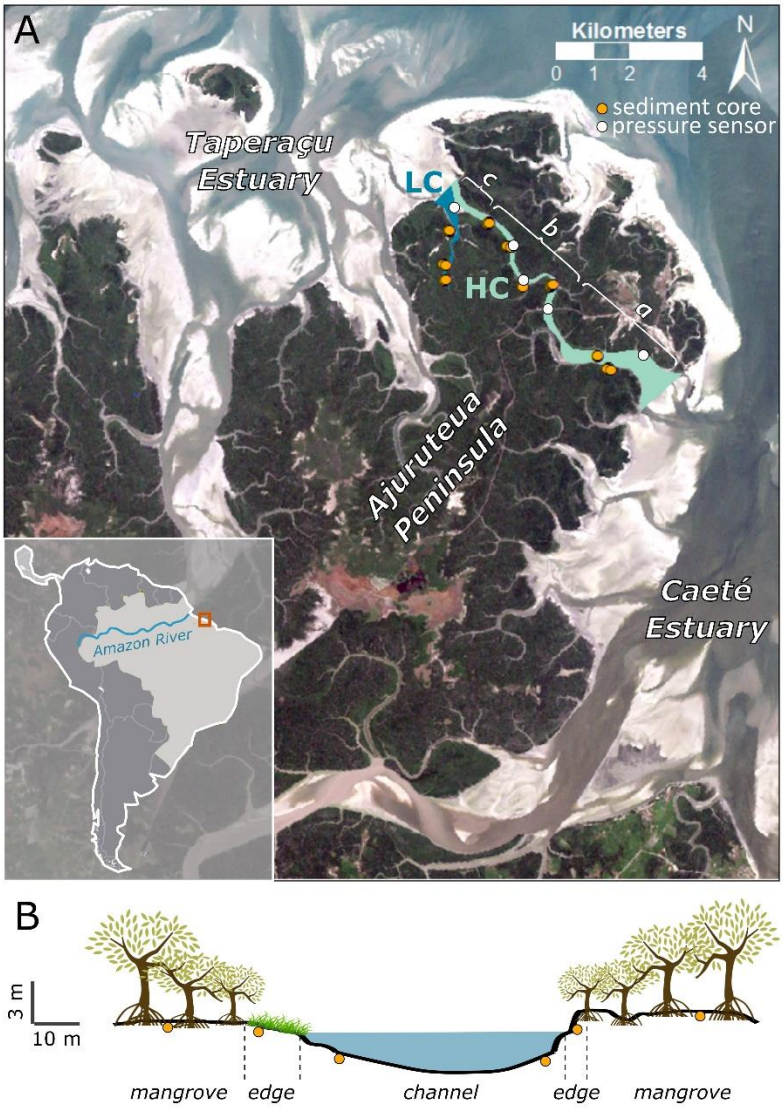

Figure 4.1. A) Map of the Ajuruteua Peninsula on the northern coast of Brazil showing the geography of the low-connectivity (LC) and high-connectivity (HC) channels and adjacent estuaries. Zones of the high-connectivity channel (*a*,*b*,*c*) are delineated with brackets. Satellite image: LandSat TM, 2001, Laboratório de Análise de Imagens do Trópico Úmido. B) Across-channel sampling scheme showing a zoomed in schematic for each transect of cores collected, illustrated as overlapping clusters of yellow dots in the above map. Yellow dots indicate relative locations of sediment cores. White dots indicate locations of pressure sensors.

Today, the barrier is still separated from the mainland by two channels that connect both estuaries: the Taperaçu and the Caeté. These are high-connectivity channels, which are sustained by pressure gradients across the peninsula that produce daily scouring bed stresses (McLachlan et al., 2020). Low-connectivity channels, which connect to a single estuary, are also prominent and further dissect the intertidal back-barrier flats. Primary channels deliver sediment to the mangrove forest directly and indirectly via

flooding of smaller secondary tidal channels that incise the mangrove flats. Channels distribute sediment differently depending on their degree of connectivity. McLachlan et al. (2020) found that the high-connectivity channel acts as a conduit for sediment along the coastline. Because the tidal wave enters both ends of the high-connectivity channel, each with unique bathymetry that influences tidal-wave amplitude and celerity, the resultant along-channel pressure gradient skews velocity toward the Taperaçu Estuary. This velocity asymmetry results in a net flux of suspended sediment northwestward along the channel. The Caeté Estuary, which has a direct fluvial source, supplies sediment to the proximal mangrove flats and to the Taperaçu Estuary, which do not have a direct fluvial source.

High-connectivity channels, like those that traverse the Ajuruteua Peninsula, are common features on the apexes of many peninsulas found along 480 km of coast southeastward from the Amazon River mouth (Souza-Filho et al., 2009). These channels are believed to act as conduits for sediment along the coastline (McLachlan et al., 2020). The along-shore sediment-transport pathways add to the sediment supply of numerous low-connectivity channels that intersect the peninsulas farther inland and import sediment via tidal pumping and sediment trapping within mangrove forests (McLachlan et al., 2020). Research presented here aims to: 1) discern the evolutionary history of these important channels and 2) predict how their role as sediment conduits develops through time and in response to future environmental changes.

4.2 METHODS

4.2.1 *Field Techniques*

Two proximal tidal channels that traverse the Ajuruteua Peninsula were examined in this research: one with high connectivity and one with low connectivity (Figure 4.1). A variety of pressure sensors (RBR Duo, Campbell Scientific OBS 3+, HOBO Onset U20) were deployed along the high-connectivity channel in 2015 (Mar 3-15) and in 2017 (Mar 24-Apr 2), recording measurements at rates $\geq$1 min^{-1} (Figure 4.1). These sensors allowed tidal ranges to be calculated and the rate of tidal-wave propagation to be estimated.

To detect along- and across-channel patterns in grain size, stratigraphy, and accumulation rate, 44 sediment cores were collected throughout the region. Most cores (n=38) were collected in rectangular plexiglass trays (60 x 10 x 2 cm) pushed vertically into the substrate. The trays were stored upright, and x-radiographs were shot within 48 hours after collection to minimize the effects of dewatering and compaction. Cores were then sectioned into 2-cm depth intervals for laboratory analyses. Six additional cores were collected with a cylindrical Russian corer (~5 cm in diameter, <2 m in length) and immediately

sectioned into 4-cm depth intervals; this method allowed for the collection of deeper sediment but precluded x-radiographic examination.

Because tidal-channel network morphology can suggest the relative age of an intertidal environment (e.g., van Maanen et al., 2015; Xu et al., 2017), secondary tidal channels were surveyed where they intersected the primary channels to estimate channel-network density and augment our understanding of regional morphology. In the field, secondary tidal channels were identified along the banks of the two studied primary channels. They were then visually categorized into four size classes (small, medium, large, and extra-large) based on their relative cross-sectional area, and cross-sectional bathymetries of two characteristic channels in each class were measured. Large secondary channels measured ~10-15 m wide and ~2-3 m deep. Channels smaller than ~0.5 m^2 were considered to be relatively ephemeral and not included in the survey.

4.2.2 *Laboratory and Analytical Techniques*

After cores were sectioned into depth intervals and transported to a laboratory, each section was physically homogenized for subsequent analyses. Grain-size distributions were measured in selected intervals of each core using particle-size analyzers, either a Micromeritics Sedigraph (5100, 5120, and 5125) for just the mud fraction (<63 μm) or a Beckman Coulter LS 13 320 for the entire sample.

Accumulation rates for each core were estimated using ^{210}Pb geochronology. ^{210}Pb has a half-life of 22.3 years and can be used to calculate accumulation rates over the past century (Nittrouer et al., 1979). Alpha spectrometry was used to determine the radioactivity of ^{210}Pb by directly measuring that of its granddaughter ^{210}Po, relative to a calibrated ^{209}Po spike. Measured radioactivities were normalized by porosity and percent mud of each sample, to account for down-core variations in grain size, and supported activity was subtracted from total activities to calculate excess ^{210}Pb activities. In the deepest cores, total ^{210}Pb activity below the region of log-linear decay was found to be ~0.75 dpm g^{-1} of mud, so this value was used as the supported level for all cores. Sediment-accumulation rate (S) was then calculated as

$$S = \lambda z / \left[\ln\left(\frac{A_0}{A_z}\right)\right], \tag{4.1}$$

where λ is the ^{210}Pb decay constant (0.0311 yr^{-1}), A_0 and A_z are excess ^{210}Pb activities at two points within the zone of log-linear decay, and z is the distance in depth between the two points. Only log-linear profiles of excess activities with r^2>0.6 were considered to have steady-state accumulation and included in our analysis. To aid in the interpretation of ^{210}Pb profiles and recognize sedimentary structures within cores, x-radiograph negatives were visually examined and characterized.

Because tidal-channel network geometry is expected to evolve from clustered small channels to dispersed large channels as the morphology approaches equilibrium with sediment- and hydrodynamic-forcing conditions (van Maanen et al., 2015; Xu et al., 2017), spatial variations in channel-network geometry may signify the relative age of tidal flats. Therefore, to detect clustering patterns for each size class of secondary tidal channels, survey data were analyzed using the *Multi-Distance Spatial Cluster Analysis* tool in ArcGIS v10.6.1. This tool utilizes Ripley's *K* function (Ripley, 1976, 1977), which determines if features in space exhibit statistically significant clustering or dispersion over a range of distances. Here, the number of secondary channels found within a given distance (*t*) of each individual secondary channel is summed and then compared with the number of channels one would expect from a spatially random sample;

$$K(t) = \frac{A}{n}\sum_{i \neq j}\left[I(d_{ij} < t)/n\right], \tag{4.2}$$

where A is the total surface area of the study region, n is the total number of secondary channels within the study region, d_{ij} is the Euclidean distance between two data points, and I is the indicator function (1 if the operand is true, 0 otherwise). Then, the variance-stabilized Ripley *K* function, called the L function, is calculated so that for a homogenous sample, the expected $L(t)$ will equal the distance, t;

$$L(t) = \sqrt{K(t)/\pi} \tag{4.3}$$

Any observed $L(t)$ greater than that expected from a random spatial pattern is interpreted as channel clustering, while those less than expected are interpreted as channel dispersion.

The confidence interval for the multi-distance spatial cluster analysis was set at 90%, and the geographic boundary was defined as the minimum enclosing rectangle containing all surveyed tidal channels. To reduce the effects of channel sinuosity and variable channel width that would lead to an underestimate of $L(t)$ near the boundary edges, outer-boundary values were simulated by mirroring those found within the boundary.

Additionally, because the relative sinuosity of vegetation-fringed tidal channels may indicate their origin, channel sinuosity (R) was calculated as the ratio between sinuous length and straight length (Pestrong, 1965) measured from satellite imagery with 30-m resolution shown in Figure 4.1 (LandSat TM, 2001, Laboratório de Análise de Imagens do Trópico Úmido).

4.3 RESULTS

To aid in description of along-channel trends, the high-connectivity channel will be discussed in terms of three zones as delineated in Figure 4.1, with *zone a* being nearest the Caeté Estuary, *zone b* extending along the central length of the channel, and *zone c* being nearest the Taperaçu Estuary.

4.3.1 *Channel Width and Tidal Propagation*

The high-connectivity channel is widest at its outlets, reaching ~400 m wide at the Taperaçu Estuary and ~500 m wide at the Caeté Estuary. Its narrowest stretch is in *zone b* on the northwestern end of the channel, ~2.5 km from the Taperaçu Estuary and ~5.5 km from the Caeté Estuary. This narrowest stretch, hereon identified as the pinch point, is roughly collocated with the channel stretch that experiences high tide the latest; high tide occurred almost simultaneously at both ends of the high-connectivity channel and ~12-16 minutes later in the mid-length stretch (Figure 4.2).

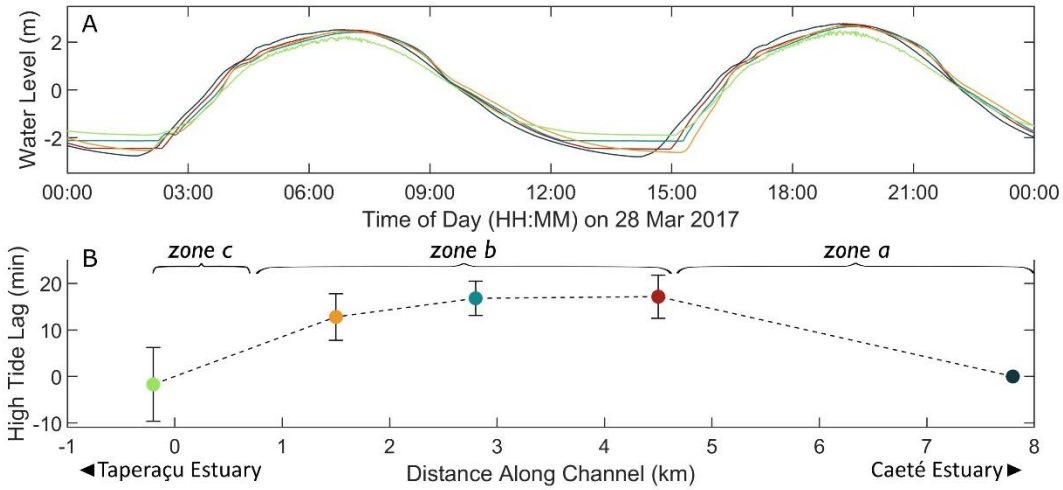

Figure 4.2. A) Characteristic timeseries of water-level variation recorded along the high-connectivity channel. B) The time lag of high tide along the channel, with the eastern-most sensor (nearest the Caeté Estuary) as the reference. Notice that high tides reach both channel outlets around the same time and propagate inland along the channel over 15-20 minutes. Zones along the channel (*a*,*b*,*c*) are delineated with brackets. Colors of both lines and dots represent sensor locations, shifting from dark blue nearest the Caeté Estuary to light green nearest the Taperaçu Estuary.

4.3.2 *Sediment Grain Size, Accumulation Rate, and Sedimentary Structure*

Sediment cores were analyzed to determine along- and across-channel trends in stratigraphy, grain size, and sediment-accumulation rate (Figures 4.3-4.6). Cores were composed of mud and sand, and most exhibited thin, mm-scale laminae. The term 'mud' refers to sediment <63 μm in diameter and includes both silt- and clay-sized sediment. General patterns show that across the channels, from the channel beds to the mangrove forest, grain size tended to fine and stratigraphic layering became less distinct. This same trend was found along the high-connectivity channel from the Caeté Estuary to the Taperaçu Estuary and along the low-connectivity channel from the Taperaçu Estuary inland.

Figure 4.3 displays data collected across the high-connectivity channel ~2 km from the Taperaçu Estuary to demonstrate the type of information retrieved from sediment cores. In general, x-radiographs illustrate that slight down-core variations in mm- to cm-scale stratigraphy exist, though grain-size analyses indicate that the proportional makeup of clay (<4 μm), silt (4-63 μm), and sand (>63 μm) remains nearly consistent in cores collected from the mangrove flat and forest edge. In contrast, cores collected from the channel bed exhibit more within-core variation; many cores exhibit sand layers 1-5 cm thick erratically spaced within clay-dominated laminae. For example, for the characteristic cores displayed (Figure 4.3), the down-core sand fraction varies by ~10% in the mangrove forest, by ~30% on the forest edge, and by ~55% in the channel bed.

Along the high-connectivity channel (Figure 4.4B), grain size of bed sediment tends to fine toward the Taperaçu Estuary; down-core depth-averaged samples were typically >50% mud (D_{50} = 6-29 μm) within 2 km of the Taperaçu Estuary and <50% mud (D_{50} = 162-177 μm) within 2 km of the Caeté Estuary. Across-channel patterns suggest that grain size fines from the channel bed, across the forest edge, and into the mangrove forest. This trend is most extreme in *zone b* of the high-connectivity channel, where typical down-core depth-averaged median grain size was 134-176 μm in the channel and 4-47 μm on the mangrove flats. Along the low-connectivity channel (Figure 4.5B), grain size tends to fine inland, with samples generally <50% mud (D_{50} = 164-177 μm) near the channel mouth and >50% mud (D_{50} = 4-51 μm) near the channel head.

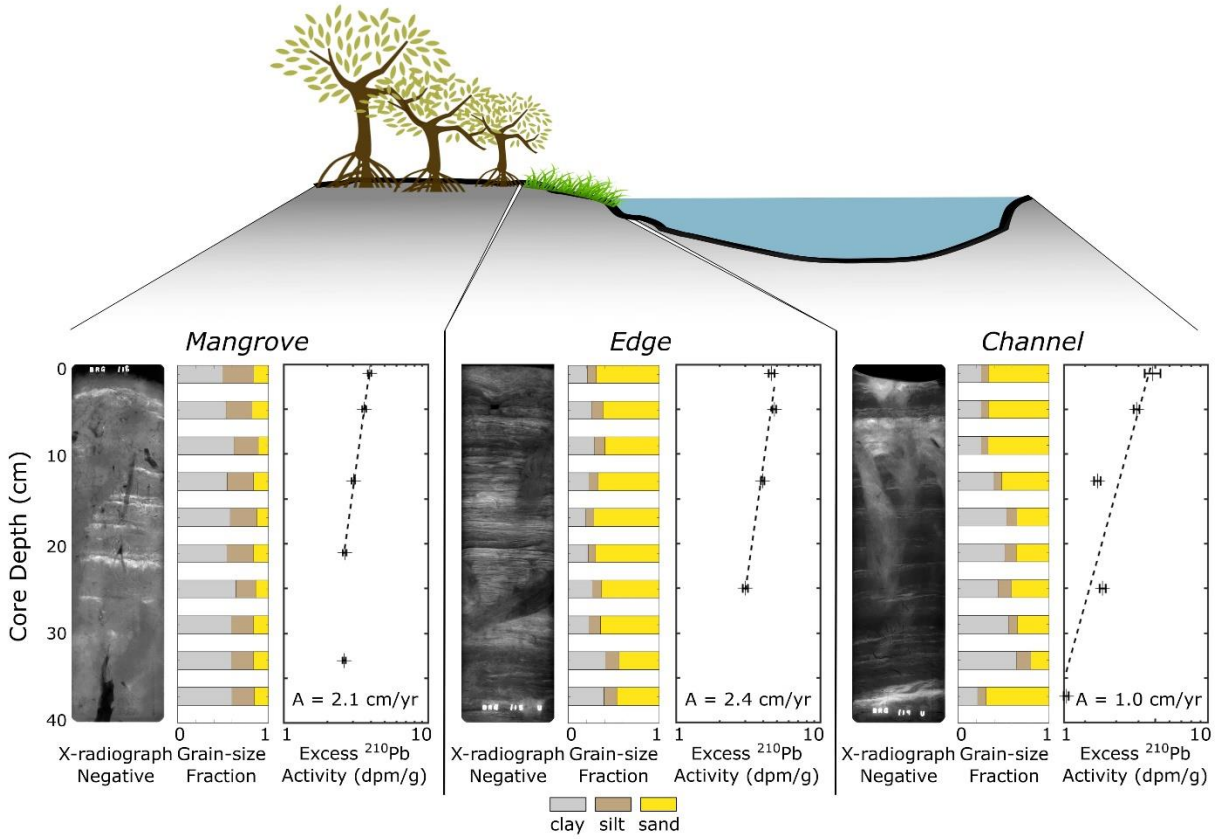

Figure 4.3. Examples of information retrieved from cores: x-radiograph negatives, down-core grain-size fractions, and down-core profiles of excess ^{210}Pb activity. The dashed lines are log-linear regressions, which allow for calculation of the sediment-accumulation rates (A). Grayscale in x-radiograph negatives corresponds to bulk density, with darker shades indicating more mud and lighter shades indicating more sand. Grayscale is consistent within each core but not among cores. Grain-size distributions were measured for alternate 2-cm intervals down each core. Cores were collected across the high-connectivity channel ~2 km from the Taperaçu Estuary.

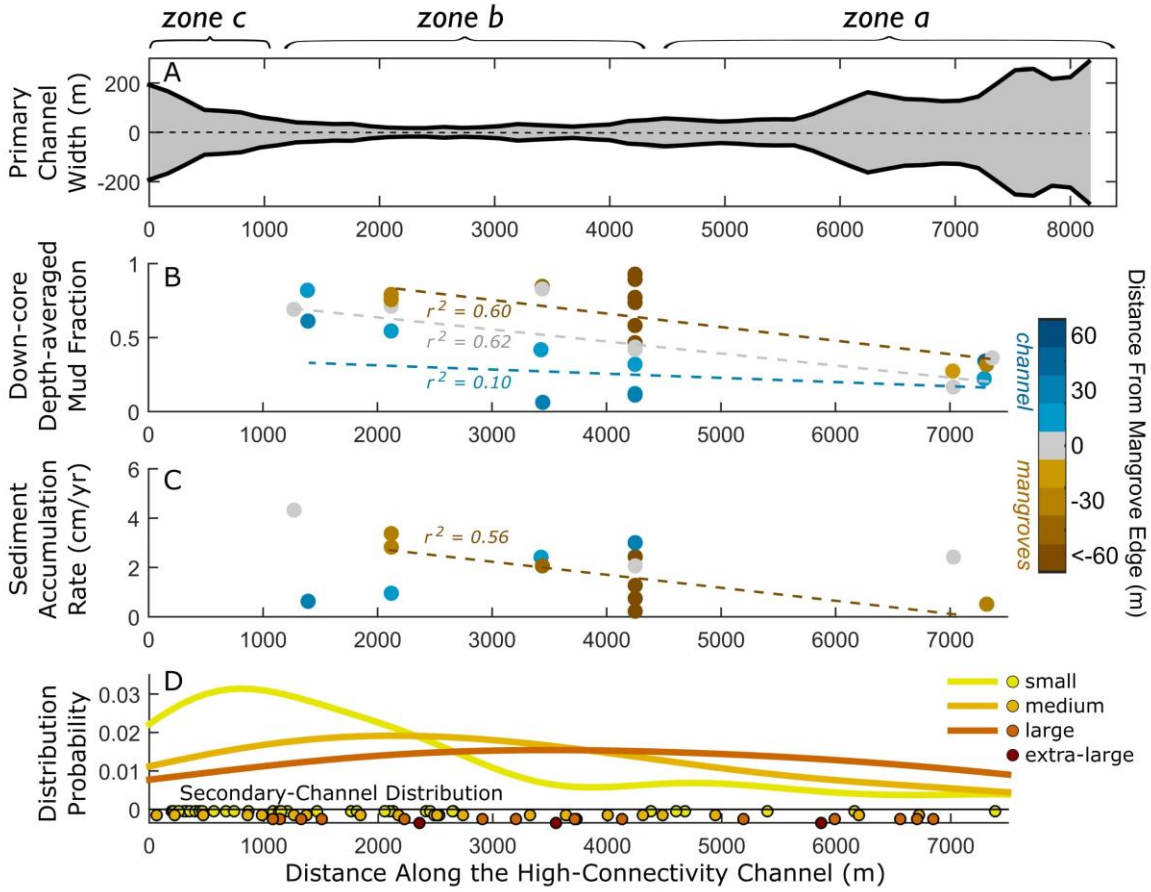

Figure 4.4. Trends along the high-connectivity channel of A) primary-channel width, B) down-core depth-averaged mud fraction (<63µm), C) sediment-accumulation rate calculated from ^{210}Pb geochronology, and D) locations (dots) and probability distributions (lines) of secondary tidal channels where they intersect the primary channel. Zones along the channel (*a*,*b*,*c*) are delineated with brackets. Along-channel distance is measured from the Taperaçu Estuary. Dashed lines represent linear regressions for all cores collected from the channel (blue), mangrove-channel edge (grey), and vegetated mangrove flat (brown).

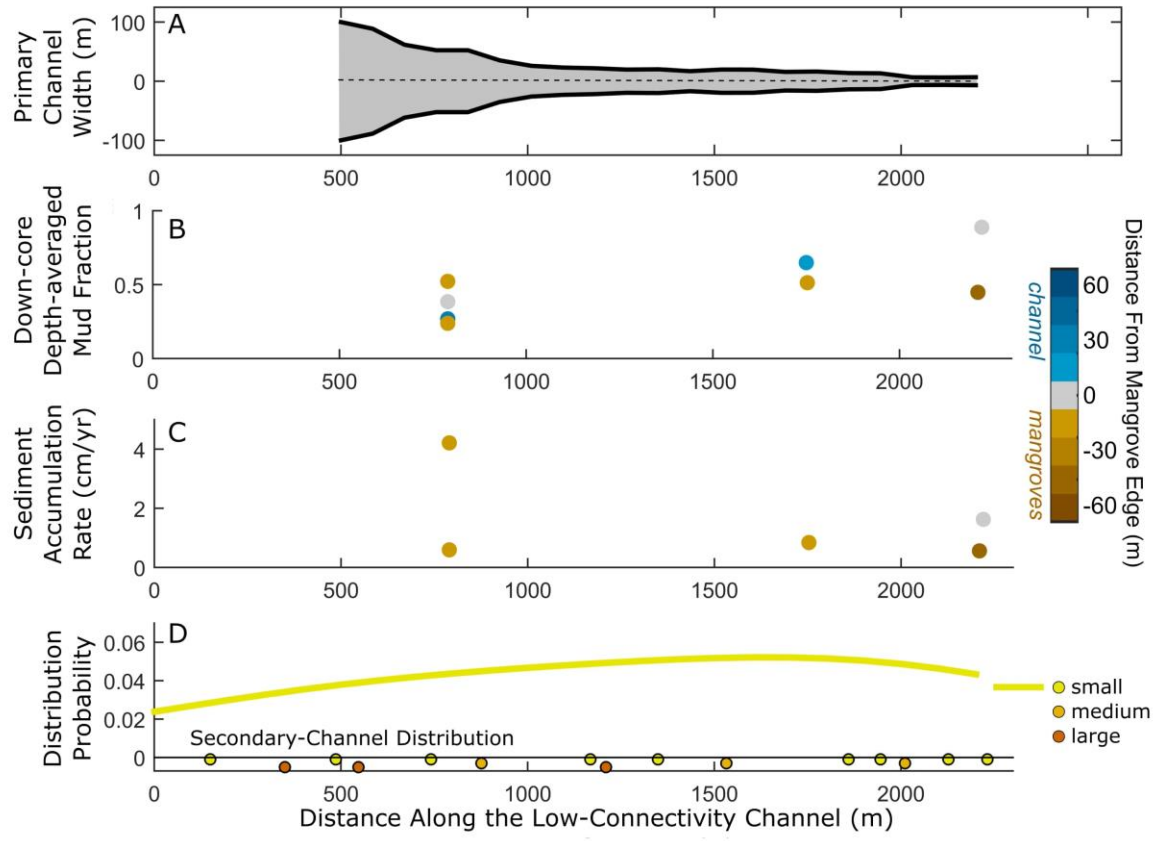

Figure 4.5. Trends along the low-connectivity channel of A) primary-channel width, B) down-core depth-averaged mud fraction (<63µm), C) sediment-accumulation rate calculated from ^{210}Pb geochronology, and D) locations (dots) and probability distributions (lines) of secondary tidal channels where they intersect the primary channel. Along-channel distance is measured from the Taperaçu Estuary.

Stratigraphic analysis also revealed across-channel trends (Figure 4.6) and along-channel trends (Figure 4.7), though substantial local variation was noted. Many cores exhibited thin, mm-scale laminae that alternated between fine- and coarse-grained deposits. Thicker, cm-scale beds were also present and were either comprised of laminae (Figure 4.6) or interrupted surrounding laminae (Figure 4.7). The thin laminae were most distinct in cores collected in *zone a* near the Caeté Estuary and those collected from the unvegetated mangrove-channel edge. Closer to the Taperaçu Estuary in *zone b* and within the mangrove forests, laminae were less distinct and more bioturbation was observed. Variations between cores collected in close proximity were predominately associated with processes that varied on a meter to sub-meter scale, such as vegetation density and the degree of bioturbation.

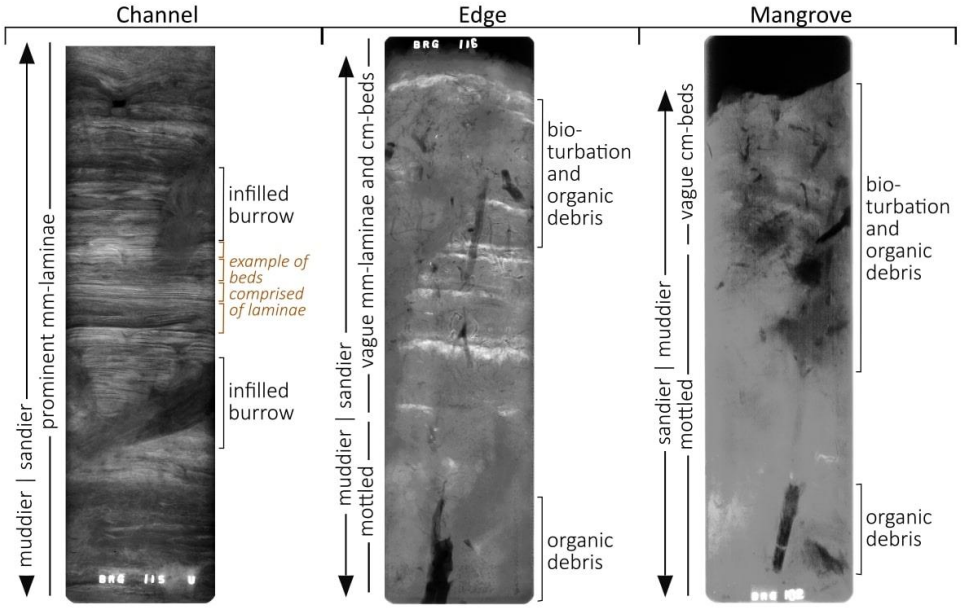

Figure 4.6. X-radiograph negatives and simplified bed descriptions of three characteristic sediment cores that represent across-channel trends and illustrate that the bed becomes more bioturbated moving from the channel into the muddier mangrove forest. Grayscale corresponds to bulk density, with darker shades indicating more mud and lighter shades indicating more sand. Grayscale is consistent within each core but not among cores. X-radiographs are 40-cm long.

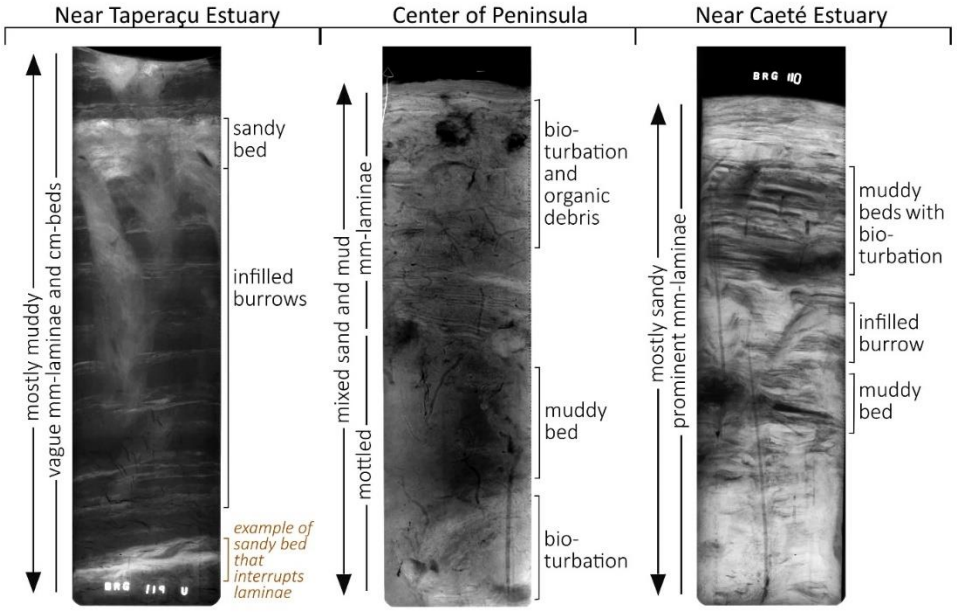

Figure 4.7. X-radiograph negatives and simplified bed descriptions of three characteristic sediment cores that represent along-channel trends and illustrate that the bed becomes muddier with less distinct laminae moving from the Caeté Estuary to the Taperaçu Estuary. All cores were collected from the mangrove-channel edge. Grayscale corresponds to bulk density, with darker shades indicating more mud and lighter shades indicating more sand. Grayscale is consistent within each core but not among cores. X-radiographs are 40-cm long.

Of the 44 cores collected, almost 50% produced reliable sediment-accumulation rates with r^2>0.6, fifteen in the high-connectivity channel and five in the low-connectivity channel. Those that did produce reliable accumulation rates generally contained a relatively large proportion of mud (>30%) and exhibited laminae patterns with limited downcore variation, characteristics more common in the mangrove-forest substrate than the channel bed. Therefore, cores collected from the mangrove forest were most likely to produce steady-state ^{210}Pb profiles and reliable accumulation rates.

Accumulation rates along the low-connectivity channel ranged from 0.5 cm yr^{-1} to >4 cm yr^{-1}, though the small number of cores (*n*=5) limited our ability to find patterns in sediment-accumulation rate there (Figure 4.5C). Along the high-connectivity channel, accumulation rates within the mangrove forest (*n*=8) become progressively greater in the direction of along-channel net sediment flux, increasing from <1 cm yr^{-1} near the Caeté Estuary to >3 cm yr^{-1} near the Taperaçu Estuary (Figure 4.4C). Cores collected from the edge of the mangrove forest (*n*=3) and the channel (*n*=4) did not consistently follow this same pattern.

4.3.3 *Secondary Tidal-Channel Network Geometry*

The secondary tidal-channel survey reveals that these channels are not homogeneously distributed throughout the region (Figure 4.4D, Figure 4.5D, and Figure 4.8). Instead, along the high-connectivity channel, small secondary tidal channels are more concentrated toward the Taperaçu Estuary in *zone c*, whereas medium and large secondary tidal channels are progressively clustered toward the mid-channel length in *zone b*. Multi-distance spatial cluster analysis demonstrates that these spatial patterns are significant (Figure 4.8B-D); small, medium, and large channels show significant clustering at relatively short spatial scales, <300 m, <700 m, and <500 m, respectively. Additionally, small secondary tidal channels are significantly dispersed at large spatial scales >450 m. Because this analysis is not robust for small sample sizes, spatial cluster analyses were not performed on the extra-large channels intersecting the high-connectivity channel (*n*=3) nor on any size class intersecting the low-connectivity channel (*n*<10).

Channel sinuosity was also found to vary throughout the study region. Sinuosity values of the two primary channels were found to be comparable ($R_{high\text{-}connectivity}$ = 1.3, $R_{low\text{-}connectivity}$ = 1.2) and frequently less than those of secondary channels ($R_{secondary}$ = 1.3-2.5) within ~4 km of the primary channels visible in satellite imagery (Figure 4.1).

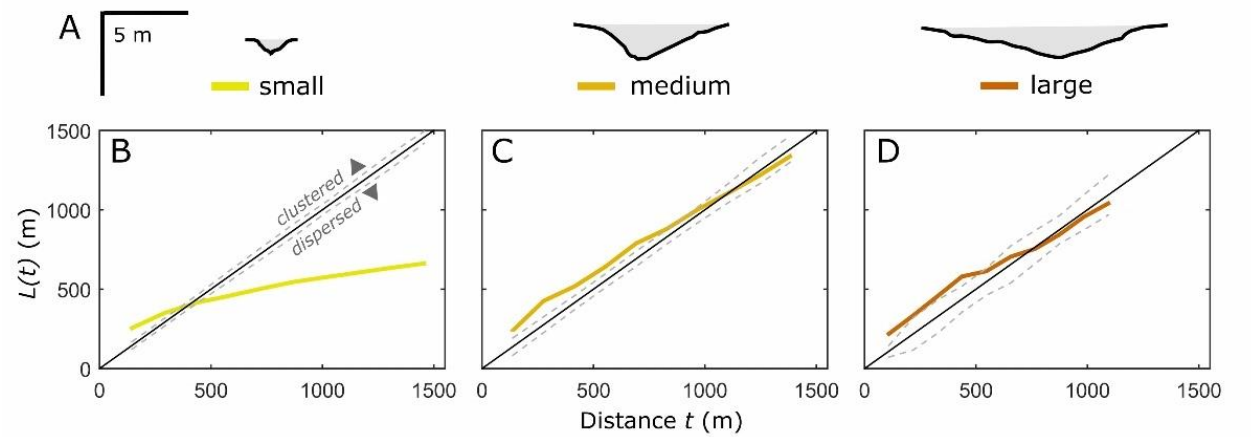

Figure 4.8. A) Measured cross sections of characteristic secondary tidal-channel size classes positioned above the multi-distance spatial cluster analysis of B) small, C) medium, and D) large secondary tidal channels that intersect the high-connectivity channel (associated along-channel distributions are displayed in Figure 4.4D and Figure 4.5D). The 1:1 solid black line represents $L(t)$ expected from a random spatial pattern, and $L(t)$ observed above this line indicate channel clustering, as is observed here for relatively short distances of each channel size class. Dashed lines indicate 90% confidence intervals.

4.4 DISCUSSION

Spatial and temporal trends discussed here allow us to develop a conceptual model of sediment accumulation and infilling in a muddy back-barrier environment vegetated by mangroves. Sediment deposition in this environment appears to occur on timescales from tidal cycles to seasons to episodic events, such as river floods and storm surges. The mm-scale laminae in the accumulating sediment commonly display lenticular bedding (Figure 4.6 and Figure 4.7), alternating between sand and mud, which is often interpreted to represent tidal sedimentation (Reineck and Wunderlich, 1968) in regions such as these vegetated tidal channels with minimal wave influence. The deposits, called tidalites, are created by rhythmic layering of sediment in alternating tidal-velocity regimes, such as ebb/flood flows and spring/neap cycles, and demonstrate the importance of tidal processes for infilling this back-barrier environment.

Though the fine-scale sedimentary structures indicate that accumulation is primarily driven by tidal deposition in this macrotidal environment, spatial variations exist both across and along the channels. Seasonal variability in trade winds and other episodic events are inferred to influence sediment deposition, presenting as cm-scale beds that are comprised of laminae (Figure 4.6) or interrupt the laminae (Figure 4.7). Those that interrupt the laminae are generally composed of relatively coarse sand, indicating high-energy events. These events do not appear to be erosional as the pre-event laminae maintain their bedforms rather than terminate in a characteristically smooth erosional surface.

High-energy events are more likely to impact sedimentation in the channel and at the mangrove edge, rather than in the mangrove forest where turbulence from waves and currents is dampened and little sand is available. Thus, the along-channel trend in accumulation rate found in the mangrove forest, where accumulation rate increases toward the Taperaçu Estuary, probably better represents true regional-scale patterns than the trend found on the mangrove edge and channel bed. The mangrove flats accumulated more persistently with fewer episodic interruptions and produced more reliable calculated sediment-accumulation rates. In contrast, sedimentation within the channel was more susceptible to high-energy events and sandbar migration, both of which would deposit relatively large amounts of sand and would have spatially variable effects on sediment-accumulation rate. Therefore, non-steady-state ^{210}Pb accumulation profiles were more commonly found in cores from the channel bed and mangrove edge.

4.4.1 *Across-Channel Deposition*

Stratigraphic variation was observed in sediment cores collected in close proximity due to meter-scale variability in vegetation density, degree of bioturbation, and mangrove-forest morphology, as has also been observed in mangrove forests by Furukawa et al. (1997), Horstman et al. (2015), and Norris et al. (2017). Cores within the mangrove forest were variably affected by crab burrows and organic debris, which often deformed or masked mm-scale laminae beyond recognition (Figure 4.6) due to the high rates of bioturbation relative to sediment accumulation. Cores from the channel bed and grass-vegetated mangrove edge exhibited cm-scale variations in sand-layer thickness likely because they were variably affected by water velocity during high-energy events; water velocity (i.e. sediment-transport potential) depends on channel morphology and vegetation density.

Despite these variations, patterns in across-channel deposition can be detected. First, all zones from the channel into the mangrove forest are accumulating, with most rates faster than regional eustatic sea-level rise (0.2-0.4 cm yr^{-1}) (Church et al., 2013) as well as average global sea-level rise (0.3 cm yr^{-1}) (Nerem et al., 2010, 2018). Second, accumulation rates on the forest edge tend to exceed those within the adjacent forest by ~1 cm yr^{-1} (Figure 4.4C and Figure 4.5C), consistent with greater subaerial accommodation space near the channel. Elevation of the mangrove edge was up to one meter lower than that of the mangrove flat (Figure 4.1B). Previous work has shown that deposition rates are largely controlled by relative bed elevation within mangrove forests (Wolanski, 1995), and channel banks are prime low-elevation zones that allow accumulation (Walsh and Nittrouer, 2004; Woodroffe et al., 2016).

Similar to results here, Walsh and Nittrouer (2004) found that sediment-accumulation rates of a mangrove bank in the Gulf of Papua were greatest in mid-tidal areas (>4 cm yr^{-1}) and least in high-tidal and low-tidal areas (1-2 cm yr^{-1}). They also found that areas with the most rapid accretion observed via remote

sensing more often had non-steady-state or event-related ^{210}Pb profiles, similar to results here. Together, these findings bolster the conclusion that high-energy events in densely vegetated mangrove environments with minimal fetch and waves are often not erosional, and instead, result in coarse-grained deposits on top of undisturbed pre-event substrate on the channel beds and forest edge.

Sediment grain size also exhibits across-channel patterns, tending to decrease from the channel into the forest due to distal fining. This pattern has been observed in mangrove forests along open shorelines (Fricke et al., 2017b), semi-enclosed bays (Swales et al., 2015), and tidal creeks (Furukawa et al., 1997). Sediment deposited within the channel is a product of both the coarse-grained bedload and the fine-grained suspended load, whereas the mangrove flats receive sediment predominately from suspension settling. Mangrove flats are also less likely to receive coarse-grained sediment because they are less likely to be inundated when peak transport velocities occur in the channel. As a result, deposition of coarser particles drives the aggradation and progradation of channel banks, whereas mangrove flats rely on deposition of finer particles to aggrade (Figure 4.4B).

Biological mixing was found to be more destructive of physical structures in cores collected from the mangrove flats than those within the channel (Figure 4.6), often erasing the presence of mm-scale laminae and leaving only faint remains of cm-scale bedding. This pattern is expected because mangrove-root growth disturbs substrate stratigraphy (e.g., Ferreira et al., 2007; McKee et al., 2007). Additionally, burrowing crabs are common on this peninsula and prefer to burrow in silty rather than sandy sediment (Gomes et al., 2013a).

4.4.2 *Along-Channel Deposition*

The region of tidal convergence, where tidal waves propagating inland from each outlet meet, is estimated to occur in *zone b* of the high-connectivity channel (~1.5-4.5 km from the Taperaçu Estuary), roughly where the channel is the narrowest (~2.5 km from the Taperaçu Estuary). In this stretch, high tide occurs latest (Figure 4.2), indicating that this is where the incursion of flood water from both directions converges.

Foundational research in fluvial geomorphology has shown that hydraulic geometry is determined by the discharge that flows through a channel such that channel width, channel depth, and mean velocity all vary with discharge as simple power functions (Leopold and Maddock, 1953; Myrick and Leopold, 1963). Applying these concepts here, the high-connectivity channel narrows in the direction of tidal convergence presumably because the volume of water it must accommodate, and the intertidal volume it must service via secondary-channel networks, declines along the tidal-flux pathway. Previously collected water-velocity measurements from two locations along the high-connectivity channel, one at the channel's

mid-length and one near the Taperaçu Estuary, corroborate this assumption that tidal convergence coincides with the channel's narrowest stretch. Near the channel's mid-length, ~4 km from either channel mouth, rising tide flowed toward the Taperaçu Estuary (29 Nov 2015; Schettini et al., 2019). During the same tidal phase, closer to the Taperaçu Estuary, ~2 km from the mouth, rising tide briefly reversed direction (<80 minutes) and flowed toward the Caeté Estuary with a tidal excursion of ~1.5-2.0 km (12 Oct 2015; McLachlan et al., 2020). These observations of convergent velocities along the channel further suggest that a convergence zone exists between the two sites where the channel is narrowest.

Along-channel trends in bed grain size can be explained in relation to current strength and proximity to source. During spring tides when water elevations are capable of exceeding bankfull levels (McLachlan et al., 2020), flood-tide convergence occurs in *zone b* when rising water confined within the high-connectivity channel escapes into secondary channels and inundates the mangrove flats. Because the convergence coincides with slow water speeds within the channel (<15 cm s^{-1}) and mangrove forest (<5 cm s^{-1}) (McLachlan et al., 2020), relatively fine sediment is deposited on the channel banks and mangrove flats (typically >50% mud, D_{50} = 4-47 μm). In contrast, faster velocities near the channel mouths in *zones a* and *c* are expected to enhance bed shear stress and hinder deposition of fine sediment, resulting in discrete physical layering due to more active erosion and deposition phases during each tidal cycle. Indeed, bed sediment near the Caeté channel mouth tends to be coarser (Figure 4.4B) with more pronounced laminae (Figure 4.7) than that in the convergence zone. These results and conclusions support those of another study focused on the seasonality of this channel's morphosedimentology (Gomes at al., 2020), which thoroughly mapped channel-bed grain size throughout the high-connectivity channel in both the dry and rainy seasons, and concluded that relatively fine-grained sediment is trapped in the location of tidal-flux convergence (*zone b*) preferentially during the rainy season.

A second reason for sediment fining away from the local Caeté source is because coarser sediment is likely to settle out of suspension and deposit proximally along the sediment-flux pathway. This along-channel pattern could also be a result of differing sediment grain sizes sourced from both estuaries, i.e. the Taperaçu may supply finer sediment to the channel than the Caeté. However, the Taperaçu Estuary does not have a direct fluvial source to supply mud, as the Caeté Estuary does, and both estuaries import sediment from the same offshore source (Souza-Filho et al., 2009). Therefore, mud circulating along the entire high-connectivity channel is probably locally sourced from the Caeté Estuary. This mud is assumed to be reworked and redistributed within the system, with a net northwestward flux within the high-connectivity channel (McLachlan et al., 2020) and through adjacent forests (Schettini et al., 2019).

In addition to the greatest mud fractions, the most rapid sediment accumulation also occurs near the convergence zone. Accumulation rates within the mangrove forest increase from ~0.5 cm yr^{-1} near the Caeté Estuary to >3 cm yr^{-1} near the Taperaçu Estuary (Figure 4.4C). These rates are comparable to those

observed in other mangrove forests, though they tend toward the higher end of the range. In autochthonous mangrove forests which rely on locally produced sediment, such as in the Caribbean region, sediment-accumulation rates are generally <0.5 cm yr^{-1} (Parkinson et al., 1994; McKee et al., 2007). The greatest values for accumulation rates in this study are more similar to those in extensive mangrove stands with large fluvial sediment supplies, such as near the Ganges-Brahmaputra, Fly, and Amazon River mouths, which are generally more rapid: 0.7 cm yr^{-1} (Stanley and Hait, 2000), 4.4 cm yr^{-1} (Walsh and Nittrouer, 2004), and 2.4 cm yr^{-1} (Allison et al., 1995a), respectively. Thus, the rapid accumulation observed here suggests that sediment is delivered from a large fluvial source, i.e., the Amazon River mouth located approximately 150 km to the northwest (Asp et al., 2018).

Rapid accumulation rates are not sustainable with limited intertidal accommodation space, indicating that the spatial distribution of these rates has not persisted since the formation of this back-barrier environment ~2 ka (Souza-Filho et al., 2006). Instead, the location of most rapid accumulation has likely shifted through time, as further explained in the following sections. Land subsidence could also help sustain these rapid accumulation rates. Deep fault-related subsidence is thought to have persisted in the area since the Miocene (Rossetti, 2003), though no major subsidence event has occurred in the past 2 kyr (Souza-Filho et al., 2009). Shallow compaction-related subsidence rates are not known for this region but can range from 0 to 2 cm yr^{-1} in similar mangrove-vegetated environments (e.g., Krauss et al., 2010; McKee et al., 2007).

Secondary tidal channels were found to cluster on the Taperaçu end of the high-connectivity channel in *zone b*. Using multi-distance spatial cluster analysis, clustering of small, medium, and large secondary tidal channels was found to be significant over short distances (Figure 4.8). Dense networks of small channels in a mangrove forest indicate that a location is further away from achieving equilibrium between sediment and hydrodynamic forcing conditions than a location with more sparse networks of large channels (van Maanen et al., 2015; Xu et al., 2017). With this evidence, we conclude that *zone b* of the high-connectivity channel, which has greater accumulation rates over the past century and apparently young secondary tidal channels, is relatively far away from equilibrium. In contrast, *zone a* on the Caeté side of the channel, which has slower accumulation rates over the past century and apparently more mature secondary tidal channels, seems more stable and is assumed to be closer to a dynamic equilibrium.

Sedimentary and morphologic trends observed along the study channels demonstrate the need for sampling over adequate length scales to detect km-scale trends that are often obscured by smaller-scale variability. For the high-connectivity channel, where cores were collected over a 6-km span, along-channel distance accounts for over half of the variance observed in mud fractions and accumulation rates (Figure 4.4B-C). However, any subset of these data that spans <3 km would not produce a coefficient of determination that explained most of the variance. Observations in the low-connectivity channel, spanning

only ~2 km, are consistent with trends in the high-connectivity channel, though the spatial scale is not long enough to confidently establish these trends given the density of core collection. Likewise, analysis of secondary tidal channels along the high-connectivity channel demonstrates that the minimum length scale needed to confidently observe spatial clustering is ~400-800 m, a length scale that is too short to contain a large enough number of secondary channels along the low-connectivity channel for a robust analysis.

4.4.3 *Evolution of Back-Barrier Intertidal Environments on Timescales from Minutes to Millennia*

The high-connectivity channel is assumed to have started forming after the emergence of an offshore sandy bar 2.1 ka (Souza-Filho et al., 2006). The low-connectivity channel may share a similar origin, as both primary channels have comparable sinuosities of ~1.2-1.3. Because the surrounding secondary channels generally have greater sinuosities of ~1.3-2.5, they likely formed in a different manner, such as by incising the intertidal flats that were created after the emergence of the sandy bar (Zeff, 1988). These results suggest that low-connectivity primary channels may originate as high-connectivity channels that infill and eventually pinch off to form two low-connectivity channels. Infilling of densely vegetated high-connectivity channels has been documented in other areas with large sediment supplies, such as the North Inlet–Winyah Bay salt-marsh system in South Carolina, USA, due to persistent sediment accumulation (Traynum and Styles, 2008). Barotropic convergence zones are prime areas for channel infilling because they accumulate sediment fluxing from multiple sediment sources (Warner et al., 2003), and such accumulation associated with tidal convergence has been documented to completely infill and divide high-connectivity channels in estuarine marshes (Collins et al., 1987).

Like these previous studies, we find that at present within a high-connectivity back-barrier environment, the narrowest stretch of the channel coincides with the zone of tidal convergence when hydrodynamics are in equilibrium with cross-sectional area. However, this geometry is not necessarily achieved when the back-barrier environment initially forms, and the location of convergence is expected to shift through time in response to the local morphology as the back-barrier environment infills. Therefore, trends observed here in stratigraphy and morphology spanning several kilometers are used to hypothesize infilling patterns over the past hundred to thousand years as the environment progresses toward morphodynamic equilibrium. Starting from the hypothesized initial morphology of this back-barrier environment 2.1 kya (Souza-Filho et al., 2006), secondary-channel network morphology is used to inform morphologic development over the previous thousand to several hundred years, and information retrieved from sediment cores (sediment-accumulation rates, stratigraphic layers, and grain size) is used to inform sediment infilling over the past hundred years.

The conceptual model proposed here (Figure 4.9) takes into account the modern convergence zone while also incorporating trends observed along the high-connectivity channel: 1) *zone a*, the stretch of channel nearest the Caeté Estuary, is relatively wide and sandy, slowly accumulating sediment, and has morphologically mature secondary tidal channels, whereas 2) *zone b*, the mid-channel-length stretch, is relatively narrow and muddy, is rapidly accumulating sediment, and has morphologically young secondary-tidal channels. We propose that when the high-connectivity channel was young, sediment sourced locally from adjoining estuaries was deposited along the channel, predominantly in *zones a* and *c*. This deposition created sandy shoals and banks composed of tidalites near the channel-estuary confluences as faster settling sands deposited just behind the protecting barrier. This allowed the elevation of the proximal flats to build upward, decreasing accommodation space as well as the volume and hydroperiod of water inundating the flats (e.g., Adame et al., 2010; D'Alpaos et al., 2006; Wolanski et al., 1992). Over time, infilling of these areas became less morphodynamically favorable and accumulation rates slowed due to stronger confined tidal flows within the narrower channel and shorter hydroperiods on the elevated flats. Additionally, bed sediment became coarser with more discrete layering due to more active phases of erosion and deposition during each tidal cycle. Channel-network geometry on the flats evolved as flows through the dense mangroves were focused into large, sparse secondary tidal channels.

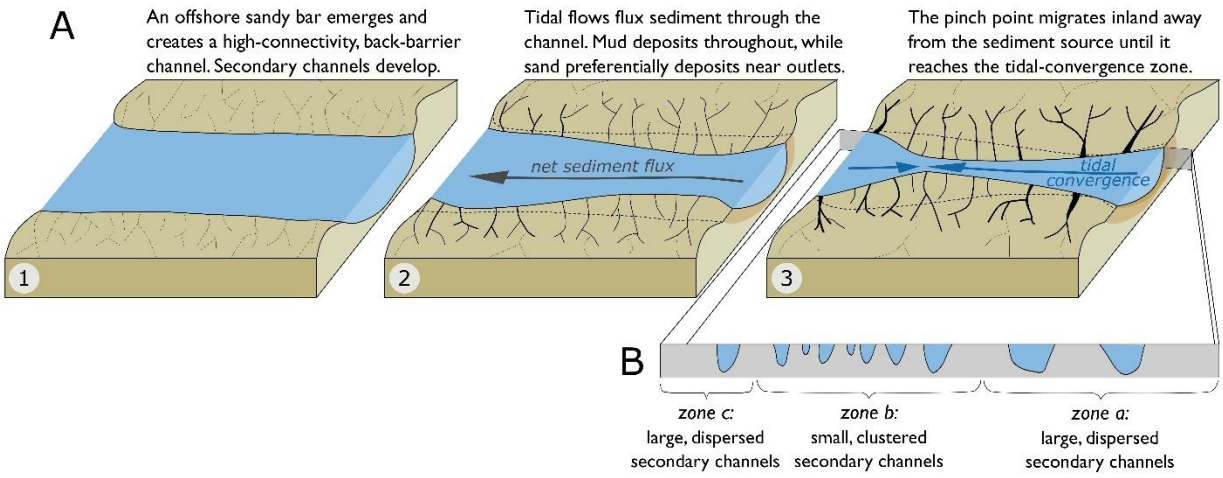

Figure 4.9. A) Conceptual diagram timeseries (1 to 3) illustrating that back-barrier infilling is controlled by the direction of net along-channel sediment flux, available accommodation space, and the location of tidal convergence. B) Along-channel cross section illustrating that zones with recent rapid infilling have secondary tidal channels that are small and clustered (*zone b*), whereas those of more mature zones are large and dispersed (*zones a* and *c*). Channel cross sections are not drawn to scale.

Because the Caeté Estuary supplies much more sediment than the Taperaçu Estuary (McLachlan et al., 2020), *zone a* near the Caeté Estuary likely infilled more quickly than *zone c*. In response to the

decreased accommodation space on the Caeté end of the high-connectivity channel, the location of preferential infilling continually migrated along the channel toward the present region of tidal convergence in *zone b*. In effect, the modern pinch point is positioned just updrift of where sediment is now preferentially infilling and creating relatively young mangrove flats. Because these flats have had less time to evolve toward morphodynamic equilibrium than those near the Caeté Estuary, their secondary tidal channels are relatively small and dense.

We can apply this theory of morphologic evolution to other back-barrier environments that are similarly macrotidal, sediment rich, densely vegetated, incised by tidal channels with multiple outlets, and initially formed landward of an emergent barrier island. In these cases, a back-barrier environment originates as a large, high-connectivity tidal channel with ample accommodation space. As tidal flows continue to move sediment into the back barrier, diminishing accommodation space and channel width, regions of rapid infilling migrate away from channel outlets at rates correlated with the relative sediment supply from each estuarine source. Tidal convergence from the channel outlets becomes more important as flows are confined to smaller channel cross sections and accumulation is focused into areas with greater accommodation space. The channel pinch point will migrate inland away from sediment sources until it reaches a balance in the tidal-convergence zone between processes promoting deposition and available accommodation space. Ultimately, high-connectivity channels could close if tidal pressure gradients are not maintained.

Evidence of previous high-connectivity channel closure is preserved along the Ajuruteua Peninsula in other channels theorized to have been created by sandy bar emergence (Souza-Filho et al., 2006, 2009). The high-connectivity channel studied here is the longest and widest of its kind on the peninsula, whereas its hypothesized predecessors farther inland are significantly smaller or only suggested by two low-connectivity channels that approach each other at their heads. Because these high-connectivity channels are sustained by pressure gradients across the peninsula that produce daily scouring stresses (McLachlan et al., 2020), channel closure may only occur after morphologic shifts reduce the pressure gradient by altering either tidal amplitude or phase lag. Once a channel pinches off to form two low-connectivity channels, the channel will cease to serve as a sediment-flux conduit along the coastline. Instead, it will predominantly import and trap sediment (McLachlan et al., 2020), filling accommodation space that develops due to subsidence and/or sea-level rise. As a result, the higher-order channel heads will infill and the channel lengths will shrink, in accordance with the theory of tidal-channel evolution (van Maanen et al., 2015; Xu et al., 2017). Eventually, along-channel patterns in grain size, accumulation rate, and secondary tidal-channel network geometry discussed here will no longer be discernible in surficial deposits, as seems to be the case with the studied low-connectivity channel.

While mangroves are important for sediment deposition and channel stabilization here, they might not be necessary for this conceptual model to hold true elsewhere because barotropic pressure gradients and flux convergence can promote sediment deposition in other intertidal areas that host high-connectivity channels, such as in marshlands (Collins et al., 1987; Warner et al., 2003). Still, the evolution of morphology proposed can only progress if the flat elevation is not overwhelmed by relative sea-level rise (Woodroffe et al., 2016). Therefore, environments that are able to aggrade quickly, such as those with dense intertidal vegetation that create protected, quiescent settings, are favorable (Van Santen et al., 2007). To assess the broad applicability of this conceptual model, future studies should focus on high-connectivity back-barrier channels in a variety of other densely vegetated environments, including other mangrove forests and marshlands.

4.5 CONCLUSION

Understanding how back-barrier environments infill and evolve is necessary to predict how these regions will respond to future changes in sea level and sediment supply. With this motivation, active processes, surface morphology, and bed strata from an Amazonian tidal-channel system were interpreted to create an evidence-based conceptual model of past morphologic evolution in a macrotidal back-barrier environment vegetated by mangroves. This study corroborates others that attribute sustained infilling in back-barrier environments to protective barriers that create quiescent conditions for sediment deposition (e.g., Benallack et al., 2016; Sloss et al., 2005; Thorbjarnarson et al., 1985; Zeff, 1988) and tidal-convergence zones that accumulate sediment (Collins et al., 1987; Warner et al., 2003; Traynum and Styles, 2008). We add an understanding of the relationships between tidal convergence, accommodation space, and channel connectivity, as well as their impacts on sediment-flux pathways and secondary channel-network geometry, to our conceptual understanding of morphologic evolution in these environments.

Within high-connectivity back-barrier environments, sediment is deposited over tidal timescales, aggrading the bed upwards and diminishing channel volume. As accommodation space becomes limited and tidal dynamics dominate flows in channels with smaller cross sections, the regions of preferential infilling migrate away from the local sediment sources and toward the tidal convergence zone. In some cases, sediment infilling may pinch off high-connectivity channels to form two low-connectivity channels, altering sediment-flux pathways; high-connectivity channels serve to distribute sediment along a coastline and supply sediment to regions with less direct sources, whereas low-connectivity channels preferentially import and trap sediment inland.

These findings shed light on how sediment transported through vegetated back-barrier environments is ultimately preserved, and how the geologic record and surface morphology can be

interpreted. Where length scales allow, the sequential history of geomorphic evolution may be interpreted with observations of active processes, surface morphology, and bed strata. The location of recent preferential infilling is evidenced by narrow channel widths, rapid sediment-accumulation rates, relatively fine sediment, and clustering of small secondary tidal channels. This conceptual model should be tested within other similar environments to validate its broad applicability, to confine the spatial and temporal scales necessary for observing the trends discussed, and to determine other influencing variables such as initial back-barrier morphology.

Chapter 5.
SUMMARY

Rivers deliver most of the sediment that reaches the global ocean, and those with great sediment discharges, including the Amazon and Mekong rivers, are often sourced from large mountains, transit great distances, and discharge in tropical environments. Upon nearing the marine realm, tide-influenced channels often serve as the primary flux conduits directing sediment through the coastal environment. Therefore, channel geometry is key to determining sediment dispersal within delta distributaries and along coastlines. The objective of this research is to determine the impact of channel depth and connectivity on sedimentary processes and predict the consequent geomorphorphic change.

In river deltas, channel bifurcations control the division of water and sediment across downstream distributaries. These bifurcations add complexity to vertical mixing and longitudinal sediment flux, especially where tides produce bidirectional flow. Thus, the geometry of channel bifurcations, and their spatial relationship to tidal and estuarine processes, control sediment distribution and morphologic development of tide-influenced deltas. In Chapter 2, research is described that elucidates how channel depth controls sediment-flux partitioning in tidal rivers. This research is important to predict future morphologic changes, particularly considering that estuarine regimes are intruding farther into many of the world's largest and most populated deltas.

Sediment-flux partitioning was measured upstream of a channel bifurcation in the Mekong River Delta that seasonally transitions from a tidal-river to estuarine regime. Sampling was concentrated over two subchannels; the deep subchannel flows into the larger distributary while the shallow subchannel flows into the smaller distributary. Suspended particles in the tidal river were predominately microflocs with effective densities of 0.05-0.3 g cm^{-1} and settling velocities <0.5 mm s^{-1}. The finest particles dominated the mass settling fluxes, so the less frequent formation of larger microflocs and macroflocs had minimal influence on potential sediment deposition.

Although subchannel depth did not meaningfully impact particle settling rates, it did influence sediment distribution via its effect on flow velocity and vertical mixing. In the deep subchannel, where seaward flows ebb into a larger cross-sectional area, tidal velocity is symmetric, and the residual sediment flux is near zero. In contrast, in the shallow subchannel, where ebb flows are confined to a smaller cross section, flow velocity and shear are ebb dominant. Consequently, much sediment is resuspended from the bed during ebb flows. When sediment concentrations exceed ~400 mg L^{-1}, sediment-induced stratification inhibits vertical mixing.

As a result, when the bifurcation is a tidal river, residual sediment flux is directed upstream from the shallow distributary and downstream to the deep distributary. The flux direction is opposite when estuarine processes persist at the bifurcation, suggesting that decreased fluvial discharge will shift sediment flux more often toward the shallow distributary. These results are likely applicable to other tidally influenced deltas that have large supplies of fine-grained sediment, low channel sinuosity, and distributaries of similar lengths. In these deltas, the predicted global increase in seasonal sediment trapping due to estuarine intrusion may be disproportionately large in relatively shallow distributaries. Future modeling efforts should consider the effect of channel depth on sediment-induced stratification and consequential distribution of suspended sediment.

Sediment that is discharged from rivers mouths may be fluxed along the shallow continental shelf before being imported into tidal channels and deposited back onshore. This sediment-dispersal pathway is thought to be the primary source of sediment and nutrients needed by the world's largest continuous stand of mangroves southeast of the Amazon River mouth. This stand is bisected by numerous tidal channels that connect to one or more bodies of water. The morphodynamics of mangrove forests, including the impact of tidal-channel connectivity on sediment transport, must be understood to effectively manage these highly productive, though globally threatened, environments. In Chapter 3, hydrodynamics and sediment dynamics are observed and analyzed for two tidal channels, and the impact of channel connectivity on sediment distribution is evaluated.

Within the low-connectivity channel, tidal duration and tidal velocity are in quadrature. Both are landward dominant when tidal ranges remain below the elevation of the mangrove flats. When water overtops the flats, the tidal-velocity asymmetry is temporarily skewed seaward due to the development of ebb-tidal pulses. Even so, sediment is consistently imported inland.

In contrast, tidal duration and tidal velocity are not in quadrature within the high connectivity channel, and a residual flow skews water and sediment fluxes. The greatest sediment flux occurs during strong ebb-tidal pulses. Therefore, the net direction of sediment flux is determined by the direction of along-channel flow concurrent with the ebb-tidal pulse. High-connectivity channels act as conduits for water and sediment along the coastline, dispersing sediment far away from fluvial sources. Furthermore, although channel connectivity influences both the source and volume of sediment available to the surrounding mangrove forest, it does not affect the processes that distribute sediment inside the mangrove forests.

These sediment-dispersal processes, which were observed over tidal timescales, can also help elucidate the long-term evolution of this coastline, which is thought to have formed over the last 7000 years by repeated events of sand-bar emergence and subsequent back-barrier infilling. Understanding how back-barrier environments infill and evolve is necessary to predict how these regions will respond to future changes in sea level and sediment supply. Research presented in Chapter 4 expands upon modern

observations in Chapter 3 to conceptualize how the morphology of this back-barrier environment has progressed over the past two millennia.

Within high-connectivity back-barrier environments, sediment deposition occurs predominately over tidal timescales. As deposition limits accommodation space, tidal dynamics become more dominant in channels with smaller cross sections. Consequently, the regions of preferential infilling migrate away from the local sediment sources and toward the tidal convergence zone. In some cases, sediment infilling may pinch off high-connectivity channels to form two low-connectivity channels, altering sediment-flux pathways; high-connectivity channels serve as conduits that distribute sediment along a coastline, whereas low-connectivity channels preferentially import and trap sediment inland.

These findings explain how sediment transported through vegetated back-barrier environments may be ultimately preserved and improve our ability to interpret the geologic record and surface morphology. Where length scales are sufficient, the sequential history of geomorphic evolution can be informed by observations of active processes, surface morphology, and bed strata. The location of recent preferential infilling in a high-connectivity channel is evidenced by narrow widths of the primary tidal channel, rapid sediment-accumulation rates of the vegetated flats, relatively fine bed sediment, and clustering of small secondary tidal channels. To accurately model high-connectivity channels in back-barrier environments, the morphodynamic feedbacks between channel bathymetry, tidal-wave propagation, and the location of flux convergence, as well as the impact of densely vegetated intertidal flats on channel hydrodynamics, should be carefully considered.

Together, the three research projects presented here further our understanding of the role that channel morphology plays in sediment dispersal and morphologic development of tide-influenced channels. The shape of tide-influenced channels and the sediment-transport pathways through them are morphodynamically linked, such that channel geometry dictates sediment dispersal, and sediment dispersal can change channel geometry. This work contributes to the growing body of knowledge about the sedimentary processes that shape our coastlines, and our ability to interpret geologic evidence that records their geomorphic change.

BIBLIOGRAPHY

Adams, C.E. and **Weatherly, G.L.** (1981) Suspended-sediment transport and benthic boundary-layer dynamics. *Mar. Geol.*, **42**, 1–18.

Adams, C.E., Wells, J.T. and **Park, Y.A.** (1990) Internal hydraulics of a sediment-stratified channel flow. *Mar. Geol.*, **95**, 131–145.

Akter, R., Asik, T.Z., Sakib, M., Akter, M., Sakib, M.N., Al Azad, A.S.M.A., Maruf, M., Haque, A. and **Rahman, M.M.** (2019) The dominant climate change event for salinity intrusion in the GBM Delta. *Climate*, **7**, 1–23.

Adame, M.F., **Neil, D.**, **Wright, S.F.** and **Lovelock, C.E.** (2010) Sedimentation within and among mangrove forests along a gradient of geomorphological settings. *Estuar. Coast. Shelf Sci.*, **86**, 21–30.

Adams, C.E. and **Weatherly, G.L.** (1981) Suspended-sediment transport and benthic boundary-layer dynamics. *Mar. Geol.*, **42**, 1–18.

Adams, C.E., **Wells, J.T.** and **Park, Y.A.** (1990) Internal hydraulics of a sediment-stratified channel flow. *Mar. Geol.*, **95**, 131–145.

Akter, R., **Asik, T.Z.**, **Sakib, M.**, **Akter, M.**, **Sakib, M.N.**, **Al Azad, A.S.M.A.**, **Maruf, M.**, **Haque, A.** and **Rahman, M.M.** (2019) The dominant climate change event for salinity intrusion in the GBM Delta. *Climate*, **7**, 1–23.

Ali, A., **Mynett, A.E.** and **Azam, M.H.** (2007) Sediment dynamics in the Meghna Estuary, Bangladesh: A model study. *J. Waterw. Port, Coastal, Ocean Eng.*, **133**, 255–263.

Allison, M.A., **Dallon Weathers, H.** and **Meselhe, E.A.** (2017) Bottom morphology in the Song Hau distributary channel, Mekong River Delta, Vietnam. *Cont. Shelf Res.*, **147**, 51–61.

Allison, M.A., **Lee, M.T.**, **Ogston, A.S.** and **Aller, R.C.** (2000) Origin of Amazon mudbanks along the northeastern coast of South America. *Mar. Geol.*, **163**, 241–256.

Allison, M.A., **Nittrouer, C.A.** and **Faria Jr, L.E.C.** (1995a) Rates and mechanisms of shoreface progradation and retreat downdrift of the Amazon River mouth; Geological significance of sediment transport and accumulation on the Amazon continental shelf. *Mar. Geol.*, **125**, 373–392.

Allison, M.A., **Nittrouer, C.A.** and **Kineke, G.C.** (1995b) Seasonal sediment storage on mudflats adjacent to the Amazon River. *Mar. Geol.*, **125**, 303–328.

Alongi, D.M. (2002) Present state and future of the world's mangrove forests. *Environ. Conserv.*, **29**, 331–349.

Anh, D.T., **Hoang, L.P.**, **Bui, M.D.** and **Rutschmann, P.** (2018) Simulating future flows and salinity intrusion using combined one- and two-dimensional hydrodynamic modelling-the case of Hau River, Vietnamese Mekong Delta. *Water*, **10**, 1–21.

Asp, N.E., **Amorim de Freitas, P.T.**, **Gomes, V.J.C.** and **Gomes, J.D.** (2013) Hydrodynamic overview and seasonal variation of estuaries at the eastern sector of the Amazonian coast. *J. Coast. Res.*, **165**, 1092–1097.

Asp, N.E., **Gomes, V.J.C.**, **Ogston, A.**, **Borges, J.C.C.** and **Nittrouer, C.A.** (2016) Sediment source, turbidity maximum, and implications for mud exchange between channel and mangroves in an Amazonian estuary. *Ocean Dyn.*, **66**, 285–297.

Asp, N.E., **Gomes, V.J.C.**, **Schettini, C.A.F.**, **Souza-Filho, P.W.M.**, **Siegle, E.**, **Ogston, A.S.**, **Nittrouer, C.A.**, **Silva, J.N.S.**, **Nascimento, W.R.**, **Souza, S.R.**, **Pereira, L.C.C.** and **Queiroz, M.C.** (2018) Sediment dynamics of a tropical tide-dominated estuary: Turbidity

maximum, mangroves and the role of the Amazon River sediment load. *Estuar. Coast. Shelf Sci.*, **214**, 10–24.

Asp, N.E., **Schettini, C.A.F.**, **Siegle, E.**, **da Silva, M.S.** and **de Brito, R.N.R.** (2012) The dynamics of a frictionally-dominated Amazonian estuary. *Brazilian J. Oceanogr.*, **60**, 391–403.

Aubrey, D.G. (1986) Hydrodynamic controls on sediment transport in well-mixed bays and estuaries. *Phys. Shallow Estuaries Bays*, **16**, 245–258.

Aucan, J. and **Ridd, P.V.** (2000) Tidal asymmetry in creeks surrounded by saltflats and mangroves with small swamp slopes. *Wetl. Ecol. Manag.*, **8**, 223–231.

Bagnold, R.A. (1966) An approach to the sediment transport problem from general physics. *USGS Prof. Pap.*, **422**, 42.

Barendregt, A. and **Swarth, C.W.** (2013) Tidal freshwater wetlands: Variation and changes. *Estuaries and Coasts*, **36**, 445–456.

Bayliss-Smith, T.P., **Healey, R.**, **Lailey, R.**, **Spencer, T.** and **Stoddart, D.R.** (1979) Tidal flows in salt marsh creeks. *Estuar. Coast. Mar. Sci.*, **9**, 235–255.

Benallack, K., **Green, A.N.**, **Humphries, M.S.**, **Cooper, J.A.G.**, **Dladla, N.N.** and **Finch, J.M.** (2016) The stratigraphic evolution of a large back-barrier lagoon system with a non-migrating barrier. *Mar. Geol.*, **379**, 64–77.

Boldt, K.V., **Nittrouer, C.A.** and **Ogston, A.S.** (2013) Seasonal transfer and net accumulation of fine sediment on a muddy tidal flat: Willapa Bay, Washington. *Cont. Shelf Res.*, **60**, S157–S172.

Bolla Pittaluga, M., **Coco, G.** and **Kleinhans, M.G.** (2015) A unified framework for stability of channel bifurcations in gravel and sand fluvial systems. *Geophys. Res. Lett.*, **42**, 7521–7536.

Bonneton, N., **Bonneton, P.**, **Parisot, J.**, **Sottolichio, A.** and **Detandt, G.** (2012) Tidal bore and Mascaret – example of Garonne and Seine Rivers. *Comptes Rendus Geosci.*, **344**, 508–515.

Boon, J.D. and **Byrne, R.J.** (1981) On basin hypsometry and the morphodynamic response of coastal inlet systems. *Mar. Geol.*, **40**, 27–48.

Bowden, K.F. (1981) Turbulent mixing in estuaries. *Ocean Manag.*, **6**, 117–135.

Budiyanto, F. and **Lestari, L.** (2013) Study of metal contaminant level in the Mahakam Delta: Sediment and dissolved metal perspectives. *J. Coast. Dev.*, **16**, 147–157.

Burban, P.-Y., **Lick, W.** and **Lick, J.** (1989) The flocculation of fine-grained sediments in estuarine waters. *J. Geophys. Res.*, **94**, 8323–8330.

Burchard, H., **Schuttelaars, H.M.** and **Ralston, D.K.** (2018) Sediment trapping in estuaries. *Ann. Rev. Mar. Sci.*, **10**, 14.1–14.25.

Buschman, F.A., **Van Der Vegt, M.**, **Hoitink, A.J.F.** and **Hoekstra, P.** (2013) Water and suspended sediment division at a stratified tidal junction. *J. Geophys. Res. Ocean.*, **118**, 1459–1472.

Canestrelli, A., **Fagherazzi, S.**, **Defina, A.** and **Lanzoni, S.** (2010) Tidal hydrodynamics and erosional power in the Fly River delta, Papua New Guinea. *J. Geophys. Res.*, **115**, 1–14.

Chernetsky, A.S., **Schuttelaars, H.M.** and **Talke, S.A.** (2010) The effect of tidal asymmetry and temporal settling lag on sediment trapping in tidal estuaries. *Ocean Dyn.*, **60**, 1219–1241.

Christiansen, T., **Wiberg, P.L.** and **Milligan, T.G.** (2000) Flow and sediment transport on a tidal salt marsh surface. *Estuar. Coast. Shelf Sci.*, **50**, 315–331.

Church, J.A., **Clark, P.U.**, **Cazenave, A.**, **Gregory, J.M.**, **Jevrejeva, S.**, **Levermann, A.**, **Merrifield, M.A.**, **Milne, G.A.**, **Nerem, R.**., **Nunn, P.D.**, **Payne, A.J.**, **Pfeffer, W.T.**,

Stammer, D. and **Unnikrishnan, A.S.** (2013) Sea level change. In: *Climate Change 2013: The Physical Science Basis. Contribution of Working Group I to the Fifth Assessment Report of the Intergovernmental Panel on Climate Change* (Ed. T.F. Stocker, D. Qin, G.K. Plattner, M. Tignor, S.K. Allen, J. Boschung, A. Nauels, Y. Xia, V. Bex, and P.M. Midgley), *Cambridge University Press*, Cambridge, United Kingdom and New York, NY, USA, 1137–1216.

Collins, L.M., **Collins, J.N.** and **Leopold, L.B.** (1987) Geomorphic processes of an estuarine marsh: Preliminary results and hypotheses. In: *International Geomorphology 1986, Part 1* (Ed. V. Gardiner), *John Wiley & Sons Ltd.*, New York, 1, 1024–1072.

D'Alpaos, A., **Lanzoni, S.**, **Mudd, S.M.** and **Fagherazzi, S.** (2006) Modeling the influence of hydroperiod and vegetation on the cross-sectional formation of tidal channels. *Estuar. Coast. Shelf Sci.*, **69**, 311–234.

Dahdouh-Guebas, F., **Jayatissa, L.P.**, **Di Nitto, D.**, **Bosire, J.O.**, **Lo Seen, D.** and **Koedam, N.** (2005) How effective were mangroves as a defence against the recent tsunami? *Curr. Biol.*, **15**, R443–R447.

Dalrymple, R.W. and **Choi, K.** (2007) Morphologic and facies trends through the fluvial-marine transition in tide-dominated depositional systems: A schematic framework for environmental and sequence-stratigraphic interpretation. *Earth-Science Rev.*, **81**, 135–174.

Danielsen, F., **Sørensen, M.K.**, **Olwig, M.F.**, **Selvam, V.**, **Parish, F.**, **Burgess, N.D.**, **Hiraishi, T.**, **Karunagaran, V.M.**, **Rasmussen, M.S.**, **Hansen, L.B.**, **Quarto, A.** and **Suryadiputra, N.** (2005) The Asian tsunami: A protective role for coastal vegetation. *Sci. Brevia*, **310**, 643.

Darby, S.E., **Hackney, C.R.**, **Leyland, J.**, **Kummu, M.**, **Lauri, H.**, **Parsons, D.R.**, **Best, J.L.**, **Nicholas, A.P.** and **Aalto, R.** (2016) Fluvial sediment supply to a mega-delta reduced by shifting tropical-cyclone activity. *Nature*, **569**, 276–279.

de Beaumont, L.E. (1845) Septieme lechón. In: *Lecons de geologie pratique*, *Bertrand*, Paris, 221–252.

Donato, D.C., **Kauffman, J.B.**, **Murdiyarso, D.**, **Kurnianto, S.**, **Stidham, M.** and **Kanninen, M.** (2011) Mangroves among the most carbon-rich forests in the tropics. *Nat. Geosci.*, **4**, 293–297.

Driscoll, N. and **Nittrouer, C.** (2000) Source to sink studies. MARGINS Newsl. No. 5

Dronkers, J. (1986) Tidal asymmetry and estuarine morphology. *Netherlands J. Sea Res.*, **20**, 117–131.

Duke, N.C., **Meynecke, J.O.**, **Dittmann, S.**, **Ellison, A.M.**, **Berger, U.**, **Cannicci, S.**, **Diele, K.**, **Ewel, K.C.**, **Field, C.D.**, **Koedam, N.**, **Lee, S.Y.**, **Marchand, C.**, **Nordhaus, I.** and **Dahdouh-Guebas, F.** (2007) A world without mangroves? *Sci. Lett.*, **317**, 41–43.

Dunne, T., **Mertes, L.A.K.**, **Meade, R.H.**, **Richey, J.E.** and **Forsberg, B.R.** (1998) Exchanges of sediment between the flood plain and channel of the Amazon River in Brazil. *Bull. Geol. Soc. Am.*, **110**, 450–467.

Dyer, K.R. and **Manning, A.J.** (1999) Observation of the size, settling velocity and effective density of flocs, and their fractal dimensions. *J. Sea Res.*, **41**, 87–95.

Edmonds, D.A. and **Slingerland, R.L.** (2008) Stability of delta distributary networks and their bifurcations. *Water Resour. Res.*, **44**, 1–13.

Edmonds, D.A. and **Slingerland, R.L.** (2007) Mechanics of river mouth bar formation: Implications for the morphodynamics of delta distributary networks. *J. Geophys. Res.*, **112**, 1–14.

Eidam, E.F., **Nittrouer, C.A.**, **Ogston, A.S.**, **DeMaster, D.J.**, **Liu, J.P.**, **Nguyen, T.T.** and

Nguyen, T.N. (2017) Dynamic controls on shallow clinoform geometry: Mekong Delta, Vietnam. *Cont. Shelf Res.*, **147**, 165–181.

Ensign, S.H., **Doyle, M.W.** and **Piehler, M.F.** (2013) The effect of tide on the hydrology and morphology of a freshwater river. *Earth Surf. Process. Landforms*, **38**, 655–660.

Ensign, S.H., **Noe, G.B.**, **C.R., H.** and **Fagherazzi, S.** (2012) A meeting of the waters: interdisciplinary challenges and opportunities in tidal rivers. *Eos (Washington. DC).*, **93**, 455–456.

Erban, L.E., **Gorelick, S.M.** and **Zebker, H.A** (2014) Groundwater extraction, land subsidence, and sea-level rise in the Mekong Delta, Vietnam. *Environ. Res. Lett.*, **9**, 1–6.

Ericson, J.P., **Vörösmarty, C.J.**, **Dingman, S.L.**, **Ward, L.G.** and **Meybeck, M.** (2006) Effective sea-level rise and deltas: Causes of change and human dimension implications. *Glob. Planet. Change*, **50**, 63–82.

Eslami, S., **Hoekstra, P.**, **Kernkamp, H.**, **Trung, N.N.**, **Do Duc, D.**, **Quang, T.T.**, **Februarianto, M.**, **Van Dam, A.** and **van der Vegt, M.** (2019a) Flow division dynamics in the Mekong Delta: Application of a 1D-2D coupled model. *Water*, **11**, 837.

Eslami, S., **Hoekstra, P.**, **Nguyen Trung, N.**, **Ahmed Kantoush, S.**, **Van Binh, D.**, **Duc Dung, D.**, **Tran Quang, T.** and **van der Vegt, M.** (2019b) Tidal amplification and salt intrusion in the Mekong Delta driven by anthropogenic sediment starvation. *Sci Rep.*, **9**, 18746.

Fagherazzi, S. and **Mariotti, G.** (2012) Mudflat runnels: Evidence and importance of very shallow flows in intertidal morphodynamics. *Geophys. Res. Lett.*, **39**, 1–6.

Fennessy, M.J., **Dyer, K.R.**, and **Huntley, D.A.** (1994). Size and settling velocity distributions of flocs in the Tamar estuary during a tidal cycle. *Netherl. J. Aquat. Ecol.*, **28**, 275–282.

Fernandes, M.E.B., **Oliveira, F.P.** and **Eyzaguirre, I.A.L.** (2018) Mangroves on the Brazilian Amazon Coast: Uses and Rehabilitation. In: *Coastal Research Library* (Ed. C. Makowski and C. Finkl), *Springer, Cham*, 25, 621–635.

Ferreira, T.O., **Otero, X.L.**, **Vidal-Torrado, P.** and **Macías, F.** (2007) Effects of bioturbation by root and crab activity on iron and sulfur biogeochemistry in mangrove substrate. *Geoderma*, **142**, 36–46.

Fortunato, A.B., **Baptista, A.M.** and **Luettich, R.A.** (1997) A three-dimensional model of tidal currents in the mouth of the Tagus estuary. *Cont. Shelf Res.*, **17**, 1689–1714.

Fricke, A.T., **Nittrouer, C.A.**, **Ogston, A.S.**, **Nowacki, D.J.**, **Asp, N.E.** and **Souza Filho, P.W.M.** (2019) Morphology and dynamics of the intertidal floodplain along the Amazon tidal river. *Earth Surf. Process. Landforms*, **44**, 204–218.

Fricke, A.T., **Nittrouer, C.A.**, **Ogston, A.S.**, **Nowacki, D.J.**, **Asp, N.E.**, **Souza Filho, P.W.M.**, **da Silva, M.S.** and **Jalowska, A.M.** (2017a) River tributaries as sediment sinks: Processes operating where the Tapajós and Xingu rivers meet the Amazon tidal river. *Sedimentology*, **64**, 1731–1753.

Fricke, A.T., **Nittrouer, C.A.**, **Ogston, A.S.** and **Vo-Luong, H.P.** (2017b) Asymmetric progradation of a coastal mangrove forest controlled by combined fluvial and marine influence, Cù Lao Dung, Vietnam. *Cont. Shelf Res.*, **147**, 78–90.

Friedrichs, C.T. and **Aubrey, D.G.** (1988) Non-linear tidal distortion in shallow well-mixed estuaries: A synthesis. *Estuar. Coast. Shelf Sci.*, **27**, 521–545.

Friedrichs, C.T., **Aubrey, D.G.** and **Speer, P.E.** (1990) Impacts of relative sea-level rise on evolution of shallow estuaries. *Coast. Estuar. Stud.*, **38**, 105–122.

Friedrichs, C.T., **Wright, L.D.**, **Hepworth, D.A.** and **Kim, S.C.** (2000) Bottom-boundary-layer processes associated with fine sediment accumulation in coastal seas and bays. *Cont. Shelf*

Res., **20**, 807–841.

Frings, R.M. and **Kleinhans, M.G.** (2008) Complex variations in sediment transport at three large river bifurcations during discharge waves in the river Rhine. *Sedimentology*, **55**, 1145–1171.

Furukawa, K., **Wolanski, E.** and **Mueller, H.** (1997) Currents and sediment transport in mangrove forests. *Estuar. Coast. Shelf Sci.*, **44**, 301–310.

Gallo, M.N. and **Vinzon, S.B.** (2005) Generation of overtides and compound tides in Amazon estuary. *Ocean Dyn.*, **55**, 441–448.

Gastaldo, R.A., **Allen, G.P.** and **Huc, A.Y.** (1995) The tidal character of fluvial sediments of the modern Mahakam River delta, Kalimantan, Indonesia. *Spec. Publ. Int. Assoc. Sedimentol.*, **24**, 171–181.

Geyer, R.W., **Beardsley, R.C.**, **Lentz, S.J.**, **Candela, J.**, **Limeburner, R.**, **Johns, W.E.**, **Castro, B.M.** and **Dias Soares, I.** (1996) Physical oceanography of the Amazon shelf. *Cont. Shelf Res.*, **16**, 575–616.

Geyer, W.R. and **MacCready, P.** (2014) The estuarine circulation. *Annu. Rev. Fluid Mech.*, **46**, 175–197.

Gibbs, R.J. (1976) Amazon River sediment transport in the Atlantic Ocean. *Geology*, **4**, 45–48.

Glaser, M. (2003) Interrelations between mangrove ecosystem, local economy and social sustainability in Caeté Estuary, North Brazil. *Wetl. Ecol. Manag.*, **11**, 265–272.

Gomes, D., **Ara, F.**, **Simith, B.** and **Asp, N.E.** (2013a) Mangrove sedimentary characteristics and implications for crab Ucides cordatus (Crustacea, Decapoda, Ucididae) distribution in an estuarine area of the Amazonian region. *Acta Amaz.*, **43**, 481–489.

Gomes, V.J.C., **Freitas, P.T.A.** and **Asp, N.E.** (2013b) Dynamics and seasonality of the middle sector of a macrotidal estuary dynamics. *J. Coast. Res.*, **SI 65**, 1140–1145.

Granek, E.F. and **Ruttenberg, B.I.** (2007) Protective capacity of mangroves during tropical storms: A case study from "Wilma" and "Gamma" in Belize. *Mar. Ecol. Prog. Ser.*, **343**, 101–105.

Gratiot, N., **Bildstein, A.**, **Anh, T.T.**, **Thoss, H.**, **Denis, H.**, **Michallet, H.** and **Apel, H.** (2017) Sediment flocculation in the Mekong River estuary, Vietnam, an important driver of geomorphological changes. *Comptes Rendus Geosci.*, **349**, 260–268.

Hale, R., **Bain, R.**, **Goodbred, S.** and **Best, J.** (2019) Observations and scaling of tidal mass transport across the lower Ganges-Brahmaputra delta plain: Implications for delta management and sustainability. *Earth Surf. Dyn.*, **7**, 231–245.

Haque, A., **Sumaiya, S.** and **Rahman, M.** (2015) Flow distribution and sediment transport mechanism in the estuarine systems of Ganges-Brahmaputra-Meghna Delta. *Int. J. Environ. Sci. Dev.*, **7**, 22–30.

Harris, P.T., **Hughes, M.G.**, **Baker, E.K.**, **Dalrymple, R.W.** and **Keene, J.B.** (2004) Sediment transport in distributary channels and its export to the pro-deltaic environment in a tidally dominated delta: Fly River, Papua New Guinea. *Cont. Shelf Res.*, **24**, 2431–2454.

Hayashi, S.N., **Souza-Filho, P.W.M.**, **Nascimento, W.R.** and **Fernandes, M.E.B.** (2019) The effect of anthropogenic drivers on spatial patterns of mangrove land use on the Amazon coast. *PLoS One*, **14**, 1–20.

Hecht, J.S., **Lacombe, G.**, **Arias, M.E.**, **Dang, T.D.** and **Piman, T.** (2019) Hydropower dams of the Mekong River basin: A review of their hydrological impacts. *J. Hydrol.*, **568**, 285–300.

Hoitink, A.J.F. and **Jay, D.A.** (2016) Tidal river dynamics: Implications for deltas. *Rev. Geophys.*, **54**, 240–272.

Horstman, E.M., **Dohmen-Janssen, C.M.**, **Bouma, T.J.** and **Hulscher, S.J.M.H.** (2015) Tidal-scale flow routing and sedimentation in mangrove forests: Combining field data and numerical modelling. *Geomorphology*, **228**, 244–262.

Ikejima, K., **Tongnunui, P.**, **Medej, T.** and **Taniuchi, T.** (2003) Juvenile and small fishes in a mangrove estuary in Trang province, Thailand: Seasonal and habitat differences. *Estuar. Coast. Shelf Sci.*, **56**, 447–457.

Jay, D.A. and **Flinchem, P.** (1997) Interaction of fluctuating river flow with a barotropic tide: A demonstration of wavelet tidal analysis methods. *J. Geophys. Res.*, **102**, 5705–5720.

Jiyu, C., **Huifang, Z.**, **Yongfa, D.** and **Jieming, S.** (1985) Development of the Changjiang estuary and its submerged delta. *Cont. Shelf Res.*, **4**, 47–56.

Johnson, D.W. (1919) Shore processes and shoreline development. *John Wiley & Sons, Inc.*, New York, 584 pp.

Jones, N.L. and **Monismith, S.G.** (2008) The influence of whitecapping waves on the vertical structure of turbulence in a shallow estuarine embayment. *J. Phys. Oceanogr.*, **38**, 1563–1580.

Kästner, K., **Hoitink, A.J.F.**, **Vermeulen, B.**, **Geertsema, T.J.** and **Ningsih, N.S.** (2017) Distributary channels in the fluvial to tidal transition zone. *J. Geophys. Res. Earth Surf.*, **122**, 696–710.

Kathiresan, K. (2003) How do mangrove forests induce sedimentation? *Rev. Biol. Trop.*, **51**, 355–359.

King, B. and **Wolanski, E.** (1996) Bottom friction reduction in turbid estuaries. In: *Mixing in Estuaries and Coastal Seas* (Ed. C. Pattiaratchi), 325–337.

King, C.A.M. and **Williams, W.W.** (1949) The formation and movement of sand bars by wave action. *Geogr. J.*, **113**, 70–85.

Kondolf, G.M., **Gao, Y.**, **Annandale, G.W.**, **Morris, G.L.**, **Jiang, E.**, **Hotchkiss, R.** and **Carling, P.** (2014) Sustainable sediment management in reservoirs and regulated rivers: Experiences from five continents. The United States Agency for International Development Regional Development Mission for Asia.

Krauss, K.W., **Cahoon, D.R.**, **Allen, J.A.**, **Ewel, K.C.**, **Lynch, J.C.** and **Cormier, N.** (2010) Surface elevation change and susceptibility of different mangrove zones to sea-level rise on Pacific high islands of Micronesia. *Ecosystems*, **13**, 129–143.

Kuehl, S.A., **DeMaster, D.J.** and **Nittrouer, C.A.** (1986) Nature of sediment accumulation on the Amazon continental shelf. *Cont. Shelf Res.*, **6**, 209–225.

Kummu, M., **de Moel, H.**, **Salvucci, G.**, **Viviroli, D.**, **Ward, P.J.** and **Varis, O.** (2016) Over the hills and further away from coast: Global geospatial patterns of human and environment over the 20th–21st centuries. *Environ. Res. Lett.*, **11**, 34010.

Langbein, W.B. (1963) The hydraulic geometry of a shallow estuary. *Hydrol. Sci. J.*, **8**, 84–94.

Lanzoni, S. (2002) Long-term evolution and morphodynamic equilibrium of tidal channels. *J. Geophys. Res.*, **107**, 3001.

Larcombe, P. and **Ridd, P.V.** (1996) Dry season hydrodynamics and sediment transport in a mangrove creek. *Mix. Estuaries Coast. Seas*, **50**, 388–404.

Larsen, L.G. and **Harvey, J.W.** (2010) How vegetation and sediment transport feedbacks drive landscape change in the Everglades and wetlands worldwide. *Am. Nat.*, **176**, E66–E79.

Larsen, L.G., **Harvey, J.W.** and **Crimaldi, J.P.** (2009) Morphologic and transport properties of natural organic floc. *Water Resour. Res.*, **45**, 1–13.

Leopold, L.B. and **Maddock, T.** (1953) The hydraulic geometry of stream channels and some

physiographic implications. *USGS Prof. Pap.*, **252**.

Li, W., **Bhattacharya, J.P.** and **Wang, Y.** (2011) Delta asymmetry: Concepts, characteristics, and depositional models. *Pet. Sci.*, **8**, 278–289.

Li, X., **Liu, J.P.**, **Saito, Y.** and **Nguyen, V.L.** (2017) Recent evolution of the Mekong Delta and the impacts of dams. *Earth-Science Rev.* **175**, 1–17.

Lincoln, J.M. and **Fitzgerald, D.M.** (1988) Tidal distortions and flood dominance at five small tidal inlets in southern Maine. *Mar. Geol.*, **82**, 133–148.

Liu, J.P., **DeMaster, D.J.**, **Nittrouer, C.A.**, **Eidam, E.F.** and **Nguyen, T.T.** (2017) A seismic study of the Mekong subaqueous delta: Proximal versus distal sediment accumulation. *Cont. Shelf Res.*, **147**, 197–212.

Liu, S., **Li, X.**, **Chen, D.**, **Duan, Y.**, **Ji, H.**, **Zhang, L.**, **Chai, Q.** and **Hu, X.** (2020) Understanding land use/land cover dynamics and impacts of human activities in the Mekong Delta over the last 40 years. *Glob. Ecol. Conserv.*, **22**, e00991.

Liu, Z., **Zhao, Y.**, **Colin, C.**, **Stattegger, K.**, **Wiesner, M.G.**, **Huh, C.A.**, **Zhang, Y.**, **Li, X.**, **Sompongchaiyakul, P.**, **You, C.F.**, **Huang, C.Y.**, **Liu, J.T.**, **Siringan, F.P.**, **Le, K.P.**, **Sathiamurthy, E.**, **Hantoro, W.S.**, **Liu, J.**, **Tuo, S.**, **Zhao, S.**, **Zhou, S.**, **He, Z.**, **Wang, Y.**, **Bunsomboonsakul, S.** and **Li, Y.** (2016) Source-to-sink transport processes of fluvial sediments in the South China Sea. *Earth-Science Rev.*, **153**, 238–273.

Lyard, F., **Lefevre, F.**, **Letellier, T.** and **Francis, O.** (2006) Modelling the global ocean tides: Modern insights from FES2004. *Ocean Dyn.*, **56**, 394–415.

Manning, A.J. (2002) The observed effects of turbulence on estuarine flocculation. *J. Coast. Res.*, **SI41**, 90–104.

Mazda, Y., **Kanazawa, N.** and **Wolanski, E.** (1995) Tidal asymmetry in mangrove creeks. *Hydrobiologia*, **295**, 51–58.

Mazda, Y., **Kobashi, D.** and **Okada, S.** (2005) Tidal-scale hydrodynamics within mangrove swamps. *Wetl. Ecol. Manag.*, **13**, 647–655.

Mazda, Y., **Magi, M.**, **Kogo, M.** and **Hong, P.N.** (1997) Mangroves as a coastal protection from waves in the Tong King Delta, Vietnam. *Mangroves Salt Marshes*, **1**, 127–135.

McKee, K.L., **Cahoon, D.R.** and **Feller, I.C.** (2007) Caribbean mangroves adjust to rising sea level through biotic controls on change in soil elevation. *Glob. Ecol. Biogeogr.*, **16**, 545–556.

McLachlan, R.L., **Ogston, A.S.** and **Allison, M.A.** (2017) Implications of tidally-varying bed stress and intermittent estuarine stratification on fine-sediment dynamics through the Mekong's tidal river to estuarine reach. *Cont. Shelf Res.*, **147**, 27–37.

McLachlan, R.L., **Ogston, A.S.**, **Asp, N.E.**, **Fricke, A.T.**, **Nittrouer, C.A.** and **Gomes, V.J.C.** (2020) Impacts of tidal-channel connectivity on transport asymmetry and sediment exchange with mangrove forests. *Estuar. Coast. Shelf Sci.*, **233**, 106524.

Meade, R.H. (1972) Transport and deposition of sediment in estuaries. In: *Environmental Framework of Coastal Plain Estuaries* (Ed. B.W. Nelson),

Meade, R.H. (1969) Landward transport of bottom sediments in estuaries of the Atlantic coastal plain. *J. Sediment. Petrol.*, **39**, 222–234.

Milliman, J.D. and **Farnsworth, K.L.** (2011) River discharge to the coastal ocean - a global synthesis. *Cambridge University Press*, Cambridge.

Milliman, J.D. and **Meade, R.H.** (1983) World-wide delivery of river sediment to the oceans. *J. Geol.*, **91**, 1–21.

Mousavi, M.E., **Irish, J.L.**, **Frey, A.E.**, **Olivera, F.** and **Edge, B.L.** (2011) Global warming and

hurricanes: The potential impact of hurricane intensification and sea level rise on coastal flooding. *Clim. Change*, **104**, 575–597.

Myrick, R.M. and **Leopold, L.B.** (1963) Hydraulic geometry of a small tidal estuary. *USGS Prof. Pap.*, **422-B**.

Nerem, R.S., **Beckley, B.D.**, **Fasullo, J.T.**, **Hamlington, B.D.**, **Masters, D.** and **Mitchum, G.T.** (2018) Climate-change–driven accelerated sea-level rise detected in the altimeter era. *PNAS Earth, Atmos. Planet. Sci.*, **115**, 2022–2025.

Nerem, R.S., **Chambers, D.P.**, **Choe, C.** and **Mitchum, G.T.** (2010) Estimating mean sea level change from the TOPEX and Jason altimeter missions. *Mar. Geod.*, **33**, 435–446.

Nguyen, A.D., **Savenije, H.H.G.**, **Pham, D.N.** and **Tang, D.T.** (2008) Using salt intrusion measurements to determine the freshwater discharge distribution over the branches of a multi-channel estuary: The Mekong Delta case. *Estuar. Coast. Shelf Sci.*, **77**, 433–445.

Nicholls, R.J., **Hoozemans, F.M.J.** and **Marchand, M.** (1999) Increasing flood risk and wetland losses due to global sea-level rise: Regional and global analyses. *Glob. Environ. Chang.*, **9**, S69–S87.

Nidzieko, N.J. (2010) Tidal asymmetry in estuaries with mixed semidiurnal/diurnal tides. *J. Geophys. Res. Ocean.*, **115**, 1–13.

Nidzieko, N.J. and **Ralston, D.K.** (2012) Tidal asymmetry and velocity skew over tidal flats and shallow channels within a macrotidal river delta. *J. Geophys. Res. Ocean.*, **117**, 1–17.

Nienhuis, J.H., **Ashton, A.D.**, **Edmonds, D.A.**, **Hoitink, A.J.F.**, **Kettner, A.J.**, **Rowland, J.C.** and **Törnqvist, T.E.** (2020) Global-scale human impact on delta morphology has led to net land area gain. *Nature*, **577**, 514–518.

Nienhuis, J.H., **Hoitink, A.J.F.T.** and **Törnqvist, T.E.** (2018) Future change to tide-influenced deltas. *Geophys. Res. Lett.*, **45**, 3499–3507.

Nittrouer, C. A. and **DeMaster, D.J.** (1996) The Amazon shelf setting: Tropical, energetic, and influenced by a large river. *Cont. Shelf Res.*, **16**, 553–573.

Nittrouer, C.A., **Sternberg, R.W.**, **Carpenter, R.** and **Bennett, J.T.** (1979) The use of Pb-210 geochronology as a sedimentological tool: Application to the Washington continental shelf. *Mar. Geol.*, **31**, 297–316.

Norris, B.K., **Mullarney, J.C.**, **Bryan, K.R.** and **Henderson, S.M.** (2017) The effect of pneumatophore density on turbulence: A field study in a Sonneratia-dominated mangrove forest, Vietnam. *Cont. Shelf Res.*, **147**, 114–127.

Nowacki, D.J. and **Ogston, A.S.** (2013) Water and sediment transport of channel-flat systems in a mesotidal mudflat: Willapa Bay, Washington. *Cont. Shelf Res.*, **60**, S111–S124.

Nowacki, D.J., **Ogston, A.S.**, **Nittrouer, C.A.**, **Fricke, A.T.** and **Van, P.D.T.** (2015) Sediment dynamics in the lower Mekong River: Transition from tidal river to estuary. *J. Geophys. Res. Ocean.*, **120**, 6363–6383.

Oertel, G.F. and **Overman, K.** (2004) Sequence morphodynamics at an emergent barrier island, middle Atlantic coast of North America. *Geomorphology*, **58**, 67–83.

Otvos, E.G. (1981) Barrier island formation through nearshore aggradation - Stratigraphic and field evidence. *Mar. Geol.*, **43**, 195–243.

Parkinson, R.W., **DeLaune, R.D.** and **White, J.R.** (1994) Holocene sea-level rise and the fate of mangrove forests within the wider Caribbean region. *J. Coast. Res.*, **10**, 1077–1086.

Pereira, L.C.C., **Nascimento Trindade, W.**, **da Silva, I.R.**, **Vila-Concejo, A.** and **Short, A.D.** (2016) Maranhão Beach Systems, Including the Human Impact on São Luís Beaches. In: *Brazilian Beach Systems* (Ed. A.D. Short and A.H. da F. Klein), *Springer International*

Publishing, Cham, 125–152.

Pestrong, R. (1965) The development of drainage patterns on tidal marshes. *Stanford University Press*, Stanford, CA, 87 pp.

Postma, H. (1961) Transport and accumulation of suspended matter in the Dutch Wadden Sea. *Netherlands J. Res.*, **1**, 148–190.

Postma, H. (1967) Sediment transport and sedimentation in the estuarine environment. *Estuaries*, 158–179.

Pritchard, D. (2005) Suspended sediment transport along an idealised tidal embayment: Settling lag, residual transport and the interpretation of tidal signals. *Ocean Dyn.*, **55**, 124–136.

Pritchard, M. and **Green, M.** (2017) Trapping and episodic flushing of suspended sediment from a tidal river. *Cont. Shelf Res.*, **143**, 286–294.

Qiu, C. and **Zhu, J.R.** (2013) Influence of seasonal runoff regulation by the Three Gorges Reservoir on saltwater intrusion in the Changjiang River Estuary. *Cont. Shelf Res.*, **71**, 16–26.

Ralston, D.K. and **Geyer, W.R.** (2017) Sediment transport time scales and trapping efficiency in a tidal river. *J. Geophys. Res. Earth Surf.*, **122**, 2042–2063.

Redmond, G., **Hodges, K.I.**, **Mcsweeney, C.**, **Jones, R.** and **Hein, D.** (2015) Projected changes in tropical cyclones over Vietnam and the South China Sea using a 25 km regional climate model perturbed physics ensemble. *Clim. Dyn.*, **45**, 1983–2000.

Rehage, J.S. and **Loftus, W.F.** (2007) Seasonal fish community variation in headwater mangrove creeks in the southwestern everglades: An examination of their role as dry-down refuges. *Bull. Mar. Sci.*, **80**, 625–645.

Reineck, H.E. and **Wunderlich, F.** (1968) Classification and origin of flaser and lenticular bedding. *Sedimentology*, **11**, 99–104.

Rice, K.C., **Hong, B.** and **Shen, J.** (2012) Assessment of salinity intrusion in the James and Chickahominy Rivers as a result of simulated sea-level rise in Chesapeake Bay, East Coast, USA. *J. Environ. Manage.*, **111**, 61–69.

Richey, J.E., **Meade, R.H.**, **Salati, E.**, **Devol, A.H.**, **Nordin, C.F.** and **Santos, U. Dos** (1986) Water discharge and suspended sediment concentrations in the Amazon River: 1982–1984. *Water Resour. Res.*, **22**, 756–764.

Ripley, B.D. (1976) The second-order analysis of stationary point processes. *J. Appl. Probab.*, **13**, 255–266.

Ripley, B.D. (1977) Modelling spatial patterns. *J. R. Stat. Soc. Ser. B*, **39**, 172–212.

Robertson, A.I. and **Duke, N.C.** (1987) Mangroves as nursery sites: Comparisons of the abundance and species composition of fish and crustaceans in mangroves and other nearshore habitats in tropical Australia. *Mar. Biol.*, **96**, 193–205.

Rogers, K.G., **Goodbred, S.** and **Migration, H.** (2014) The Sundarbans and Bengal Delta: The world's largest tidal mangrove and delta system. In: *Landscapes and Landforms of India* (Ed. V.S. Kale), *Springer*, New York,

Rossetti, D.F. (2003) Delineating shallow Neogene deformation structures in northeastern Pará State using ground penetrating radar. *An. Acad. Bras. Cienc.*, **75**, 235–248.

Roy, P.S., **Thom, B.G.** and **Wright, L.D.** (1980) Holocene sequences an an embayed high-energy coast: An evolutionary model. *Sediment. Geol.*, **26**, 1–19.

Salahuddin, H. (2011) Dynamics of saline water incursion in the Mahakam Delta, East Kalimantan. In: *Proceedings JCM Makassar*.

Sassi, M.G., **Hoitink, A.J.F.**, **Vermeulen, B.** and **Hidayat, H.** (2013) Sediment discharge

division at two tidally influenced river bifurcations. *Water Resour. Res.*, **49**, 2119–2134.

Schettini, C.A.F., **Asp, N.E.**, **Ogston, A.S.**, **Gomes, V.J.C.**, **McLachlan, R.L.**, **Fernandes, M.E.B.**, **Nittrouer, C.**, **Truccolo, E.C.** and **Gardunho, D.C.L.** (2019) Circulation and fine-sediment dynamics in the Amazon macrotidal mangrove coast. *Earth Surf. Process. Landforms*. doi: 10.1002/esp.4756

Schubel, J.R. (1968) Turbidity maximum of the northern Chesapeake Bay. *Science*, **161**, 1013–1015.

Schuerch, M., **Spencer, T.**, **Temmerman, S.**, **Kirwan, M.L.**, **Wolff, C.**, **Lincke, D.**, **McOwen, C.J.**, **Pickering, M.D.**, **Reef, R.**, **Vafeidis, A.T.**, **Hinkel, J.**, **Nicholls, R.J.**, **Brown, S.**, **Loo, Y.Y.**, **Billa, L.** and **Singh, A.** (2018) Future response of global coastal wetlands to sea-level rise. *Nature*, **561**, 231–234.

Schwarz, C., **Cox, T.**, **van Engeland, T.**, **van Oevelen, D.**, **van Belzen, J.**, **van de Koppel, J.**, **Soetaert, K.**, **Bouma, T.J.**, **Meire, P.** and **Temmerman, S.** (2017) Field estimates of floc dynamics and settling velocities in a tidal creek with significant along-channel gradients in velocity and SPM. *Estuar. Coast. Shelf Sci.*, **197**, 221–235.

Scully, M.E. and **Friedrichs, C.T.** (2007) Sediment pumping by tidal asymmetry in a partially mixed estuary. *J. Geophys. Res. Ocean.*, **112**, 1–12.

Sheridan, P. and **Hays, C.** (2003) Are mangroves nursery habitat for transient fishes and decapods? *Wetlands*, **23**, 449–458.

Sloss, C.R., **Jones, B.G.**, **Brooke, B.P.**, **Heijnis, H.** and **Murray-Wallace, C. V.** (2011) Contrasting sedimentation rates in Lake Illawarra and St Georges Basin, two large barrier estuaries on the southeast coast of Australia. *J. Paleolimnol.*, **46**, 561–577.

Sloss, C.R., **Jones, B.G.**, **Murray-Wallace, C. V.** and **McClennen, C.E.** (2005) Holocene sea level fluctuations and the sedimentary evolution of a barrier estuary: Lake Illawarra, New South Wales, Australia. *J. Coast. Res.*, **21**, 943–959.

Sloss, C.R., **Murray-Wallace, C. V.** and **Jones, B.G.** (2007) Holocene sea-level change on the southeast coast of Australia: A review. *The Holocene*, **17**, 999–1014.

Sobel, A.H., **Camargo, S.J.**, **Hall, T.M.**, **Lee, C.**, **Tippett, M.K.** and **Wing, A.A.** (2016) Human influence on tropical cyclone intensity. *Science.*, **353**, 242–246.

Soulsby, R.L., **Manning, A.J.**, **Spearman, J.** and **Whitehouse, R.J.S.** (2013) Settling velocity and mass settling flux of flocculated estuarine sediments. *Mar. Geol.*, **339**, 1–12.

Souza-Filho, P.W.M., **Cohen, M.C.L.**, **Lara, R.J.**, **Lessa, G.C.**, **Koch, B.** and **Behling, H.** (2006) Holocene coastal evolution and facies model of the Bragança macrotidal flat on the Amazon mangrove coast, northern Brazil. *J. Coast. Res.*, **SI 39**, 306–310.

Souza-Filho, P.W.M., **Lessa, G.C.**, **Cohen, M.C.L.**, **Costa, F.R.** and **Lara, R.J.** (2009) The subsiding macrotidal barrier estuarine system of the Eastern Amazon Coast, Northern Brazil. In: *Geology and Geomorphology of Holocene Coastal Barriers of Brazil . Lecture Notes in Earth Sciences.*, *Springer, Berlin, Heidelberg*, 347–375.

Souza-Filho, P.W.M., **Morais Tozzi, H.A.** and **El-Robrini, M.** (2003) Geomorphology, land-use and environmental hazards in Ajuruteua macrotidal sandy beach, northern Brazil. *J. Coast. Res.*, **SI 35**, 580–589.

Spalding, M.D., **Blasco, E.** and **Field, C.D.** (1997) World Mangrove Atlas. *The International Society for Mangrove Ecosystems*, Okiwana, Japan, 178 pp.

Speer, P.E., **Aubrey, D.G.** and **Friedrichs, C.T.** (1991) Nonlinear hydrodynamics of shallow tidal inlet/bay systems. In: *Tidal Hydrodynamics* (Ed. B.B. Parker), *John Wiley & Sons, Inc.*, 321–339.

Stanley, D.J. and **Hait, A.K.** (2000) Holocene depositional patterns, neotectonics and Sundarban mangroves in the western Ganges-Brahmaputra delta. *J. Coast. Res.*, **16**, 26–39.

Stephens, J.D., **Allison, M.A.**, **Di Leonardo, D.R.**, **Weathers, H.D.**, **Ogston, A.S.**, **McLachlan, R.L.**, **Xing, F.** and **Meselhe, E.A.** (2017) Sand dynamic in the Mekong River channel and export to the coastal ocean. *Cont. Shelf Res.*, **147**, 38–50.

Sternberg, R.W., **Ogston, A.** and **Johnson, R.** (1996) A video system for in situ measurement of size and settling velocity of suspended particulates. *J. Sea Res.*, **36**, 127–130.

Swales, A., **Bentley, S.J.** and **Lovelock, C.E.** (2015) Mangrove-forest evolution in a sediment-rich estuarine system: Opportunists or agents of geomorphic change? *Earth Surf. Process. Landforms*, **40**, 1672–1687.

Syvitski, J.P.M. and **Kettner, A.** (2011) Sediment flux and the Anthropocene. *Philos. Trans. R. Soc. A Math. Phys. Eng. Sci.*, **369**, 957–975.

Syvitski, J.P.M., **Kettner, A.J.**, **Overeem, I.**, **Hutton, E.W.H.**, **Hannon, M.T.**, **Brakenridge, G.R.**, **Day, J.**, **Vörösmarty, C.**, **Saito, Y.**, **Giosan, L.** and **Nicholls, R.J.** (2009) Sinking deltas due to human activities. *Nat. Geosci.*, **2**, 681–686.

Ta, T.K.O., **Nguyen, V.L.**, **Tateishi, M.**, **Kobayashi, I.**, **Tanabe, S.** and **Saito, Y.** (2002) Holocene delta evolution and sediment discharge of the Mekong River, southern Vietnam. *Quaternary Sci. Rev.*, **21**, 1807–1819.

Tamura, T., **Saito, Y.**, **Lap Nguyen, V.**, **Oanh Ta, T.K.**, **Bateman, M.D.**, **Matsumoto, D.** and **Yamashita, S.** (2012) Origin and evolution of interdistributary delta plains; insights from Mekong River delta. *Geology*, **40**, 303–306.

Thampanya, U., **Vermaat, J.E.**, **Sinsakul, S.** and **Panapitukkul, N.** (2006) Coastal erosion and mangrove progradation of Southern Thailand. *Estuar. Coast. Shelf Sci.*, **68**, 75–85.

Thomson, R.E. and **Emery, W.J.** (2014) Data analysis methods in physical oceanography, 3rd edn. *Elsevier B.V.*, 728 pp.

Thorbjarnarson, K.W., **Nittrouer, C.A.**, **DeMaster, D.J.** and **McKinney, R.B.** (1985) Sediment accumulation in a back-barrier lagoon, Great Sound, New Jersey. *J. Sediment. Petrol.*, **55**, 856–863.

Thorne, C., **Annandale, G.**, **Jensen, J.** and **Jensen, E.** (2011) Review of Sediment Transport, Morphology, and Nutrient Balance. 82 pp.

Traynum, S. and **Styles, R.** (2008) Exchange flow between two estuaries connected by a shallow tidal channel. *J. Coast. Res.*, **24**, 1260–1268.

Trowbridge, J.H. and **Kineke, G.C.** (1994) Structure and dynamics of fluid muds on the Amazon continental shelf. *J. Geophys. Res.*, **99**, 865–874.

Tu, L.X., **Thanh, V.Q.**, **Reyns, J.**, **Van, S.P.**, **Anh, D.T.**, **Dang, T.D.** and **Roelvink, D.** (2019) Sediment transport and morphodynamical modeling on the estuaries and coastal zone of the Vietnamese Mekong Delta. *Cont. Shelf Res.*, **186**, 64–76.

Uncles, R.J., **Bale, A.J.**, **Brinsley, M.D.**, **Frickers, P.E.**, **Harris, C.**, **Lewis, R.E.**, **Pope, N.D.**, **Staff, F.J.**, **Stephens, J.A.**, **Turley, C.M.** and **Widdows, J.** (2003) Intertidal mudflat properties, currents and sediment erosion in the partially mixed Tamar Estuary, UK. *Ocean Dyn.*, **53**, 239–251.

Vafeidis, A.T., **Nicholls, R.J.**, **Mcfadden, L.**, **Tol, R.S.J.**, **Hinkel, J.**, **Spencer, T.**, **Grashoff, P.S.**, **Boot, G.**, **Klein, R.J.T.**, **Vafeidis, A.T.**, **Nicholls, R.J.**, **Mcfadden, L.**, **Toln, R.S.J.**, **Hinkelw, J.**, **Spencer, T.**, **Grashoff, P.S.**, **Boot, G.** and **Klein, R.J.T.** (2008) A new global coastal database for impact and vulnerability analysis to sea-level rise. *J. Coast.*, **24**, 917–924.

van Maanen, B., **Coco, G.** and **Bryan, K.R.** (2015) On the ecogeomorphological feedbacks that control tidal channel network evolution in a sandy mangrove setting. *Proc. R. Soc. A Math. Phys. Eng. Sci.*, **471**, 20150115.

Van Santen, P., **Augustinus, P.G.E.F.**, **Janssen-Stelder, B.M.**, **Quartel, S.** and **Tri, N.H.** (2007) Sedimentation in an estuarine mangrove system. *J. Asian Earth Sci.*, **29**, 566–575.

Wagner, W. and **Mohrig, D.** (2019) Flow and sediment flux asymmetry in a branching channel delta. *Water Resour. Res.*, **55**, 9563–9577.

Walling, D.E. (2006) Human impact on land-ocean sediment transfer by the world's rivers. *Geomorphology*, **79**, 192–216.

Walsh, J.P. and **Nittrouer, C.A.** (2004) Mangrove-bank sedimentation in a mesotidal environment with large sediment supply, Gulf of Papua. *Mar. Geol.*, **208**, 225–248.

Walsh, K.J.E., **Mcbride, J.L.**, **Klotzbach, P.J.**, **Balachandran, S.**, **Camargo, S.J.**, **Holland, G.**, **Knutson, T.R.**, **Kossin, J.P.**, **Lee, T.C.**, **Sobel, A.** and **Sugi, M.** (2016) Tropical cyclones and climate change. *Wiley Interdiscip. Rev. Clim. Chang.*, **7**, 65–89.

Warner, J.C., **Schoellhamer, D.** and **Schladow, G.** (2003) Tidal truncation and barotropic convergence in a channel network tidally driven from opposing entrances. *Estuar. Coast. Shelf Sci.*, **56**, 629–639.

Warrick, J.A., **Bountry, J.A.**, **East, A.E.**, **Magirl, C.S.**, **Randle, T.J.**, **Gelfenbaum, G.**, **Ritchie, A.C.**, **Pess, G.R.**, **Leung, V.** and **Duda, J.J.** (2015) Large-scale dam removal on the Elwha River, Washington, USA: Source-to-sink sediment budget and synthesis. *Geomorphology*, **246**, 729–750.

Wassmann, R., **Phong, N.D.**, **Tho, T.Q.**, **Hoanh, C.T.**, **Khoi, N.H.**, **Hien, N.X.**, **Vo, T.B.T.** and **Tuong, T.P.** (2019) High-resolution mapping of flood and salinity risks for rice production in the Vietnamese Mekong Delta. *F. Crop. Res.*, **236**, 111–120.

Wattayakorn, G., **Wolanski, E.** and **Kjerfve, B.** (1990) Mixing, trapping and outwelling in the Klong Ngao mangrove swamp, Thailand. *Estuar. Coast. Shelf Sci.*, **31**, 667–688.

West, J.R. and **Oduyemi, K.O.K.** (1989) Turbulence measurements of suspended solids concentration in estuaries. *J. Hydraul. Eng.*, **115**, 457–474.

Winterwerp, J.C. (2002) On the flocculation and settling velocity of estuarine mud. *Cont. Shelf Res.*, **22**, 1339–1360.

Winterwerp, J.C. (2001) Stratification effects by cohesive and noncohesive sediment. *J. Geophys. Res. Ocean.*, **106**, 22559–22574.

Wolanski, E. (1995) Transport of sediment in mangrove swamps. *Hydrobiologia*, **295**, 31–42.

Wolanski, E., **Huan, N.N.**, **Dao, L.T.**, **Nhan, N.H.** and **Thuy, N.N.** (1996) Fine-sediment dynamics in the Mekong River estuary, Vietnam. *Estuar. Coast. Shelf Sci.*, **43**, 565–582.

Wolanski, E., **Jones, M.** and **Bunt, J.S.** (1980) Hydrodynamics of a tidal creek-mangrove swamp system. *Aust. J . Mar. Freshw. Res*, **31**, 431–50.

Wolanski, E., **Mazda, Y.** and **Ridd, P.** (1992) Mangrove Hydrodynamics. In: *Tropical Mangrove Ecosystems*, 41, 43–62.

Woodroffe, C.D. (1985) Studies of a mangrove basin, Tuff Crater, New Zealand: II. Comparison of volumetric and velocity-area methods of estimating tidal flux. *Estuar. Coast. Shelf Sci.*, **20**, 431–445.

Woodroffe, C.D., **Rogers, K.**, **McKee, K.L.**, **Lovelock, C.E.**, **Mendelssohn, I.A.** and **Saintilan, N.** (2016) Mangrove sedimentation and response to relative sea-level rise. *Ann. Rev. Mar. Sci.*, **8**, 243–266.

Wright, L.D. and **Coleman, J.M.** (1974) Mississippi River mouth processes: Effluent dynamics

and morphologic development. *J. Geol.*, **82**, 751–778.

Wright, L.D., **Coleman, J.M.** and **Thom, B.G.** (1973) Processes of channel development in a high-tide-range environment: Cambridge Gulf-Ord River Delta, Western Australia. *J. Geol.*, **81**, 15–41.

Xing, F., **Meselhe, E.A.**, **Allison, M.A.** and **Weathers, H.D.** (2017) Analysis and numerical modeling of the flow and sand dynamics in the lower Song Hau channel, Mekong Delta. *Cont. Shelf Res.*, **147**, 62–77.

Xu, F., **Coco, G.**, **Zhou, Z.**, **Tao, J.** and **Zhang, C.** (2017) A numerical study of equilibrium states in tidal network morphodynamics. *Ocean Dyn.*, **67**, 1593–1607.

Yang, Y.P., **Zhang, M.J.**, **Li, Y.T.** and **Zhang, W.** (2015) The variations of suspended sediment concentration in Yangtze River Estuary. *J. Hydrodyn.*, **27**, 845–856.

Zeff, M.L. (1999) Salt marsh tidal channel morphometry: Applications for wetland creation and restoration. *Restor. Ecol.*, **7**, 205–211.

Zeff, M.L. (1988) Sedimentation in a salt marsh-tidal channel system, southern New Jersey. *Mar. Geol.*, **82**, 33–48.

Zhang, E., **Savenije, H.H.G.**, **Wu, H.**, **Kong, Y.** and **Zhu, J.** (2011) Analytical solution for salt intrusion in the Yangtze Estuary, China. *Estuar. Coast. Shelf Sci.*, **91**, 492–501.

Zimmermann-Timm, H. (2002) Characteristics, dynamics and importance of aggregates in rivers - an invited review. *Int. Rev. Hydrobiol.*, **87**, 197–240.

VITA

Robin McLachlan received her Bachelor of Science degree in Geology from the College of Charleston in South Carolina, a coastal university that facilitated her interests in human-ocean interactions. In 2014, Robin joined the University of Washington's School of Oceanography to continue her research in coastal sediment dynamics. While a graduate student, she also researched best teaching strategies with a focus on communication education. After receiving her Doctor of Philosophy degree, Robin will start as an Assistant Professor in Geology at the College of Coastal Georgia.